

Retrospective Study on Mandible Morphology Towards Improving Implant Design

by

Ryan Gillingham



*Thesis presented in partial fulfilment of the requirements for
the degree of Master of Engineering (Mechatronic) in the
Faculty of Engineering at Stellenbosch University*

Supervisor: Dr. J Van der Merwe

Co-supervisor: Dr. T Mutsvangwa

April 2019

Declaration

By submitting this thesis electronically, I declare that the entirety of the work contained therein is my own, original work, that I am the sole author thereof (save to the extent explicitly otherwise stated), that reproduction and publication thereof by Stellenbosch University will not infringe any third party rights and that I have not previously in its entirety or in part submitted it for obtaining any qualification.

Date: April 2019

Copyright © 2019 Stellenbosch University
All rights reserved.



UNIVERSITEIT • STELLENBOSCH • UNIVERSITY
jou kennisvennoot • your knowledge partner

Plagiaatverklaring / Plagiarism Declaration

- 1 Plagiaat is die oorneem en gebruik van die idees, materiaal en ander intellektuele eiendom van ander persone asof dit jou eie werk is.
Plagiarism is the use of ideas, material and other intellectual property of another's work and to present it as my own.

- 2 Ek erken dat die pleeg van plagiaat 'n strafbare oortreding is aangesien dit 'n vorm van diefstal is.
I agree that plagiarism is a punishable offence because it constitutes theft.

- 3 Ek verstaan ook dat direkte vertalings plagiaat is.
I also understand that direct translations are plagiarism.

- 4 Dienooreenkomstig is alle aanhalings en bydraes vanuit enige bron (ingesluit die internet) volledig verwys (erken). Ek erken dat die woordelike aanhaal van teks sonder aanhalingstekens (selfs al word die bron volledig erken) plagiaat is.
Accordingly all quotations and contributions from any source whatsoever (including the internet) have been cited fully. I understand that the reproduction of text without quotation marks (even when the source is cited) is plagiarism.

- 5 Ek verklaar dat die werk in hierdie skryfstuk vervat, behalwe waar anders aangedui, my eie oorspronklike werk is en dat ek dit nie vantevore in die geheel of gedeeltelik ingehandig het vir bepunting in hierdie module/werkstuk of 'n ander module/werkstuk nie.
I declare that the work contained in this assignment, except where otherwise stated, is my original work and that I have not previously (in its entirety or in part) submitted it for grading in this module/assignment or another module/assignment.

17626676	Ryan Lloyd Gillingham
Studentenommer / Student number	Handtekening / Signature
RL Gillingham	2019/02/18
Voorletters en van / Initials and surname	Datum / Date

Abstract

Retrospective Study on Mandible Morphology Towards Improving Implant Design

R. Gillingham

*Department of Mechanical and Mechatronic Engineering,
University of Stellenbosch,
Private Bag X1, Matieland 7602, South Africa.*

Thesis: MEng (Mech)

April 2019

Pre-surgery planning is crucial to the success of orthognathic surgery. With the advancement in 3D imaging modalities, modern methods in predicting a pathological mandible's ideal geometry have improved. As a result, the design of patient-specific implants has become more commonplace. Before this, standard sized implants were inevitably used. Despite these enhanced virtual reconstruction techniques, limitations in these methods still exist. The most effective approach during virtual reconstruction is to replace the pathological area with the unaffected region on the opposite half of the mandible. This mirroring method becomes futile in scenarios where the disturbance overlaps the mandibular midline. Therefore, the aim of this study was to develop a virtual mandibular reconstruction technique for the purpose of aiding surgeons during implant design, whilst accounting for this limitation. It was proposed that this could be achieved by performing a retrospective investigation on the population's mandibular structure and developing prediction models based on statistical methods.

Two prediction models were formulated: a sparse prediction model (SPM) and a statistical shape model (SSM). The SPM offers a prediction of important unknown mandibular measurements when receiving the values of known measurements as an input, whilst the SSM provides an estimate for the full mandibular geometry after receiving mandibular coordinates as an input. The effectiveness of these techniques was tested by predicting missing anatomical features on subjects not part of the dataset used to create the models. The

tests took place for two scenarios: the first being for when the plane of symmetry is available and the second for when it's not. For the first scenario of testing, the mirroring method was also implemented, where the resulting accuracy served as the baseline.

For both testing scenarios, the SSM clearly outperformed the SPM. Thus, there is no clear benefit in using the SPM over the SSM for virtual reconstruction scenarios. For the first scenario of testing, the SSM compared similarly to the mirroring method, where no significant difference was found between their respective accuracies ($p < 0.05$). The difference between these two methods lies in their restriction of use. Whilst the mirroring method is constrained to situations such as the first scenario, the SSM has no such restriction. For the second scenario, the SSM produced estimations with accuracies similar to the first scenario, thus producing consistent accuracies in geometry prediction regardless of the area being reconstructed. It was therefore concluded that a SSM of the mandible presents itself as a modular virtual reconstruction technique that successfully accounts for the limitations found in current methods.

Uittreksel

Retrospective Study on Mandible Morphology Towards Improving Implant Design

R. Gillingham

*Departement Meganiese en Megatroniese Ingenieurswese,
Universiteit van Stellenbosch,
Privaatsak X1, Matieland 7602, Suid Afrika.*

Tesis: MIng (Meg)

April 2019

Beplanning voor chirurgie is noodsaaklik vir die sukses van ortognatiese chirurgie. Modern metodes om n patologiese kakebeen se ideale geometrie te skep het verbeter met die bevordering van 3D-beeldmodaliteite. Daarom het die ontwerp van pasiënt-spesifieke inplantings meer algemeen geword. Dit was voorheen onvermydelik om standaard-grootte inplantings te gebruik. Ten spyte van hierdie verbeterde virtuele rekonstruksie tegnieke is daar steeds beperkinge met die metodes. Die mees effektiewe rekonstruksie manier is om die patologiese gebied te vervang met die onaangeraakte streek op die teenoorgestelde helfte van die kakebeen. Nietemin, hierdie spieëlmetode is nutteloos in gevalle waar die kakebeen versteuring die middellyn oorvleuel. Daarom was die doel van hierdie studie om 'n virtuele kakebeen rekonstruksie tegniek te ontwikkel om inplantingsontwerp te ondersteun tydens chirurgie wat hierdie beperkings voorkom. Dit is voorgestel dat dit bereik kan word deur 'n terugwerkende ondersoek op die populasie se kakebeen struktuur en die ontwikkeling van 'n voorspellingsmodelle wat gebaseer is op statistiese metodes.

Twee voorspellingsmodelle is geformuleer: 'n skars voorspellingsmodel (SVPM) en 'n statistiese vormmodel (SVM). Die SVPM bied 'n voorspelling van belangrike onbekende kakebeen metings wanneer die waardes van bekende metings as 'n inset ontvang word. Die SVM lewer 'n voorspelling van die volledige kakebeen geometrie nadat die kakebeen koördinate as inset ontvang is. Die effektiwiteit van altwee tegnieke is getoets deur ontbrekende anatomiese kenmerke te voorspel op persone wat nie deel was van die datastel wat gebruik

is om die modelle te skep nie. Die toetse het plaasgevind vir twee scenario's: die eerste is vir wanneer die simmetrievlak beskikbaar is en die tweede vir wanneer dit nie is nie. Vir die eerste scenario van toetse is die spieëlmetode ook geïmplementeer en die resultate dien as die akkuraatheid basis vir die res van die toetse.

Vir beide toets scenario's het die SVM beter presteer as die SVPM. Daarom is daar geen duidelike voordeel in die gebruik van die SVPM oor die SVM vir virtuele rekonstruksiescenario's nie. Vir die eerste scenario van toetse het die SVM geen beduidende verskil gewys in vergelyking met die spieëlmetode (met 'n akkuraatheid van $p < 0.05$). Die twee metodes is onderskeibaar deur hulle verskillende beperkings van gebruik. Terwyl die spieëlmetode beperk word tot gevalle soos die eerste scenario, het die SVM geen sodanige beperkings nie. Vir die tweede scenario het die SVM skattings gelever met 'n soortgelyke akkuraatheid as die eerste scenario, en het dus konsekwente akkuraatheid in geometriese voorspellings gelever ongeag die gebied wat herbou word. Daar is tot die gevolgtrekking gekom dat 'n SVM van n kakebeen 'n suksesvolle tegniek is vir modulêre virtuele rekonstruksie wat die beperkings van huidige metodes voorkom.

Acknowledgements

Dr. J Van der Merwe. Thank you for providing me with a topic that was challenging, yet fascinating at the same time. I truly believe that I have learned a great deal during the project's duration. Your guidance, insight and advice over the past couple of years have been gratefully appreciated.

My colleagues at BERG. Thank you for your support. I leave the office behind, having formed friendships that I do not take for granted.

Lastly, but certainly not least, my parents. The sacrifices that you both have made in order to provide me with all the opportunities possible, is a debt that I will never be able to repay. I appreciate all that you both do for me.

Contents

Declaration	i
Abstract	iii
Uittreksel	v
Acknowledgements	vii
Contents	viii
List of Figures	xi
List of Tables	xiii
Nomenclature	xiv
1 Introduction	1
1.1 Background	1
1.2 Motivation	2
1.3 Aim and objectives	3
2 Literature Study	5
2.1 The Mandible	5
2.2 Orthognathic surgery	8
2.3 Cephalometry	10
2.3.1 Cephalometric analysis	11
2.3.2 Cephalometric prediction	16
2.4 Virtual surgical reconstruction	18
2.4.1 Use of symmetry for implant design	19
2.4.2 Design without the use of symmetry	20
2.5 Summary	22
3 Cephalometric Analysis	23
3.1 Ethical clearance and data collection	24
3.2 Segmenting of skull surfaces	26

3.3	Recording cephalometric measurements	27
3.4	Statistical analysis	29
3.4.1	Correlation	30
3.4.2	Statistical significance	30
3.4.3	Reliability of data	31
3.5	Results/Findings	31
3.5.1	Gender comparison	32
3.5.2	Correlations	33
3.5.3	Comparison to other geographic areas	36
3.5.4	Reliability	38
3.5.5	Recalculation of required sample size	38
3.6	Discussion	38
3.6.1	Gender comparison	38
3.6.2	Correlations	39
3.6.3	Symmetrical nature	39
3.6.4	Comparison to other geographic regions	39
4	Statistical Shape Model Construction	40
4.1	Segmenting of mandibular surfaces	41
4.2	Shape alignment and developing correspondance	42
4.3	Principal component analysis	48
4.4	Shape estimation	52
4.5	Model validation	54
4.6	SSM validation results	55
4.6.1	Compactness	55
4.6.2	Specificity	57
4.6.3	Generality	58
4.7	Discussion	59
4.7.1	Compactness	59
4.7.2	Specificity	60
4.7.3	Generality	60
5	Virtual Reconstruction	61
5.1	Testing procedure	61
5.1.1	First scenario	62
5.1.2	Second scenario	62
5.2	Results	63
5.2.1	First scenario	63
5.2.2	Second scenario	66
5.3	Discussion	68
5.3.1	First scenario	68
5.3.2	Second scenario	69
5.3.3	Results summary	69

<i>CONTENTS</i>	x
6 Conclusions	70
6.1 Fulfilment of project objectives	70
6.1.1 Cephalometric analysis	71
6.1.2 Statistical shape model	71
6.1.3 Evaluation of techniques	71
6.2 Recommendations	72
6.3 Future work	73
6.4 Conclusion	76
List of References	77
Appendices	85
A Sample Size Calculation	86
B SPM Algorithms	89
B.1 Male Algorithms	89
B.1.1 First scenario	89
B.1.2 Second scenario	91
B.2 Female Algorithms	93
B.2.1 First scenario	93
B.2.2 Second scenario	95
C Individual Subject Results	98
C.1 First scenario	98
C.1.1 Male subjects	99
C.1.2 Female subjects	103
C.2 Second scenario	106
C.2.1 Male subjects	107
C.2.2 Female subjects	110

List of Figures

2.1	Mandible's articulation with the temporal bone	6
2.2	Regions of the mandible	7
2.3	Orthognathic surgery for tumor resection	9
2.4	Common orthognathic deformities	10
2.5	Important cephalometric planes	11
2.6	Diagrammatic representation of a lateral cephalogram	12
2.7	Cranial and maxillary landmarks	13
2.8	Mandibular landmarks	16
2.9	Cephalometric prediction of mandibular prognathism	17
2.10	Mirroring virtual reconstruction technique	20
2.11	Bendable mandibular implant	21
3.1	Cephalometric analysis methodology	23
3.2	Snapshot of patient CT scan from all three planes	26
3.3	Coordinate system	27
4.1	Steps in the SSM construction process	41
4.2	Snapshot of patient CT scan with mandible isolated	42
4.3	Segmentation process	42
4.4	Alignment of shapes	44
4.5	Illustration of matching point pairs	45
4.6	Deformation of reference shape to match target shape	48
4.7	Example of a point distribution model	49
4.8	Basic example of PCA	50
4.9	Model fitting procedure	53
4.10	Compactness	56
4.11	Specificity	57
4.12	Generalization ability	59
5.1	Reconstruction for first scenario	62
5.2	Reconstruction for second scenario	63
6.1	Automated segmentation	74
6.2	Active shape model search procedure	75

*LIST OF FIGURES***xii**

A.1	Required sample size for male population	86
A.2	Required sample size for female population	87
A.3	Updated sample size requirement	88
C.1	Manual landmark selection for first scenario	98
C.2	Manual landmark selection for first scenario	106

List of Tables

2.1	Mandibular landmarks	14
2.2	Cranial and Maxillary landmarks	15
3.1	Linear Measurements	28
3.2	Angular Measurements	29
3.3	Angular measurement comparison	32
3.4	Linear measurement comparison	33
3.5	Strong correlations found between measurements performed on the male population	34
3.6	Strong correlations found between measurements performed on the female population	35
3.7	Comparison of bilateral measurements	36
3.8	Comparison of measurements performed on subjects from different geographic locations	37
4.1	Variance captured by first three modes for male SSM	56
4.2	Variance captured by first three modes for female SSM	57
4.3	Specificity ranges of SSMs on various anatomical structures	58
4.4	Generality ranges of SSMs on various anatomical structures	58
5.1	First scenario: Surface-to-surface error	64
5.2	First scenario: Male measurement estimation comparison for right half	64
5.3	First scenario: Female measurement estimation comparison for right half	65
5.4	First scenario: Male measurement estimation comparison for left half	65
5.5	First scenario: Female measurement estimation comparison for left half	66
5.6	Second scenario: Surface to surface error	66
5.7	Second scenario: Male measurement estimation comparison	67
5.8	Second scenario: Female measurement estimation comparison	67

Nomenclature

Symbols

b	Weighting factor
cov	Covariance
H	Correlation matrix
$k(x, x')$	Covariance function
L	Landmark points
N	Normal distribution
O	Observed point set
P	Predicted point set
p	P-value
$p(x)$	Probability density function
R	Rotation matrix/Random shape instance
r	Correlation coefficient
T	Translation vector
t	Training set instance
u	Deformation
X, Y	Sets of measurements
Z	Z score
α	Type 1 error
β	Type 2 error
Δ	Distance discrepancy
λ	Variance
μ	mean
Σ	Covariance matrix
ς	Shape instance

ϕ	Principle component/mode of variation
Ω_r	Reference point set
Ω_t	Target point set

Abbreviations

<i>2D</i>	Two-dimensional
<i>3D</i>	Three-dimensional
<i>CAD</i>	Computer aided design
<i>CBCT/CT</i>	Cone beam computed tomography.....
<i>CPD</i>	Coherent point drift.....
<i>DICOM</i>	Digital Imaging and Communications in Medicine
<i>EM</i>	Expectation maximum
<i>GP</i>	Gaussian process
<i>GPA</i>	Generalised Procrustes alignment.....
<i>ICC</i>	Intraclass correlation coefficient
<i>ICP</i>	Iterative closest point
<i>MRC</i>	Medical Research Council
<i>PA</i>	Procrustes alignment.....
<i>PCA</i>	Principle component analysis.....
<i>PDF</i>	Probability density function
<i>RMS</i>	Root mean square.....
<i>RMSE</i>	Root mean square error
<i>SPM</i>	Sparse prediction model
<i>SSM</i>	Statistical shape model.....
<i>SVD</i>	Singular value decomposition.....
<i>VSR</i>	Virtual surgical reconstruction

Chapter 1

Introduction

1.1 Background

Orthognathic surgery involves correcting conditions relating to the jaw and face. These conditions/defects can be congenital¹ or acquired during life. Some of the main reasons for a patient requiring this surgery include malocclusion², facial deformities and the presence of tumors (Kim and Park, 2007). Orthognathic surgery not only treats functional and cosmetic issues, but also benefits the patient psychologically and socially. This surgery poses an extensive amount of risks and the difficulties are well documented. These risks include: nerve damage, infection, vascular disease, periodontal disease³ and bone necrosis⁴ amongst others (Martis and Karabouta 1984; Lanigan and West 1990; Schultes *et al.* 1998; Jacks *et al.* 1998; Mehra *et al.* 1999; Kim and Park 2007). Due to the seriousness behind most reasons for orthognathic surgery as well as the risks associated with it, the pre-surgery planning step is crucial (Kolokitha and Topouzelis, 2011).

For decades, manual implementation of cephalometric methods has been used as a pre-surgery planning technique (Kolokitha and Topouzelis, 2011). These methods predominately involve the surgeon analysing a lateral X-ray image of the patient's skull, where a prediction is made on the patient's ideal post-surgery mandibular structure. Cephalometric studies provide detailed information on ideal skull measurements and are used by surgeons as guidelines when performing these cephalometric predictions (Rao *et al.*, 2015). Predicting the shape of a structure as complex as the mandible from 2D data can prove to be extremely difficult, especially in situations where large sections

¹Abnormality present from birth

²Disharmony between the upper and lower teeth

³Infection that damages the gum and may destroy the jawbone

⁴Decay of bone tissue due to a lack of blood supply

of bone are to be removed. This difficulty in prediction often leads to a surgeon's estimations of mandibular geometry falling short of the patient's ideal mandibular structure. In situations such as this, the surgeon would have to alter the implant intraoperatively⁵. This intraoperative alteration to the implant is made possible by the implant's bendable nature. Traditionally, these implants are found in standard sizes and often provide unsatisfactory results (Singare *et al.*, 2017).

The recent advancement in 3D imaging modalities has led to the natural progression in implant design. Where previously, geometric predictions were made with only 2D data at the surgeon's disposal, surgical reconstructions can now be made in 3D space. Virtual reconstruction has made the design of mandibular implants a more intuitive process. This emergence in virtual surgical reconstruction (VSR), combined with the various rapid prototyping techniques commercially available, has allowed for these designed implants to be 3D printed with great accuracy (Al-Ahmari *et al.*, 2015). The design of custom patient-specific implants has improved surgical precision, whilst reducing overall operating time (Han *et al.*, 2017). Studies such as ones produced by Kondo *et al.* (2015) and Singare *et al.* (2017) report on cases where custom implants were used during surgery. All the surgeries were conducted smoothly, where no adjustments to the implants were required and no complications arose.

1.2 Motivation

During VSR, the most effective method in reconstructing the mandible is the mirroring technique. This technique involves assuming the mandible to be symmetrical across the sagittal plane. The disrupted region is replaced by the mirrored area on the healthy half of the mandible (Parthasarathy *et al.* 2009; Kondo *et al.* 2015). This reconstructed mandibular region serves as the template for the resultant 3D printed implant. Despite its success in clinical cases, the mirroring technique is limited to scenarios where symmetrical features are available. For instance, if the disruption on the mandible occurs in a region that overlaps the mandibular midline, then the mirroring technique cannot be used as a standalone method. This is due to anatomical disturbances occurring on both halves of the mandible in similar regions (Singare *et al.*, 2017).

Surgeons have come across a similar issue in the virtual reconstruction of the glenoid⁶. Generally, surgeons would make use of the contralateral⁷ bone

⁵Tasks taking place during the surgery itself

⁶Shallow surface on the scapula that articulates with the head of the humerus

⁷Denotes the side of the body opposite to which a structure occurs

as a template for glenoid reconstruction (Eraly *et al.*, 2011). Problems in this method arise when disorders, such as glenoid arthritis, affect both sides. Scalise *et al.* (2008) proposed a method of using a template model of the glenoid that can change size proportionally until it best fits the pathological⁸ glenoid. Singare *et al.* (2017) also reported the use of the template method during a mandibular reconstruction scenario where symmetrical characteristics were unavailable. The problem with template-based methods is that they do not take shape variability into account (Plessers *et al.*, 2018). A measurement estimation technique reported by Ganapathi *et al.* (2011) takes population variation into account in producing linear regression algorithms that predict certain clinically important glenoid measurements. Whilst this method is able to predict a limited set of measurements, recent studies proposed the use of statistical shape modelling as a means for estimating entire missing anatomical structures. Zhang and Besier (2017), Vanden Berghe *et al.* (2017) and Plessers *et al.* (2018) constructed a statistical shape model (SSM) of the femur, acetabulum⁹ and glenoid respectively. The models were all created for the purpose of VSR, where high quality reconstruction accuracies were reported. Zachow *et al.* (2005) advocates the use of a SSM for mandibular reconstruction purposes, especially for when the plane of symmetry is unavailable.

Based on the promising results obtained from studies using statistical methods to account for limitations present in current VSR applications, it is proposed that similar techniques can be applied for the reconstruction of the mandible. The methods present themselves as modular techniques that can offer estimates of correct mandibular geometry regardless of whether the plane of symmetry is present.

1.3 Aim and objectives

The aim of this study was to formulate a pre-operative virtual mandibular reconstruction technique for the South African population, whilst accounting for limitations present in current methods. This was to be achieved by retrospectively investigating the population's mandibular structure and developing methods based on statistical correlations that can be used to predict mandibular geometry from partial inputs. From this aim, the following objectives were formulated:

1. Cephalometric Analysis: Conduct a cephalometric analysis on the South African population. Using the correlations found between the cephalometric measurements, a sparse prediction model (SPM) is formulated. This SPM should be able to offer estimations of unknown measurements

⁸Something suffering/affected by disease

⁹Socket of the hip bone, into which the femur fits

(i.e. on the damaged area of the mandible) by receiving known values of certain observed measurements (i.e. on the healthy portion of the mandible).

2. Statistical shape model (SSM): Construct a SSM of the mandible. This SSM is based on finding the statistical correlations that exist amongst a dense set of coordinates that make up the mandible. Whilst the SPM serves to predict certain important mandibular measurements, the SSM should be able to predict the full mandibular geometry. This method relies on using known mandibular geometry (i.e. healthy portion of the mandible) as partial input in order to predict the unknown geometry (i.e. damaged portion of the mandible).
3. The effectiveness of both methods should be compared to each other as well as the mirroring method that is currently used in practice. This mirroring technique serves as the baseline.

The expected result of this study will offer surgeons and implant design engineers the tools to develop an estimate of the patient's mandible, in its healthy form, quickly and with ease. This would result in a more cost and time-effective means of pre-surgery planning as well as a more accurate implant, since the potential for human error in the design process would be reduced.

Chapter 2

Literature Study

Before delving into the construction of the prediction models, literature giving context to the project's objectives was first reviewed. This chapter initially offers a background of the mandible's morphology and its basic functions. Thereafter, reasons behind the need for orthognathic surgery as well as traditionally used methods of pre-operative planning are looked into. Finally, current methods of virtual reconstruction are discussed, as well as the limitations that still exist with these methods.

2.1 The Mandible

The mandible or lower jaw, is the strongest bone in the human face. It holds the lower teeth in place and is the only movable bone of the skull (Tortora and Derrickson 2008; Standring 2015). This movement comes about via its articulation with the temporal bones at the temporomandibular joints (see Figure 2.1). The bone is formed in the fetus during the merging of the left and right mandibular prominences. The area where these sides join is called the mandibular symphysis and is still visible as a faint ridge. Like other symphyses in the body, this is a midline articulation where the bones are joined by fibrocartilage, but this articulation fuses together in early childhood (Fehrenbach and Herring, 2015). The mandible can be seen as having seven different regions. Using information provided by Harnsberger *et al.* (2006), Standring (2015) and Fehrenbach and Herring (2015), these regions are described below. A visualisation of these regions is shown in Figure 2.2.

1. **Body:** The body (Figure 2.2a) or base of the mandible is a large horizontal section that is slightly rectangular in shape. The mental foramen (opening for the terminal branches of the inferior alveolar nerve) is found on the body, usually below the 2nd premolar tooth.

2. **Alveolar process:** The alveolar process (Figure 2.2b) is superior to the body and contains the roots that hold the 16 mandibular teeth.
3. **Parasymphiseal:** The parasymphiseal (Figure 2.2c) represents the anterior surface of the mandible located adjacent and inferior to the body and alveolar process respectively. The mandibular midline, known as the mandibular symphysis or symphysis menti, is found in this region. The symphysis menti is often used as the mandibular plane of symmetry.
4. **Angle:** The angle (Figure 2.2d) of the mandible is the juncture between the body and the ramus.
5. **Ramus:** The ramus (Figure 2.2e) is the second largest region of the mandible and extends from the mandibular angle at roughly 110 degrees away from the body. The outer surface of the ramus serves for the attachment of the masseter muscle. This muscle connects the mandible to the cheekbone and plays a major role in the chewing motion. The groove present at the posterior part of the ramus, known as the sigmoid notch (Figure 2.2f), separates the two processes (coronoid and condylar).
6. **Coronoid process:** The coronoid process (Figure 2.2g) is a flat and triangular shaped protrusion extending from the ramus. This section serves for the attachment of the temporalis muscle, that assists in connecting the mandible to the temple. This muscle also contributes to the chewing motion.
7. **Condylar process:** The condylar process (Figure 2.2h) is the more anterior process extending from the ramus. This region forms the lower bony portion of the temporomandibular joint. Unlike the coronoid process, the head of the condylar process is rounded, allowing for smooth articulation with the temporal bone.

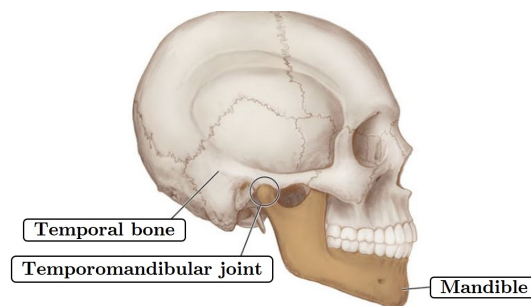


Figure 2.1: Mandible's articulation with the temporal bone
(Illustration: Fehrenbach and Herring (2015))

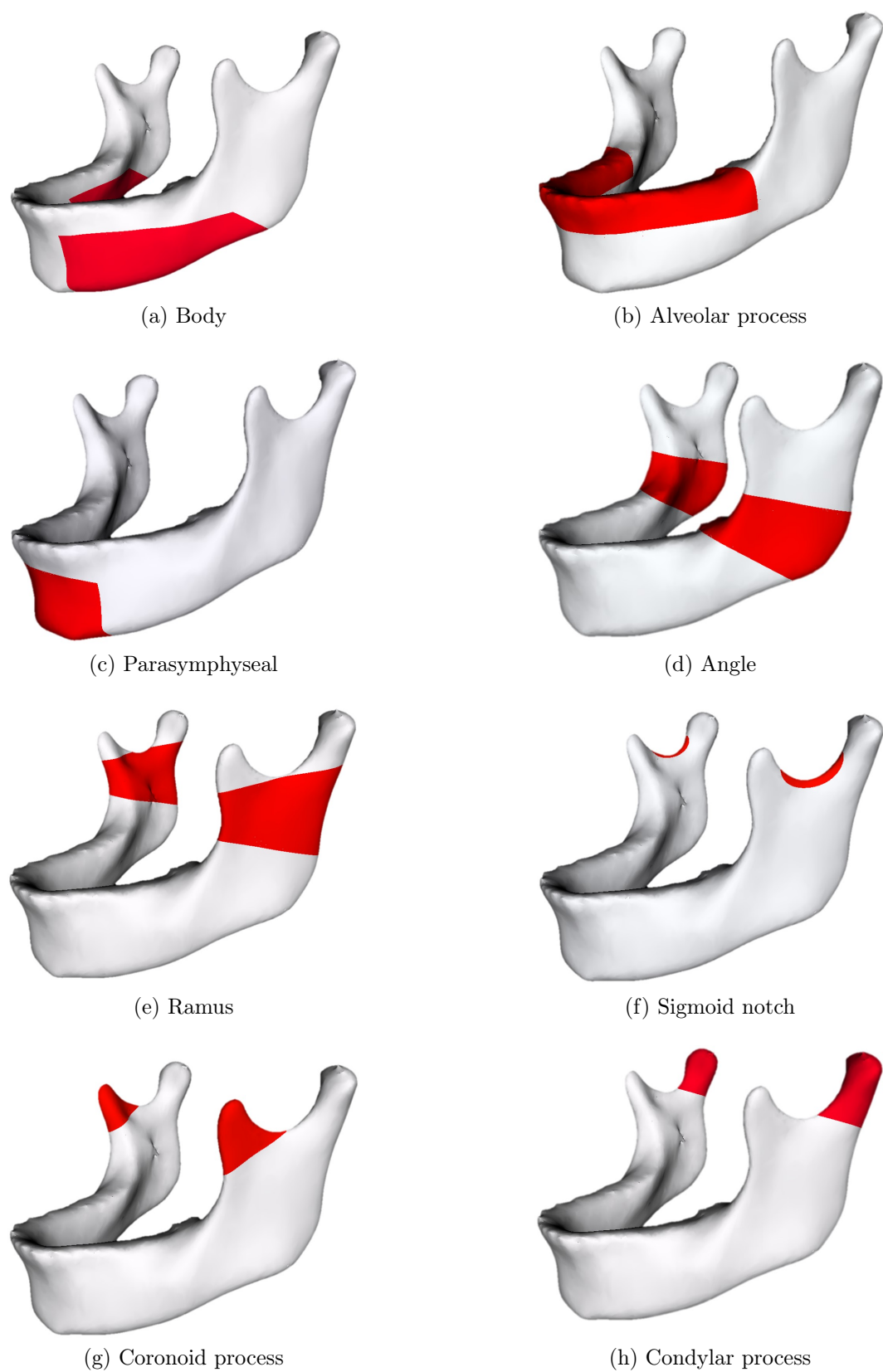


Figure 2.2: Regions of the mandible
(Illustration: RL Gillingham)

2.2 Orthognathic surgery

Orthognathic surgery, also referred to as corrective jaw surgery, is the surgical application of correcting deformities related to the jaw that cannot be treated easily using braces. Amongst the most common reasons for such deformities, are tumors and craniofacial microsomia¹ (Zachow *et al.*, 2005). For such a surgical procedure, osteotomies² are usually performed, after which osteodis-traction³ or osteosynthesis⁴ could follow. These procedures often include the use of bone grafts to replace missing bone, when large portions of the mandible are removed. This process is visualised in Figure 2.3. Figure 2.3a shows the removal of the affected bone (osteotomy) as well as the fixation of a titanium implant to the remaining bony sections (osteosynthesis). Figure 2.3b illustrates the attachment of bone grafts to the remaining mandibular sections and titanium implant. Usually, these bone grafts are taken from the femur or iliac crest (Qaisi *et al.*, 2016). Other common non-tumor related deformities requiring orthognathic surgery are shown in Figure 2.4 and described below using literature provided by AAOMS (2015).

1. **Open bite:** There are two main incidents of open bite, namely: anterior and posterior open bite. An anterior open bite occurs when the front teeth fail to touch and no overlap is present between the upper and lower incisors. A posterior open bite is when the posterior teeth fail to make contact with their corresponding teeth. To correct such a deformity, a portion of the bone in the upper tooth bearing region of the jaw, below both eye sockets, is removed. The upper jaw is then aligned correctly and secured using titanium plates (Figure 2.4a).
2. **Protruding lower jaw:** This condition, also known as mandibular prognathism, arises in situations where the mandible outgrows the maxilla. This condition is corrected surgically by separating the rear of the mandible from its front portion so that the front section can be moved backward until a suitable alignment has been achieved (Figure 2.4b).
3. **Receding lower jaw:** Opposite to mandibular prognathism, a receding lower jaw (maxillary prognathism) is when the maxilla has outgrown the mandible, resulting in a pronounced overbite. To correct such a condition, the mandible is separated into two sections. The separation usually occurs in the area just behind the molars. The front section of

¹Lack of development in craniofacial structures

²Surgical cutting of a bone in order to alter its alignment

³Gradual separation of severed bone, allowing the bones' self-healing process to fill the gap

⁴Stabilizing the ends of fractured/separated bone by using implantable devices

the mandible is repositioned forward and held in place using titanium plates (Figure 2.4c).

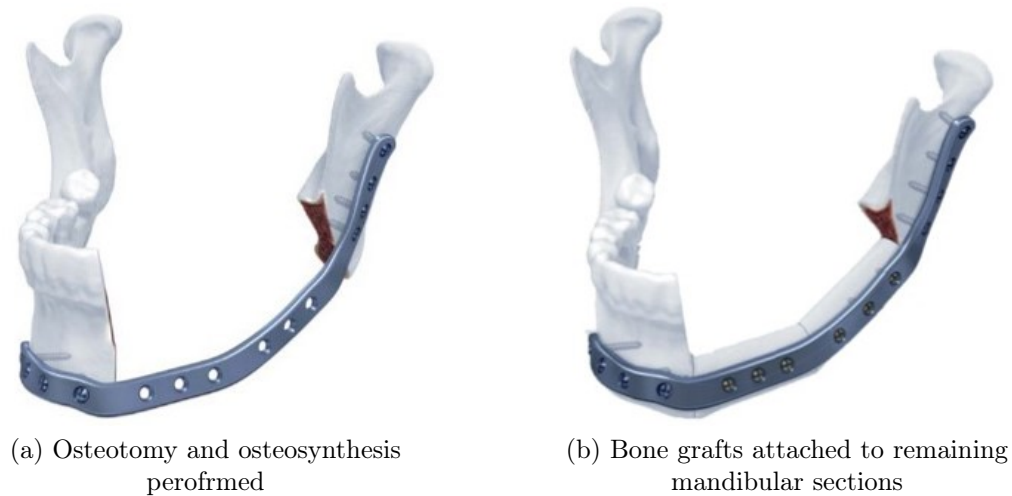


Figure 2.3: Orthognathic surgery for tumor resection
(Illustration: Synthes (2012))

Pre-surgery planning is crucial to the success of the final surgery (Kolokitha and Topouzelis, 2011). Not only does this pre-surgery step assist the surgeon in obtaining an estimate for the patient's ideal mandibular geometry, but also offers the patient him/herself a view of the predicted final results. The communication of the treatment and predicted result to the patient is important in bridging the gap in understanding between the surgeon and patient, as well as obtaining the patient's informed consent (Friede *et al.* 1987; Kolokitha and Topouzelis 2011). One of the most routine and traditionally used methods in diagnosis and treatment planning is cephalometrics (Kolokitha and Topouzelis, 2011). Using cephalometrics also enables the surgeon to evaluate the changes following the surgery. Cephalometric methods usually involve recording desired cephalometric measurements from a patient's cephalogram⁵, and comparing these measurements to the normal range (Rao *et al.*, 2015). These cephalometric norms are obtained by cephalometric studies/analyses done on the population in question.

Using these cephalometric norms, the surgeon is able to obtain a sparse representation of the patient's ideal post-surgery mandibular geometry. This sparse representation isn't always sufficient in offering the surgeon the desired confidence in estimating this geometry. As such, more modern techniques such

⁵X-ray image of the craniofacial region

as 3D virtual surgical reconstruction (VSR) have been preferred to, or used in combination with traditional cephalometric methods. VSR involves using 3D imaging modalities to obtain a more representative view of the defected site, whereafter a virtual reconstruction of this region takes place. In orthognathic and craniomaxillofacial ⁶ VSR, the assumption of facial symmetry is most commonly used, where the defected site is replaced by the corresponding unaffected area on the opposite half of the skull.

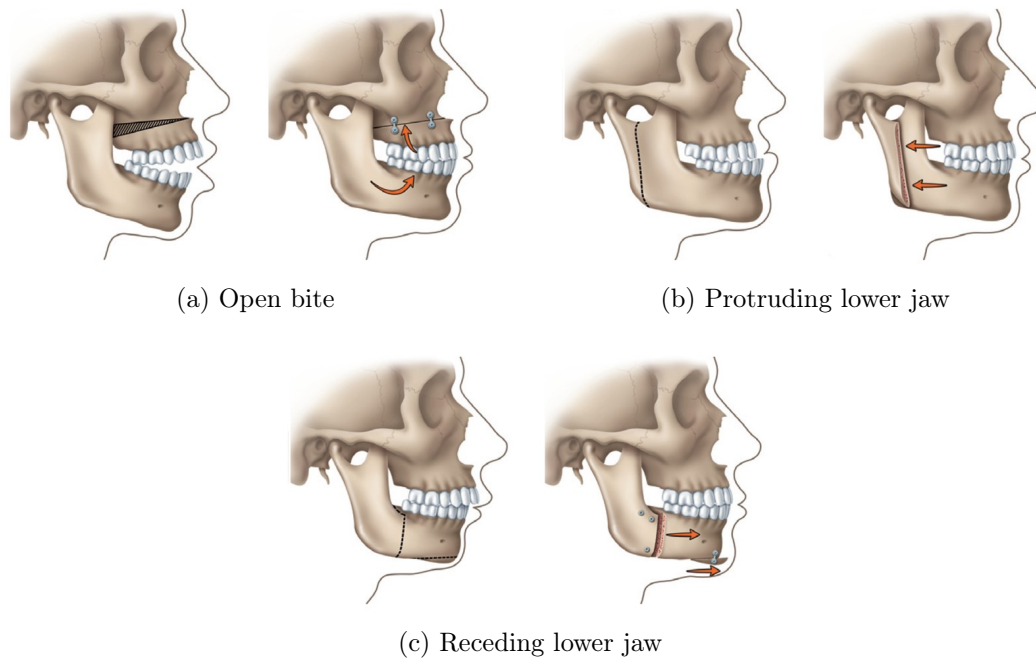


Figure 2.4: Common orthognathic deformities
(Illustration: AAOMS (2015))

2.3 Cephalometry

Cephalometry refers to the study and measurement of the head (usually the human head). Cephalometry has many applications such as in clinical research, forensics, obstetrics⁷ and ancestral tracking (Goldberg *et al.* 1966; Kallenberger and Pilbrow 2012). In its clinical application, cephalometry is referred to as a cephalometric analysis. During such a study, an analysis of the dental and skeletal relationships of a human skull is undertaken. The results are used by surgeons as a tool for planning patient-specific treatments (Tenti, 1981). In most cases, these analyses involve the identification of desired/useful landmark positions and finding the norms of clinically important skeletal measurements.

⁶Relating to any parts of the head enclosing the brain and face

⁷Branch of medicine relating to pregnancy, child birth and post-pregnancy period

Some studies go as far as to find relationships/correlations that exist between these measurements. When conducting a cephalometric analysis, it is important that all head data being observed is taken according to the same frame of reference. Figure 2.5 displays the location of certain important cephalometric planes used by researchers to obtain a frame of reference (Cheung *et al.* 2011; Bayome *et al.* 2013).

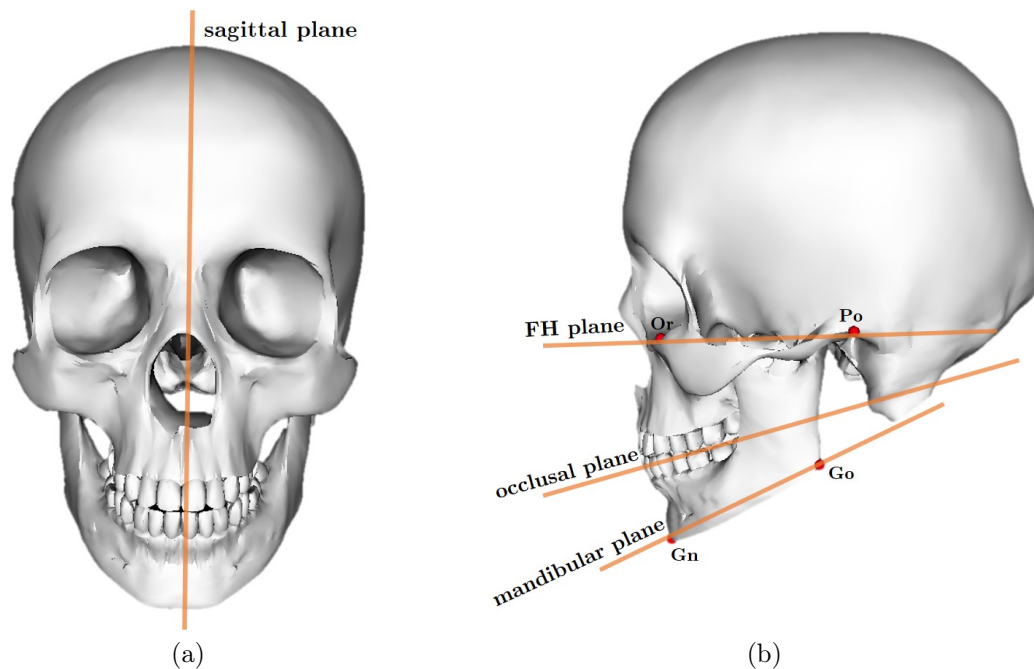


Figure 2.5: Important cephalometric planes
(Illustration: RL Gillingham)

2.3.1 Cephalometric analysis

Cephalometry was first used as a means to study and understand craniofacial growth and its development. This use gradually progressed to also forming cephalometric norms for surgeons to use as guidelines of correct facial form during orthodontic and orthognathic surgeries (Baruah *et al.*, 2009). Pioneering analyses, such as those produced by Downs (1948), Steiner (1953) and Ricketts (1961), were conducted by analysing lateral cephalograms of multiple subjects. A diagrammatic representation of a typical lateral cephalogram is shown in Figure 2.6. On each cephalogram, anatomical landmarks would be identified and measurements based on these landmarks would be recorded. The average values obtained for the measurements would serve as the cephalometric norms. The norms published from these early studies were used as the standard for analysing population groups all over the world (Baruah *et al.*, 2009). These studies were primarily performed on Caucasians. Over time, researchers no-

ticed that significant morphological variation existed between different ethnic groups. It therefore became clear that these Caucasian cephalometric norms were not sufficient in treating other ethnic groups or populations from different geographic locations. As a result, analyses have since been performed on population-specific groups.

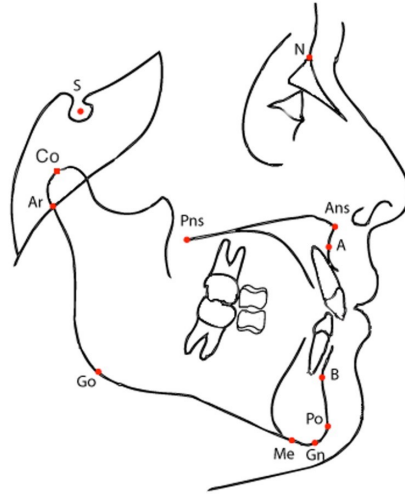


Figure 2.6: Diagrammatic representation of a lateral cephalogram
(Illustration: Scala *et al.* (2012))

During the undertaking of a cephalometric analysis, the identification of landmarks is crucial to the accuracy of the data (Asi *et al.*, 2014). Therefore, it is essential to ensure that the decided upon landmarks are easily identifiable and analogous to the general human skull. Early cephalometric analyses relied on lateral cephalograms for the identification of landmarks. The 2D nature of these cephalograms has raised certain questions about their reliability. Amongst the drawbacks of using these 2D cephalograms are the errors involved in landmark identification, the projection of these landmarks in 2D space, superimposition of anatomical structures and the implications of incorrect head orientation (Ahlqvist *et al.* 1983; Baumrind *et al.* 2003). Landmark identification has become a more intuitive and precise process since the inception of high-quality cone-beam computed tomography (CBCT or CT) of the facial region (Cevitanes *et al.*, 2007). This initiated the era of 3D imaging in orthodontics. Amongst the advantages of CT include the ability to assess a scanned image from three planes as well as obtain 3D models with a lack of distortion and overlapping structures (Ludlow *et al.*, 2009). An added benefit of using CT scans is that fine adjustments to the head orientation of the patient is not needed as the 3D nature of the imaging results in the landmarks maintaining their spatial relationships (Ludlow *et al.*, 2009). Due to these advantages, researchers have begun to develop cephalometric norms based on analysing 3D data. Studies such as those published by Cheung *et al.* (2011) and

Vahdettin *et al.* (2016) have reported 3D cephalometric norms for the Chinese and Turkish-Cypriot populations respectively. Bayome *et al.* (2013) presented a similar study, except that the linear relationships that exist between the measurements were also reported.

These linear relationships can prove to be extremely useful if strong linear correlations are found between measurements. If strong correlations exist between measurements, then the unknown value of one measurement can be estimated using the known value(s) of one or more measurements. Ganapathi *et al.* (2011) reported on a study relating to the scapula using a similar concept. In this study, 58 scapulae were analysed, where 3 measurements were recorded for each subject. These measurements were the anterior glenoid wall angle (AGWA), Resch angle (RA) and glenoid version (GV). Linear correlations were found between the measurements and were used to create linear regression equations. These equations were used to estimate unknown glenoid version measurements, with satisfactory results. Tables 2.1 and 2.2 lists and describes landmarks relevant to the current study, found on the mandible, maxilla and other cranial regions as identified by Bayome *et al.* (2013), Proffit *et al.* (2006) and Abraham (2014). The positioning of the desired landmarks can be visualised in Figures 2.7 and 2.8.

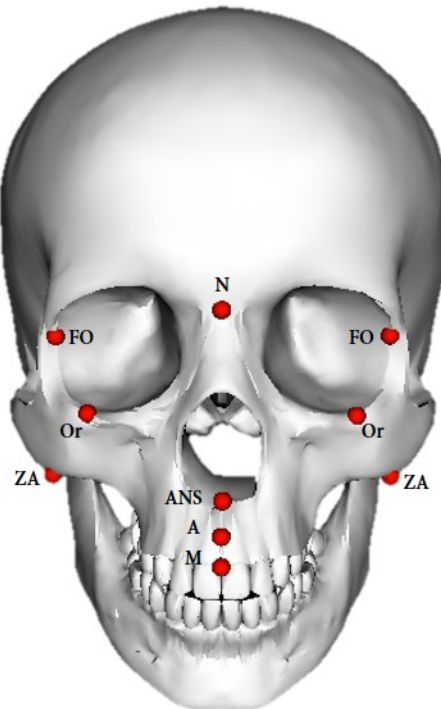


Figure 2.7: Cranial and maxillary landmarks
(Illustration: RL Gillingham)

Table 2.1: Mandibular landmarks

Landmarks	Symbol	Description
B point	B	The most posterior point between the infradentale and pogonion on the sagittal plane
Pogonion	Pg	The most anterior point on the chin, found along the sagittal plane
Gnathion	Gn	The point found midway between the menton and pogonion on the sagittal plane
Menton	Me	The most inferior point on the chin, found along the sagittal plane
Gonion	Go	The most inferior and posterior point found on the angle.
Sigmoid notch	Sig	The most inferior point found on the sigmoid notch
Condylion	Co	The most posterior point found on the condyle
Lateral condyle	Co-out	The most lateral point found on the condyle
Medial condyle	Co-in	The most medial point found on the condyle
Infradentale	Id	The highest point of the gum between the two central incisors of the lower jaw
Coronoid process apex	CP	The most superior point found on the coronoid process

Table 2.2: Cranial and Maxillary landmarks

Landmarks	Symbol	Description
Cranial Landmarks		
Nasion	N	The intersection of the nasal and frontonasal sutures found on the sagittal plane
Sella	S	The midpoint of the sella turcica found on the sagittal plane
Porion	Po	The most superior point on the upper margin of the ear canal
Orbitale	Or	The most inferior point on the lower rim of the orbit
Frontomalare orbitale	FO	The point on orbital rim intersecting with the frontozygomatic suture
Maxillary Landmarks		
Anterior nasal spine	ANS	The most anterior point on the base of nose
Posterior nasal spine	PNS	The most posterior point on the base of nose
Zygomaxillary anteriore	ZA	The center of the concavity of the zygomatic process of the maxilla
A point	A	The deepest point on the anterior section of the maxilla found along the sagittal plane

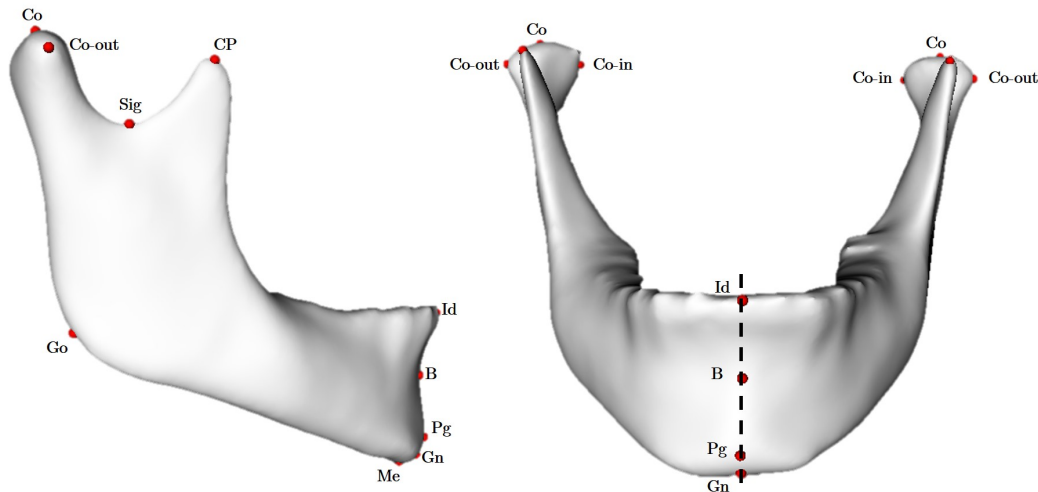


Figure 2.8: Mandibular landmarks
(Illustration: RL Gillingham)

2.3.2 Cephalometric prediction

Cephalometric analyses have been used as a surgical pre-planning guide for decades. Traditionally, this cephalometric prediction has been accomplished manually. Surgeons would place acetate paper over the patient's cephalogram, on which tracings of desired/predicted post surgery location of hard tissue would be drawn (Kolokitha and Topouzelis, 2011). Cephalometric norms from analyses done by researchers would be used as an indication for the correct geometric measurements. A generalised form of this procedure is known as the overlay tracing method. This technique is the simplest method of surgical prediction for mandibular reconstruction scenarios (Kolokitha and Topouzelis, 2011). The steps required to perform the overlay tracing method are as follows:

1. The patient's cephalogram is traced on a sheet of paper.
2. All areas not being affected during the surgery are traced onto a second transparent acetate sheet. This second sheet is known as the overlay tracing.
3. The overlay tracing is superimposed on top of the original tracing. The original tracing is manoeuvred until the correct occlusion⁸ is visualised. The rest of the mandibular region is traced onto the overlay tracing. As a result, the transparent overlay has the post-surgical prediction traced onto it.

⁸Relationship between the maxillary and mandibular teeth when they are in contact with each other

4. The overlay and original tracings are re-orientated back to their original positions. This is so that the difference between the patient's current and post-operative predicted bone structure can be observed and measured.

Many variants to the overlay tracing method have been devised and used by surgeons. One of the earliest variants was described by Cohen (1965) to correct mandibular prognathism. For this method, a divider was used to measure the amount by which the mandible would have to move back to correct the patient's underbite. This measurement took place on the original cephalogram (Figure 2.9a). An acetate paper tracing of the mandibular region, with an estimation of the soft tissue profile, was then made and cut out (Figure 2.9b). This cut-out section was placed on the original image and moved along the occlusal plane by the distance originally measured by the divider (Figure 2.9c). Once the cut-out section was correctly in place, the section was outlined (preferably in a different colour) so as to observe the predicted post-operative facial appearance.

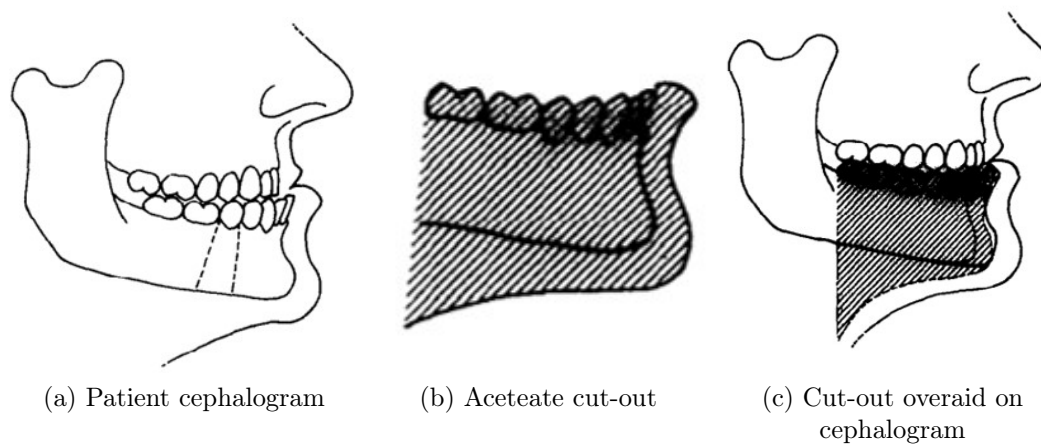


Figure 2.9: Cephalometric prediction of mandibular prognathism
(Illustration: Cohen (1965))

McNeill *et al.* (1972) offered an alternative method for cephalometric prediction. With this method, casts of the maxillary and mandibular dental regions were made and aligned to correct occlusion using an articulator⁹. An overlay tracing of the mandibular regions not to be affected during the resultant surgery was drawn and placed over the patient's original cephalogram. This overlay tracing was manoeuvred over this cephalogram until the dental occlusion mimicked that of the aligned casts.

⁹Mechanical device used to clamp dental casts

A technique was introduced by Henderson (1974) that differs slightly to the before-mentioned methods. With this technique, a cephalogram is combined with a transparency of the patient's external face. The transparent image is sectioned along predicted surgical lines that would take place on the bone during the surgery itself. The sectioned transparency pieces of the patient's face are then orientated until a suitable facial alignment has been achieved. The main advantage of this method is that the patient is able to gain an idea of the external view of his/her face post surgery.

These manual cephalometric prediction techniques are not as widely used anymore. This is mainly due to their time-consuming nature and reliance on the experience and skill of the surgeon performing the techniques. As a result, various software programs currently exist that allow for the manipulation of cephalogram images and recording of desired measurements. These programs essentially mimic the manual methods previously described, whilst reducing the amount of human-error and total pre-operative planning time. Despite the efforts to translate the manual prediction methods to more automated and computerized ones, limitations in these techniques still exist. The main limitation in using these methods is that they are limited to explaining the reconstruction area in 2D.

2.4 Virtual surgical reconstruction

3D pre-operative planning and VSR of bony matter have been present for over 20 years, yet has gained momentum in the late 2000s (Kirke *et al.* 2016; Han *et al.* 2017). VSR accounts for many limitations present in previous methods, with the main advantage being to plan complex reconstruction movements in 3D space (Zielinski *et al.*, 2015). VSR has been said to not only increase surgical precision, but also reduce the operating time spent during surgery. Amongst the greatest advantages of using VSR in mandibular reconstruction, is in the design and preparation of patient-specific mandibular implants (Han *et al.*, 2017). This design of patient-specific implants has resulted in less intraoperative changes during surgery.

During the design of a mandibular implant, surgeons can come across two different cases of mandibular reconstruction. The first of these cases is when the disrupted area occurs on the one half of the mandible but not on the other. An assumption of mandibular symmetry is used in order to create an implant to replace the damaged region. The second case is when the reconstruction process cannot be guided by symmetry as anatomical disturbances occur on both halves of the mandible in similar regions (Zachow *et al.*, 2005). In a case such as the latter, the surgeon's intuition and experience are crucial in estimating what implant geometry would be suitable in replacing the damaged

mandibular region (Jurda *et al.*, 2015).

2.4.1 Use of symmetry for implant design

Making use of tomographic images from the CT scan that a patient typically undergoes before diagnosis, a virtual 3D model of the patient's mandible is created. Once a virtual model has been formed, the disrupted area on the mandible is identified. This area is then removed from the model. If the disturbance occurs only on one half of the mandible, then the assumption of mandibular symmetry is used, where the unaffected region on the opposite half of the model is mirrored to replace the damaged region (Parthasarathy *et al.* 2009; Kondo *et al.* 2015). The result is a 3D model of a healthy looking mandible. Al-Ahmari *et al.* (2015), Mohammed *et al.* (2016) and Manmadhachary *et al.* (2017) discuss this technique during their respective implant design processes. An illustration of this mirroring technique is shown in Figure 2.10. This model forms a basis for the shape of the resultant titanium plate or mesh that is to be designed. Using Computer Aided Design (CAD) software, a plate is designed to take the shape of the reconstructed area that was previously damaged. The plate design is subsequently 3D printed in titanium and eventually used to connect the remaining pieces of mandible together after the damaged area is cut away (Al-Ahmari *et al.*, 2015).

Singare *et al.* (2017) discusses cases in which the mirroring method was used during various reconstructions. The first case was for a 50-year-old male who had already undergone mandibular reconstruction. For his initial surgery, a standard implant was used that was bent intraoperatively to best fit his mandibular structure. Months after this surgery took place, this implant had fractured. For the patient's second surgery, a custom patient-specific implant was made by mirroring the unaffected right half of the mandible. The implant was inserted during surgery without any further adjustments to the implant. Another pathological case described by Singare *et al.* (2017) was for the maxillary bone resection surgery of a 34-year-old female. Like with the mandibular case, the healthy half of the patient's maxilla was mirrored over to replace the damaged region using 3D imaging software. This mirrored segment was 3D printed in titanium and inserted during the resultant surgery. Again, no complications arose. This emphasises the mirroring technique's effectiveness, not only in mandibular reconstruction scenarios, but also for other craniomaxillofacial surgeries.

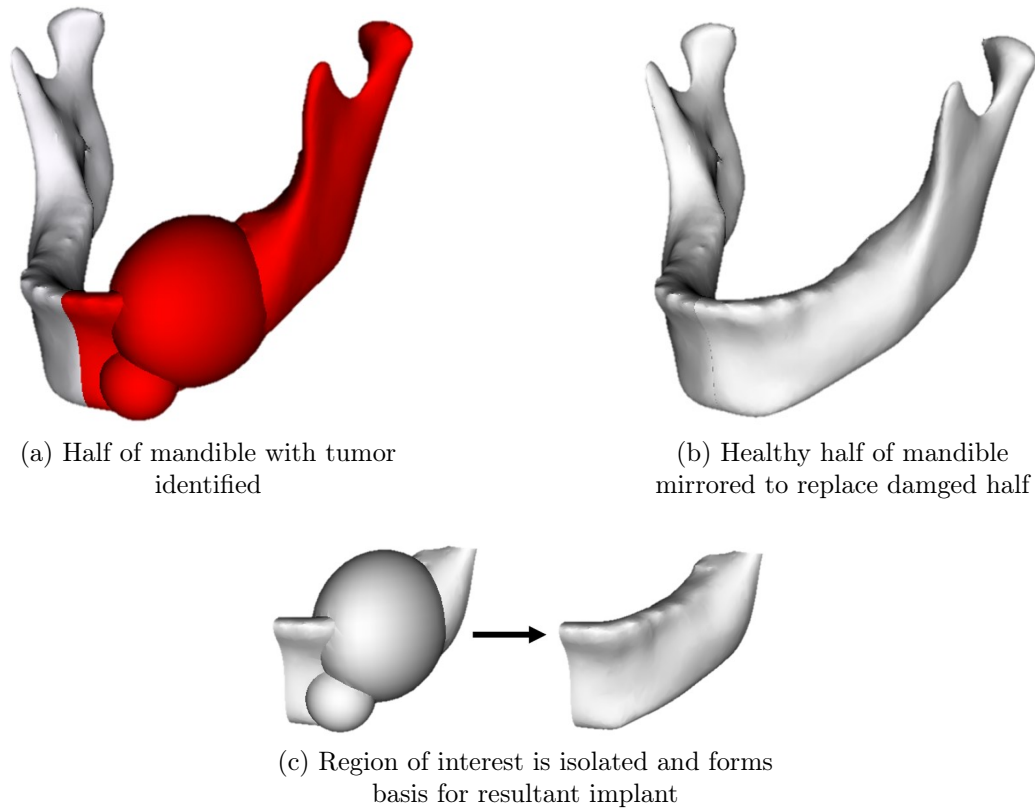


Figure 2.10: Mirroring virtual reconstruction technique
(Illustration: RL Gillingham)

2.4.2 Design without the use of symmetry

In cases where the damaged area occurs on both halves of the mandible in similar regions, the use of symmetry alone cannot be used to create an estimate of the mandible's healthy geometry. Traditionally in situations like this, implants that come in standard sizes are used. These implants are bent intraoperatively to match the patient's mandibular structure as best as possible, where a surgeon's intuition and mental image of a regular-shaped mandible is crucial (Zachow *et al.*, 2005). An illustration of such an implant is shown in Figure 2.11. These plates pose a challenge in adapting them to the patient's mandibular structure, where unsatisfactory functional results usually occur post-surgery (Singare *et al.*, 2017). Not only do these standard sized plates offer unsatisfactory results, but they often fail structurally. This failure occurs predominantly at the area of bending. It is for this reason that custom patient-specific implants are desired, that closely resemble the patient's ideal mandibular geometry, where minimal (if any) intraoperative bending of the implant is needed.

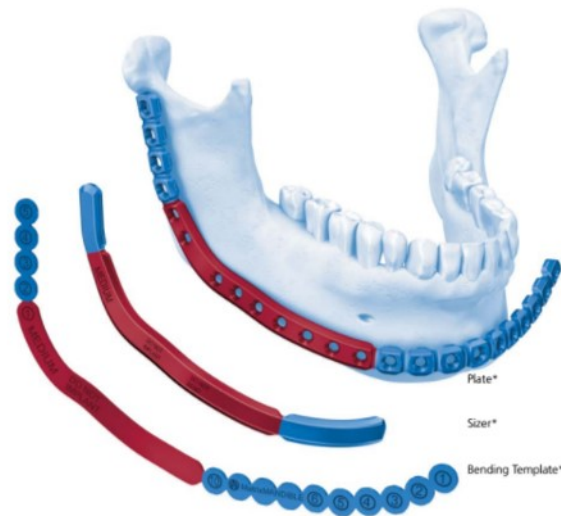


Figure 2.11: Bendable mandibular implant
(Illustration: Synthes (2012))

Singare *et al.* (2017) describes a case where a custom implant was made for a patient suffering from mandibular osteosarcoma¹⁰, where the mirroring method couldn't be used. The patient, 43 years of age, underwent a prior surgery during which a traditional bendable plate was inserted. Despite the surgeon's efforts, this plate failed to match the patient's mandibular morphology. Due to the implant's failure, the patient lost all oral function. For the subsequent surgery, a custom implant was proposed. The portion of mandible resected during the prior surgery, exceeded past the mandibular plane of symmetry. As a result, the mirroring technique alone could not be used for the virtual reconstruction of the disrupted area. First, the remaining undamaged area of the mandible was mirrored to the defected half. The region not accounted for, was reconstructed by scaling a similar mandibular model from a database, until it matched the missing area as well as possible. The resultant implant was successfully inserted during surgery without any further adjustments.

When the mirroring method cannot be used in its entirety, the difficulty in designing custom implants is increased, especially when similar virtual anatomical models are not available as a template. Linear regression, previously mentioned in Section 2.3.1, could be used to estimate certain important mandibular measurements based on the correlations that they have with other recorded measurements. This technique, although proven effective for predicting unknown variables on other anatomical structures, offers an extremely sparse estimation for a shape that is complex in shape (Plessers *et al.*, 2018). Recently, research has been done on the use of statistical shape modelling as a method

¹⁰A type of cancer that originates in the cells that form bones

for virtual reconstruction. Unlike the measurement estimation techniques, statistical shape modelling is able to offer a full representation of the geometry to be estimated. Plessers *et al.* (2018) investigated the use of a statistical shape model (SSM) to reconstruct glenoid bone defects. This was due to the amount of information relating to the glenoid joint predicted by previous methods being very limited. A SSM presents itself as a mean shape of a population, that can morph into any other shape within the variation limits described by the training data used to create the model (Plessers *et al.*, 2018). This model is able to estimate the most likely shape of missing/damaged geometries by receiving the healthy portion of the anatomical structure as partial input. Plessers *et al.* (2018) reported good results when using the SSM to virtually reconstruct glenoid joints. Studies by Zhang and Besier (2017) and Vanden Berghe *et al.* (2017) also investigated the use of statistical shape modelling for reconstruction purposes, where they implemented the technique on the femur and acetabulum respectively. Both studies reported high-quality reconstruction errors that compared favourably to other clinically relevant methods.

Limited literature exists on the use of statistical shape modelling for the reconstruction of the mandible. Zachow *et al.* (2005) advocates the possibility of using a SSM for mandibular reconstruction purposes. During this pilot study, a SSM was created from training data consisting of 11 mandibular instances. The author reported promising preliminary results, yet no comparisons were made with other clinically implemented methods (such as the mirroring technique). Abdolali *et al.* (2017) recently constructed a SSM of the mandible from a more comprehensive training set (84 mandibles). This study, however, investigated the use of a SSM for automating the segmentation of mandibles from CT scans rather than its virtual reconstruction ability.

2.5 Summary

The main objective of this study is to devise a method to assist surgeons during the virtual surgical reconstruction of the mandible. The literature behind traditional and virtual methods of reconstruction was reviewed. Traditional methods of geometry prediction and the use of implants that are bent intraoperatively have been shown to have notable shortcomings. Using VSR to create custom patient-specific implants has led to better results with fewer complications. The design of these custom implants has proved difficult in situations where the plane of symmetry is unavailable. Recent studies have suggested that forming a SSM of the anatomical structure in question may be used to overcome this complication.

Chapter 3

Cephalometric Analysis

As mentioned earlier in Chapter 2, cephalometric studies have played an integral role in the treatment planning of orthognathic surgeries over the years. The results of these studies are generally represented by cephalometric norms that are used to offer an indication of correct geometrical measurements that should occur on the patient's skull. The current study offers these norms for the South African population, whilst also drawing correlations between the various cephalometric measurements included within the study.

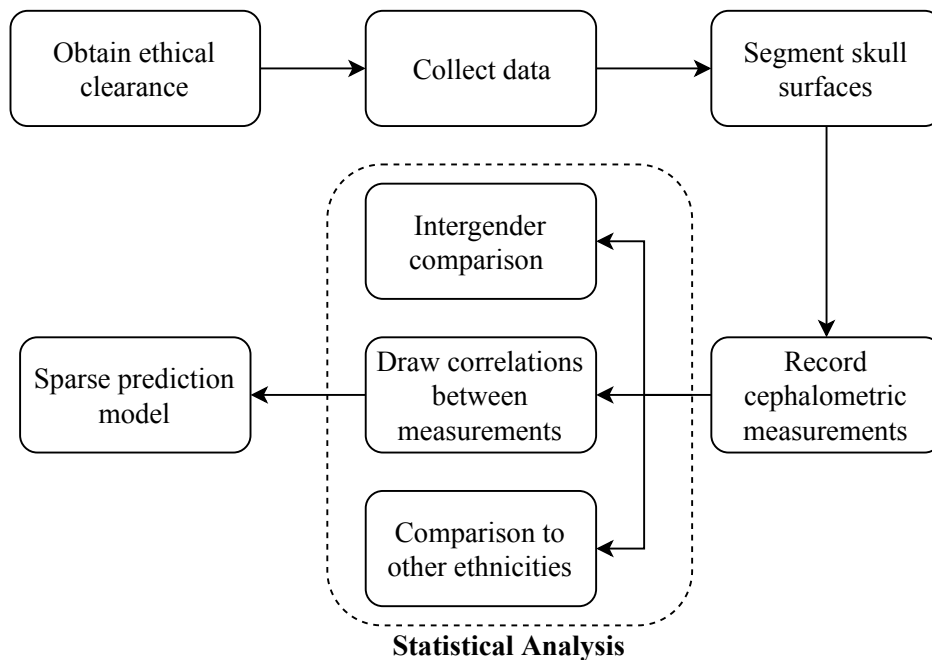


Figure 3.1: Cephalometric analysis methodology
(Illustration: RL Gillingham)

The findings from this study serve to offer useful insight into the morphology of the mandible as well as gender dimorphism in mandibular structure. A comparison was also made between the findings from the current analysis and other similar analyses performed on subjects from various geographic locations. The correlations found between the measurements were used to create a sparse prediction model (SPM), that can predict certain unknown measurements from the partial input in the form of known/healthy measurements. Figure 3.1 displays the logical flow of task completion in order to successfully conduct the cephalometric analysis.

3.1 Ethical clearance and data collection

In order to retrospectively analyse previous patient data, ethical clearance was required. To obtain this clearance, the project had to be conducted in accordance with internationally recognized standards and the guidelines of:

1. the Declaration of Helsinki
2. the South African Guidelines for Good Clinical Practice
3. the Medical Research Council's (MRC) Ethical Guidelines for Research.

After this ethical clearance had been granted, patient data could be collected from the hospital's database. Due to patient confidentiality, the patient's CT data was loaded on a private, password protected computer. This data was given a unique randomized code that's independent to the patient's details. By doing this, the data remained anonymous and the patient's identity was never revealed. Care was taken to collect an equal (approximately) amount of male and female scans. This is due to a separate statistical analysis that had to be done on both genders as a result of morphological differences that may exist between them. An important part of a clinical study is the determination of the sample size. Before this calculation could take place, certain factors, as described by Kadam and Bhalerao (2010) and Pandis *et al.* (2011), had to be decided upon:

1. Effect size: The minimum difference between two sample populations that would be considered significant. The magnitude of the effect size is most preferably estimated by referring to similar studies in literature (Kadam and Bhalerao, 2010). The study performed by Bayome *et al.* (2013), which looked at the cephalometric differences between male and female subjects of the Korean population, is closely related to the cephalometric analysis conducted during the current study. As a result, the effect size for each measurement recorded in that study was determined. The smallest effect size was chosen for the sample size calculation.

2. Standard deviation (σ): This is the estimated shared standard deviation between the two sample populations. Like the effect size, this standard deviation should be determined by examining similar studies in literature.
3. Type 1 error (α): A type 1 error refers to the probability of falsely inferring a significant difference. α was chosen to be 0.05.
4. Type 2 error (β): Conversely to a type 1 error, a type 2 error is the probability of failing to notice a significant difference. This error was chosen to be 0.2. The power of a study is equal to $1-\beta$.

With the decided upon parameters, the required sample size was calculated using Equation 3.1, where n_{tot} , Z_α , $Z_{1-\beta}$, σ and Δ refer to the sample size, Z scores corresponding to the α and $1-\beta$ values, the shared standard deviation and the chosen effect size respectively (Chow *et al.*, 2017). q_1 and q_2 refer to the proportion of subjects that are in the two groups being investigated.

$$n_{tot} = \frac{\left(\frac{1}{q_1} + \frac{1}{q_2}\right)(Z_\alpha + Z_{1-\beta})^2 \sigma^2}{\Delta^2} \quad (3.1)$$

The sample size required, using the chosen parameter values, was calculated to be 68, with 32 and 36 of the 68 belonging to the male and female populations respectively. The unequal required sample sizes was due to the difference in the amount of male and female scans acquired during the study performed by Bayome *et al.* (2013) (18 male and 20 female). This result was validated using Matlab's built-in sample size function, where the results thereof can be seen in Appendix A. For conservativeness, 40 scans for each gender were obtained, with ages of 25 ± 4.3 years and 27 ± 4.2 years for the male and female subjects respectively. Once results from the current study were obtained, this sample size calculation was repeated, this time with parameters obtained from the current study. If the results of the study were to offer unsatisfactory or inconclusive results, more data would have been collected. It was important to ensure that all the required data was collected before the ethical clearance expired. Each CT scan had a spatial resolution of between 0.5 and 0.65 mm in the X, Y and Z directions. Once obtained, these scans were converted to a DICOM (Digital Imaging and Communications in Medicine) format so that they could be opened and observed using medical imaging software. The desire was to develop and analyse cephalometric relationships for a healthy and fully developed skull. Therefore, the following inclusion criteria was placed on the obtained patient scans :

1. CT scans of patients with normal occlusion with a balanced facial structure were used.

2. Each scan had to be of a patient over the age of 18. This is due to the analysis being based on a fully developed mandible. By the age of 18, mandibular growth becomes limited .
3. The patient had to have full permanent dentition. This is because mandibular resorption occurs in areas where teeth are absent (Wical and Swoope, 1974). Since the analysis is based on healthy mandibular structure, no mandibular resorption may be present amongst the data.
4. The patient had to have a Class 1 skeletal relationship, meaning that his/her upper (maxilla) and lower (mandible) jaw should be in harmony with each other. i.e. no under or overbite could have been present amongst the data.

3.2 Segmenting of skull surfaces

The software program 3D Slicer was used to create and eventually manipulate 3D rendered surfaces from the CT scans. 3D Slicer (Version 4.10, obtainable from <https://download.slicer.org/>) is a free open source software program that focuses on image analysis and visualisation. This made this program very suitable for creating virtual 3D surfaces from medical data. The patient scan data is essentially tomographic images of the region of interest viewed from all three planes, taken at 0.6 mm intervals. The image software combines these images to form a 3D virtual surface of this region. Figure 3.2 offers an illustration of a typical CT tomographic scan as observed from all three planes in 3D Slicer.



Figure 3.2: Snapshot of patient CT scan from all three planes
(Illustration: RL Gillingham)

The desired landmark positions occur on the skull. The software program has the function to isolate certain tissue groups by limiting the rendered volume to a certain density threshold. The higher this threshold is made, the denser the tissue matter that remains. This threshold was increased to such a point where only bony matter was visible.

3.3 Recording cephalometric measurements

Once the skull surfaces had been segmented and the anatomical landmarks were identified on each surface, the relevant measurements could be recorded. The locations of the landmarks are shown in Figures 2.7 and 2.8. Figure 3.3 illustrates the chosen coordinate system used when locating the landmarks and recording the measurements. The planes used for this coordinate system are described below:

Vertical plane (YZ): This plane is the same as the sagittal plane and divides the skull into two lateral halves.

Horizontal plane (XY): The horizontal plane is made parallel to the FH plane (shown in Figure 2.5), whilst passing through the nasion (N).

Frontal plane (XZ): The frontal plane passes through the nasion (N), whilst being perpendicular to both the YZ and XY planes.

The linear and angular measurements that were recorded for each skull surface are documented in Tables 3.1 and 3.2 respectively. 24 different measurements (13 linear and 11 angular) were recorded for each subject. Of these 24 measurements, 9 were bilateral (i.e. occurring on both sides), resulting in a total of 33 measurements.

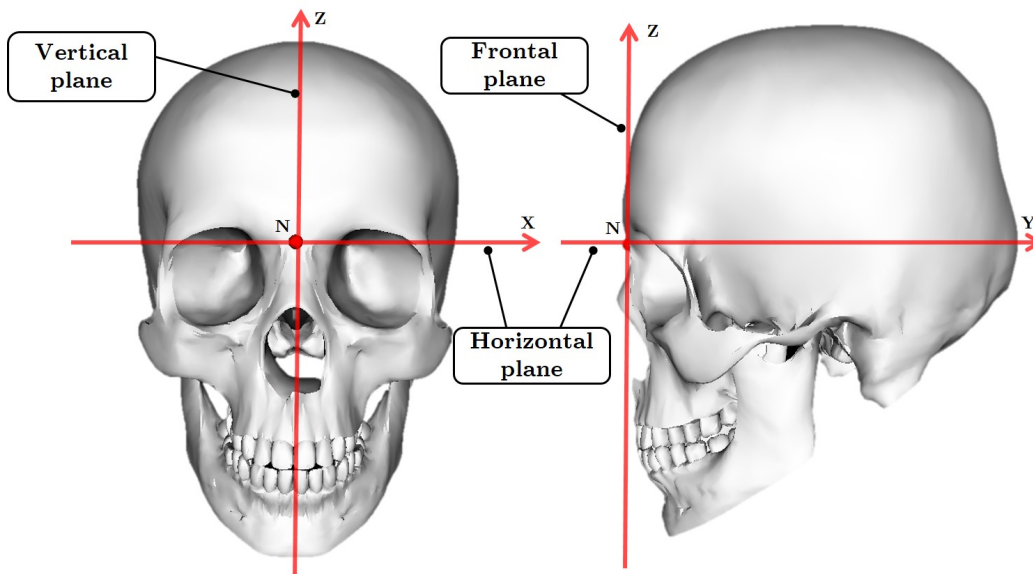


Figure 3.3: Coordinate system
(Illustration: RL Gillingham)

Table 3.1: Linear Measurements

Measurement	Description
Linear Measurements (mm)	
N-ANS	Distance between nasion and anterior nasal spine
FO-FO	Distance between right and left frontomalar orbitales
ZA-ZA	Distance between right and left zygomaxillare anteriores
Or-Or	Distance between right and left orbitales
Go-Sagittal	Distance between gonion and sagittal plane (bilateral)
Co-Sagittal	Distance between condylion and sagittal plane (bilateral)
N-Me	Vertical distance between nasion and menton
ANS-Me	Vertical distance between anterior nasal spine and menton
Co-Go	Distance between condylion on gonion (bilateral)
Co-Sig	Vertical distance between condylion and sigmoid notch (bilateral)
ID-Me	Distance between infradentale and menton
Go-Me	Distance between gonion and menton (bilateral)
Co-in - Co-out	Distance between the innermost and outermost point of the condyle (bilateral)

Table 3.2: Angular Measurements

Measurement	Description
Angular Measurements (°)	
SNA	Angle between the sella, nasion and A point
SNB	Angle between the sella, nasion and B point
ANB	Angle between the A point, nasion and B point
Facial Angle	Angle between the nasion, pogonion and FH plane
SN-Pg	Angle between the sella, nasion and pogonion
Me angle	Angle between the right and left gnathion and menton
Convexity angle	Angle between the nasion, A-point and pogonion
Me-Go-Co	Angle between the menton, gonion and condylion (bilateral)
Id-Me angle	Angle between the infradentale and menton
Co-Go-Fh	Angle between the condylion, gonion and FH plane (bilateral)
Sn-GoGn	Angle between the SN and GoGn planes (bilateral)

3.4 Statistical analysis

Once the measurements had been acquired from all the surfaces, a statistical analysis was performed on the results. This was to draw conclusions on gender differences, find the correlations that exist amongst the measurements and to test for the repeatability in obtaining the measurements. The statistical measures that were undertaken on the data are described in the following subsections.

3.4.1 Correlation

The SSM of the mandible to be formed by the end of this study relies on dense point correspondence. Forming this dense point correspondence is a challenging task (Clogenson *et al.*, 2015). Using the correlations between measurements of a cephalometric analysis, a more sparse and manageable approach is achieved in predicting certain unknown facial geometries. If strong correlations exist between certain facial measurements, then the known value of one or more measurements may be used to predict the unknown value of another by means of regression.

The Pearson correlation coefficient (r) is a measure of the linear correlation between two variables (Lee Rodgers and Nicewander, 1988). This coefficient may be used to show the degree of correlation between the cephalometric measurements. The value of this coefficient ranges between $-1 < r < 1$, where a value in the region of $0.65 < r < 1$ or $-1 < r < -0.65$ indicates a strong positive or negative correlation between the two variables respectively. This correlation coefficient is calculated as follows:

$$r = \frac{\sum_{i=1}^n (X_i - \mu_X)(Y_i - \mu_Y)}{\sqrt{\sum_{i=1}^n (X_i - \mu_X)^2 \sum_{i=1}^n (Y_i - \mu_Y)^2}} \quad (3.2)$$

r, X, Y and μ represent the correlation coefficient, the respective measurements and the mean value of the measurement respectively. Equation 3.2 can be simplified to:

$$r = \frac{cov(X, Y)}{\sigma_x \sigma_y} \quad (3.3)$$

The numerator is the covariance between the two measurements and the denominator is the product of the standard deviations of the two measurements. Rasmussen and Williams (2006) offers the following regression formula to calculate the value X when having the known value of Y :

$$X = \mu_X + \frac{cov(X, Y)}{\sigma_y^2} (Y - \mu_Y) \quad (3.4)$$

3.4.2 Statistical significance

This test serves to quantify the significance in the difference between two datasets. The p-value (p), which quantifies this difference, is the probability of obtaining the observed difference between the samples if the null hypothesis were true. The null hypothesis is the hypothesis that there is no difference between the two sets of data (Altman, 1990). This p-value came about by performing a two-sample t-test. This test compares the means and standard deviations of two datasets and returns a value (p-value) ranging between 0 and 1 (Snedecor and Cochran, 1989). A value $p < 0.05$ indicates that the two

datasets are significantly different, whilst any other value signifies that no significant difference is observed. For the current study, this test was used to assess:

1. The difference between the male and female South African population's skull structure.
2. The extent of the difference between overlapping measurements recorded by the current and other studies performed on subjects from different geographic locations.

3.4.3 Reliability of data

Before any assessment is used during clinical application, it is recommended to first establish the reliability of the data that's being recorded. Daly and Bourke (2008) defines this reliability as the extent to which measurements can be replicated. Reliability reflects both the correlation and agreement between values (Koo and Li, 2016). The intraclass correlation coefficient (ICC) is an index that successfully quantifies the degree of correlation and agreement between recorded measurements. This index is calculated using Equation 3.5, where σ_t and σ_e represent the standard deviation of the original measurements and the standard deviation of the error between the original and subsequent measurements respectively.

$$r_{ICC} = \frac{\sigma_t^2}{\sigma_t^2 + \sigma_e^2} \quad (3.5)$$

Depending on the application, various types of reliability exist. During the current study, the measurements were recorded by a single observer. The type of reliability that reflects the variation of data measured by a single rater across two or more trials is known as intra-rater reliability. The ICC coefficient ranges between 0 and 1, where a value closer to 1 indicates greater reliability. Cicchetti (1994) offers the following guidelines on interpreting the ICC rating:

- $0 < r_{ICC} < 0.4$: poor
- $0.4 < r_{ICC} < 0.6$: fair
- $0.6 < r_{ICC} < 0.75$: good
- $0.75 < r_{ICC} < 1$: excellent

3.5 Results/Findings

The following section offers the findings relating to gender dimorphism, correlations between measurements and comparisons to other ethnicities. The reliability of the study, as well as the updated sample size requirement was also reported.

3.5.1 Gender comparison

Table 3.3 shows the recorded angular measurements, where μ and σ represent the mean and standard deviation of these measurements respectively. A two-sample t-test was performed on the data to determine if the differences in the measurements performed on both genders differ significantly or not. From the results, it was shown that no significant difference was observed between the two genders for any of the angular measurements. When comparing linear measurements performed on the same subjects, as seen in Table 3.4, a large percentage of the measurements taken showed a significant difference between the two genders. Of the 19 recorded measurements, the two genders differed significantly in 17 measurements. The only measurements that didn't show a significant difference were the depths of the sigmoid notches (Co-Sig).

Table 3.3: Angular measurement comparison

Measurement [°]	Male (n=40)	Female (n=40)	p-value
	$\mu \pm \sigma$	$\mu \pm \sigma$	
SNA	85.15±3.50	83.46±4.40	0.06
SNB	81.72±4.11	80.04±4.70	0.09
ANB	3.83±2.22	4.02±2.54	0.72
Facial angle	87.24±2.40	86.92±2.15	0.53
SN-Pg	81.30±4.06	79.58±4.45	0.08
Me angle	62.22±5.34	62.54±5.21	0.79
Id-me angle	69.19±6.39	69.36±7.74	0.92
Convexity angle	8.19±4.95	8.41±5.65	0.85
Me-Go-Co (right)	115.41±3.88	115.42±4.60	0.99
Me-Go-Co (left)	115.87±4.20	115.42±5.22	0.67
Co-Go-Fh (right)	86.04±2.91	85.79±3.16	0.76
Co-Go-Fh (left)	85.55±3.13	85.45±3.68	0.90
Sn-GoGn (right)	32.21±5.00	34.43±6.02	0.08
Sn-GoGn (left)	31.12±4.95	33.32±5.94	0.08

*From two-sample t-test, * $p < 0.05$ (significant)*

*** $p < 0.001$ (very significant)*

Table 3.4: Linear measurement comparison

Measurement [mm]	Male	Female	p-value
	$\mu \pm \sigma$	$\mu \pm \sigma$	
N-ANS	49.54±2.81	46.41±3.23	< 0.001**
FO-FO	101.16±4.23	97.08±3.61	< 0.001**
ZA-ZA	94.70±5.51	89.89±4.97	< 0.001**
Or-Or	71.71±6.13	68.04±5.51	0.006*
Go-Sagittal (right)	46.65±3.14	44.46±2.65	0.001*
Go-Sagittal (left)	45.61±3.43	43.37±3.10	0.003*
Co-Sagittal (right)	50.72±2.87	47.08±3.14	< 0.001**
Co-Sagittal (left)	50.04±2.79	47.10±3.05	< 0.001**
N-Me	118.04±5.68	111.31±6.87	< 0.001**
ANS-Me	68.51±4.22	64.90±4.98	< 0.001**
Co-Go (right)	58.52±3.53	54.10±4.79	< 0.001**
Co-Go (left)	57.69±3.96	53.08±4.47	< 0.001**
Co-Sig (right)	18.61±2.82	18.15±3.09	0.49
Co-Sig (left)	18.21±3.09	17.84±3.13	0.60
ID-Me	34.08±3.06	31.75±3.56	0.002*
Go-Me (right)	89.20±4.88	84.83±4.67	< 0.001**
Go-Me (left)	89.44±5.77	84.93±4.73	< 0.001**
Co-in - Co-out (right)	19.47±1.92	17.78±2.07	< 0.001**
Co-in - Co-out (left)	19.21±1.97	17.81±2.15	0.003*

*From two-sample t-test, * $p < 0.05$ (significant)*

*** $p < 0.001$ (very significant)*

3.5.2 Correlations

Pearson's correlation coefficient (r) was calculated between the recorded measurements in order to establish the extent of the linear relationships that exist between them. For the purpose of this study, r values in the range of $-1 \leq r \leq -0.65$ and $0.65 \leq r \leq 1$ are documented. These correlations found between measurements performed on the male and female subjects are displayed in Table's 3.5 and 3.6 respectively.

Table 3.5: Strong correlations found between measurements performed on the male population

Male Population (n=40)		
Measurement 1	Measurement 2	r
N-ANS	N-Me	0.72
FO-FO	Or-Or	0.75
SNA	SNPg	0.71
	SNB	0.75
SNPg	SNB	0.98
ANB	Convexity angle	0.96
Me angle	Go-Sagittal (right)	0.77
Go-Sagittal (right)	Go-Sagittal (left)	0.78
N-Me	ANS-Me	0.88
	Id-Me	0.80
Co-Go (right)	Co-Go (left)	0.75
Co-Sig (right)	Co-Sig (left)	0.88
Me-Go-Co (right)	Me-Go-Co (left)	0.69
Facial angle	Go-Me (right)	0.71
	Go-Me (left)	0.72
Id-Me angle	Convexity angle	-0.67
Go-Me (right)	Go-Me (left)	0.90
Co-in - Co-out (right)	Co-in - Co-out (left)	0.85
Sn-GoGn (right)	Sn-GoGn (left)	0.94

From the results, it is clear that bilateral measurements (measurements that occur on both halves) share strong correlations with each other. Conversely, very few bilateral measurements showed strong correlations with measurements occurring on the mid-section of the mandible. Another deduction from the findings is that no measurements based purely on upper cranial or maxillary landmarks showed strong correlations with mandibular measurements. Using these correlations, the regression functions that form part of the SPM were formulated. These functions that regress the unknown value of a measurement by receiving the known value of other measurements as an input, can be seen in Appendix B.

Table 3.6: Strong correlations found between measurements performed on the female population

Female Population (n=40)		
Measurement 1	Measurement 2	r
N-ANS	N-Me	0.80
FO-FO	Or-Or	0.85
SNA	SNB	0.73
	SNB	0.98
SNPg	Sn-GoGn (right)	-0.73
	Sn-GoGn (left)	-0.78
ANB	Convexity angle	0.97
	Go-Sagittal (right)	0.77
Me angle	Go-Sagittal (left)	0.72
Go-Sagittal (right)	Go-Sagittal (left)	0.92
Co-Sagittal (right)	Co-Sagittal (left)	0.76
Co-Go-FH (right)	Co-Go-FH (left)	0.85
	ANS-Me	0.91
N-Me	Id-Me	0.84
Co-Go (right)	Co-Go (left)	0.84
Co-Sig (right)	Co-Sig (left)	0.92
Me-Go-Co (right)	Me-Go-Co (left)	0.69
Id-Me	Id-Me angle	-0.70
Id-Me angle	Convexity angle	-0.68
Go-Me (right)	Go-Me (left)	0.94
Sn-GoGn (right)	Sn-GoGn (left)	0.98

The strong correlations found between bilateral measurements were further supported by the results of a two sampled t-test. The results of this test, shown in Table 3.7, indicate that no significant difference exists between bilateral measurements for both the male and female subjects.

Table 3.7: Comparison of bilateral measurements

Measurement		Male		Female	
		r	p-value	r	p-value
Me-Go-Co	[°]	0.69	0.48	0.58	0.21
Co-Go-FH	[°]	0.57	0.45	0.85	0.82
SN-GoGn	[°]	0.94	0.35	0.98	0.78
Go-Sagittal	[mm]	0.78	0.07	0.92	0.25
Co-Sagittal	[mm]	0.64	0.40	0.76	0.80
Co-Go	[mm]	0.75	0.29	0.84	0.18
Co-Sig	[mm]	0.88	0.55	0.92	0.71
Go-Me	[mm]	0.90	0.79	0.94	0.95
Co-in - Co-out	[mm]	0.85	0.38	0.49	0.53

*From two-sample t-test, * $p < 0.05$ (significant)*

*** $p < 0.001$ (very significant)*

3.5.3 Comparison to other geographic areas

Table 3.8 shows the comparison between overlapping measurements performed by other studies on various ethnic groups for both the male and female populations. As can be seen by the comparisons, significant differences in the overlapping measurements can be found between the current study and other studies.

Table 3.8: Comparison of measurements performed on subjects from different geographic locations

Measurement [°]	Current Analysis		Bayome <i>et al.</i>		Baruah <i>et al.</i>		Miura <i>et al.</i>		Flynn <i>et al.</i>		Huang <i>et al.</i>	
	2018 (n=40)	South African	2013 (n=18)	Chinese	2009 (n=35)	Assam	1965 (n=40)	Japanese	1989 (n=15)	USA (black)	1998 (n=25)	USA (white)
SNA	85.15±3.50		81.92±2.78*		84.86±3.29		81±3.1**		-		83.14±3.92*	80.89±3.09**
SNB	81.72±4.11		80.43±2.63		81.31±3.64		76.2±3.1**		-		79.68±3.73*	78.14±2.51*
ANB	3.83±2.22		1.68±1.07**		3.37±1.29		4.9±1.7*		-		3.46±1.60	2.75±2.31
SN-GoGn	31.66±4.83		-		26.23±3.88**		36.4±4.3**		25.4±6.7**		-	-
Facial angle	87.22±2.48		90.01±2.21**		-		-		-		-	-
Convexity	8.19±4.95		2.48±2.03**		-		-		9.9±6.3		-	-
Me-Go-Co	115.63±3.72		113.77±3.26		-		-		120.4±8.9*		-	-
Male Population												
SNA	83.23±4.42		81.80±2.37		84.14±2.91		81.5±3.4		-		86.18±4.36*	80.60±2.85*
SNB	79.58±4.45		79.28±2.89		81.51±2.99*		77.2±3.0*		-		81.54±3.94	78.46±3.13
ANB	4.07±2.56		2.46±1.30*		2.65±1.47*		4.1±1.8		-		4.66±1.78	2.13±1.90*
SN-GoGn	33.96±5.99		-		26.97±5.82**		36.1±4.6		25.3±6.2**		-	-
Facial angle	86.99±2.12		90.76±2.39**		-		-		-		-	-
Convexity	8.49±5.71		3.46±1.61**		-		-		10.4±5.5		-	-
Me-Go-Co	115.43±4.76		117.02±3.92		-		-		119.1±5.4*		-	-
Female Population												

From two-sample *t*-test, * $p < 0.05$ (significant)

** $p < 0.001$ (very significant)

3.5.4 Reliability

The 33 measurements were recorded again for both male and female datasets, three weeks after the first set of measurements were obtained. This was in order to test for the intra-rater reliability of the measurements. The intra-class correlation coefficient (ICC), as described in Section 3.3.3, was calculated for each measurement to quantify their respective reliability. The male and female measurement's ICC ranged between $0.858 \leq r_{ICC} \leq 0.996$ and $0.863 \leq r_{ICC} \leq 0.997$ respectively. The three week break between the first and second measurement recordings, was to reduce the bias of memory when selecting the landmark positions. Following the standards described by Cicchetti (1994), these ICC ranges indicate excellent intra-rater reliability.

3.5.5 Recalculation of required sample size

The sample size calculation shown by Equation 3.1 was repeated using parameters obtained from the results. This was to determine if the current amount of samples used were sufficient. The effect size to shared standard deviation ratio ($\frac{\Delta}{\sigma}$) was calculated for each measurement for which a significant difference was observed between the male and female subjects. For conservativeness, the smallest ratio was used for the calculation as this would result in the largest sample size. The required number of samples was calculated to be 70, with 35 needed for each gender. As a result, no further samples were needed.

3.6 Discussion

The implications of the findings are discussed in the following subsections.

3.6.1 Gender comparison

No significant difference was found between any angular measurements performed on the male and female subjects. This suggests that the shape of the male and female skulls are relatively similar. Other studies, such as those performed by Miura *et al.* (1965), Huang *et al.* (1998) and Baruah *et al.* (2009) on the Japanese, USA and Assamese populations respectively, showed similar results, where angular measurements performed on both genders showed little significant difference. Conversely to the results of the angular measurement comparison, the two genders differed significantly for the majority of the recorded linear measurements (17 of 19). This shows that despite the skull structure of the male and female population being similar in shape, they differ significantly in size. These results are in agreement with other published cephalometric norms. Thilander *et al.* (2005) and Bayome *et al.* (2013), who conducted their studies on the Swedish and Korean populations respectively, reported that the linear measurements in male subjects were noticeably larger

than that in females. This was observed in the current study, where the average magnitude for every linear measurement, was greater for the male population. This clear difference in size leads to the conclusion that separate studies for both genders should be conducted when analysing cephalometric morphology.

3.6.2 Correlations

The strong linear correlations found between the recorded measurements are shown in Tables 3.5 and 3.6. For both genders, the majority of the bilateral measurements showed strong correlations with each other. It can therefore be assumed that bilateral measurements will have greater success in predicting missing bilateral measurements through regression than measurements occurring on the front section of the mandible. Another deduction from the findings is that no measurements based purely on upper facial or cranial landmarks showed a strong correlation with any mandibular measurements. This indicates that difficulties would arise if an estimation of mandibular geometry was attempted using the upper portion of a patient's skull. It would thus be preferable to use measurements local to the patient's mandibular defect when attempting to infer the shape of missing geometry.

3.6.3 Symmetrical nature

The use of the mirroring technique during VSR relies on the assumption that the mandible is symmetrical across the sagittal plane, i.e both halves of the mandible are similar. The findings shown in Table 3.7 indicate that no significant difference is present between any of the bilateral measurements (angular or linear) for both genders. This lack of significant difference between bilateral measurements as well as the strong linear correlations present between these measurements, supports the intuitive observation of the mandible being symmetrical across the sagittal plane.

3.6.4 Comparison to other geographic regions

Comparisons between overlapping measurements recorded in the current study and similar studies performed on subjects from different geographic areas (see Table 3.8), showed that significant differences in skull structure exist between the South African population and these other populations. Even studies on populations of the same racial type (black) to the subjects analysed for the current study, reported significantly different cephalometric norms. This shows that despite populations being of the same race, their anatomy could still be significantly different in shape and size. Baruah *et al.* (2009) reported similar findings where Indian groups from different locations differed significantly to each other. This emphasizes the need for a population-specific model for geometry prediction.

Chapter 4

Statistical Shape Model Construction

As seen in Chapter 2, the design of implants for patients with mandibular deformities is a very difficult and non-exact task, especially when mandibular symmetry cannot be used as a guide. The human error present in the design method presents a strong chance for the resulting implant not matching the patient's mandibular geometry accurately. Any kind of guideline for the shape of the resultant implant would be highly desired (Zachow *et al.*, 2005). The method of using a cephalometric analysis as described in Chapter 3, finds correlations that exist amongst a discrete amount of measurements that make up the human skull. This serves as a sparse representation of a shape that is complex in geometry. Statistical shape modelling offers a different approach in analysing the variation that exists in a particular shape family. A shape can be represented as a collection of points of any dimension (Cootes *et al.*, 2000). If a training set of shapes are aligned according to the same frame of reference and are then superimposed, a distribution of the points making up that particular shape can be observed. Statistical shape modelling involves the statistical analysis of this point distribution, where information on how the shapes within that particular shape family vary can be obtained. This analysis is usually carried out by performing Principal component analysis (PCA) on the point distribution. PCA finds the directions (principal components) in which the data varies. A model (SSM) of the shape in question is represented as a mean shape combined with these principal modes of variation.

Two gender-specific SSMs were constructed. Figure 4.1 illustrates the steps performed in order to construct the SSMs. The mandibular surfaces required for constructing the SSMs were obtained similarly to the way the skull surfaces were formed in Chapter 3. Once these surfaces had been segmented, they were aligned to a single reference shape, after which, correspondence

was found amongst the dataset. Once aligned, PCA was performed on the point distribution. The resultant PCA model is able to offer an estimate of healthy mandibular geometry by receiving partial input in the form of known mandibular coordinates.

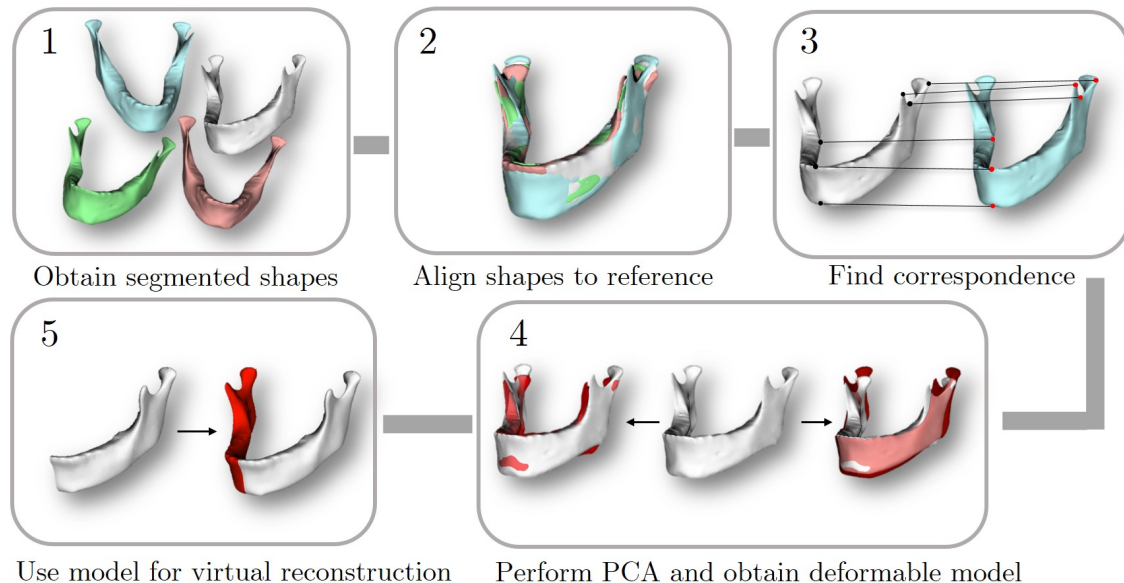


Figure 4.1: Steps in the SSM construction process
(Illustration: RL Gillingham)

4.1 Segmenting of mandibular surfaces

The resultant SSM of the mandible is created from mandibular surfaces. Segmenting mandibular surfaces is a more intricate process than when segmenting the skull surfaces in Chapter 3. When segmenting the skull surfaces, the density threshold of the particular region was increased to a point where the bony matter remained. In this case, only the mandibular surfaces of the subjects were desired. As a result, simply limiting the scene to a certain density threshold wouldn't isolate the mandible, as the mandible has a similar density to the surrounding unrelated bony matter. In order to isolate the rendering to only that of the mandible, the following steps were taken:

1. The density threshold function is used to isolate the anatomy in the CT scan scene to that of a threshold corresponding to the density of the mandible. Due to the mandible's similar bone density to surrounding matter, such as the teeth, this initial rendering contains many unwanted artefacts. Figure 4.3a displays this initial surface rendering.

2. To ensure that only a rendering of the mandible results, the unrelated matter was erased manually from each slice. Figure 4.2 illustrates the isolation of the mandible in the CT scan scene, whilst Figure 4.3b shows the surface rendering once the mandible has been isolated.
3. Remaining artefacts and noise were removed from the surfaces using the program's smoothing function. Figure 4.3c shows a mandibular surface after the smoothing process.

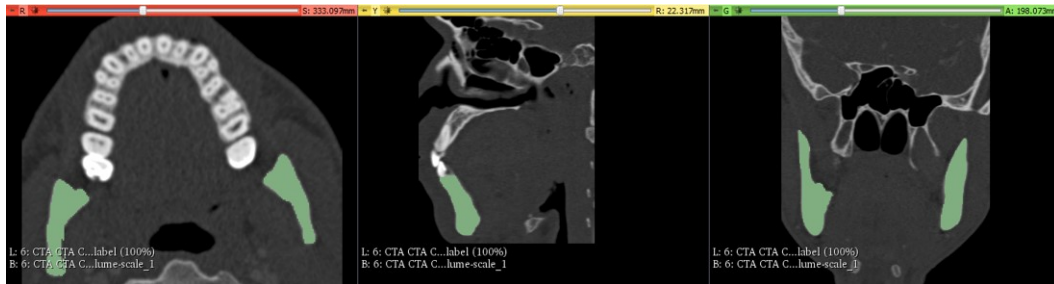


Figure 4.2: Snapshot of patient CT scan with mandible isolated
(Illustration: RL Gillingham)

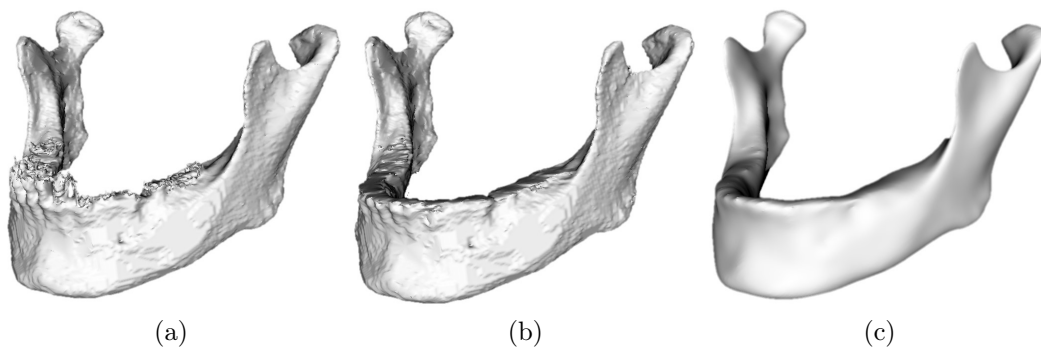


Figure 4.3: Segmentation process
(Illustration: RL Gillingham)

4.2 Shape alignment and developing correspondance

As mentioned earlier, every shape can be represented by a certain number of points that define its geometry. Before a point distribution of these shapes could be obtained, the shapes had to be aligned to the same orientation as a chosen reference shape. The most popular method to align the shapes of a given dataset is the Procrustes analysis (PA) (Heimann and Meinzer, 2009). This method initially involves defining a set of corresponding landmarks on

a reference shape, $D = \{d_i, \dots, d_n\}$, and the shape to be aligned to this reference, $M = \{m_i, \dots, m_n\}$. A transformation is found that maps the target shape to the reference shape. This transformation consists initially of translating the centroid of the target shape to the centroid of the reference shape (Clogenson *et al.*, 2015). Once this translation is achieved, the target shape undergoes a rotation until its alignment matches that of the reference shape. This transformation is defined by Equation 4.1 (Lorusso *et al.*, 1995).

$$\tau(m) = R(m_i + T) \quad (4.1)$$

T represents a translation vector that moves the centroid of M to the centroid D and R is a rotation matrix that rotates M to the same alignment of D after M has been translated. To obtain R , a correlation matrix, H , of the centred point sets is first calculated :

$$H = \sum_{i=1}^n (m_{c,i})(d_{c,i})^T \quad (4.2)$$

Using singular value decomposition (SVD), the correlation matrix is broken down as follows:

$$H = U\Lambda V^T \quad (4.3)$$

The rotation matrix (R) is calculated by means of Equation 4.4 (Lorusso *et al.*, 1995):

$$R = VU^T \quad (4.4)$$

Figure 4.4 illustrates this alignment of two shapes. When there is more than one shape that has to be aligned, the generalised Procrustes analysis is used. The steps detailing this method, as presented by Cootes *et al.* (2000), are as follows:

1. Choose one of the shapes as the reference shape, ς_R
2. Align the rest of the shapes, $(\varsigma_1, \dots, \varsigma_n)$, to the reference shape.
3. Once all the shapes have been aligned to the reference shape, compute the mean shape, ς_μ .
4. Use the calculated mean shape, ς_μ , as the new reference shape and repeat the procedure from step 2. If the new reference shape remains the same as the previous iteration, convergence can be assumed and the procedure is complete.

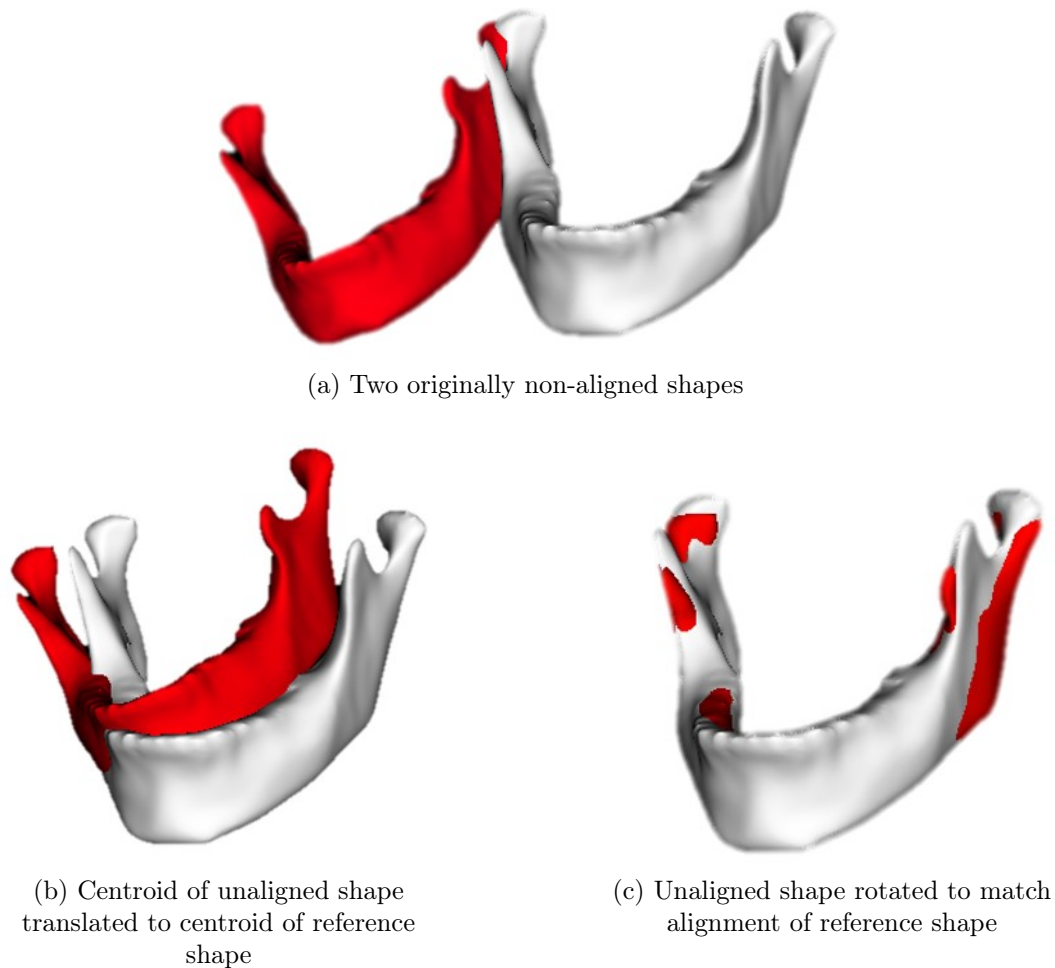


Figure 4.4: Alignment of shapes
(Illustration: RL Gillingham)

Once the shapes were aligned, correspondence was to be drawn amongst the shapes in the dataset. This means that for every point on one surface, the corresponding point had to be found on the other surface (Albrecht, 2011). This correspondence finding procedure is often termed as registration. Registration is accomplished by finding some mapping or deformation that maps the reference shape onto the target shape. This problem can be defined by Equation 4.5 and visualised in Figure 4.5 (Clogenson *et al.*, 2015):

$$T(x) = \Omega_r \rightarrow \Omega_t \quad (4.5)$$

There are two types of transformations in order to find this mapping, namely: rigid-body and nonrigid transformations (Audette *et al.*, 2000). One of the most commonly used rigid-body transformations to find correspondence is the Iterative closest point (ICP) method developed by Besl and McKay (1992)

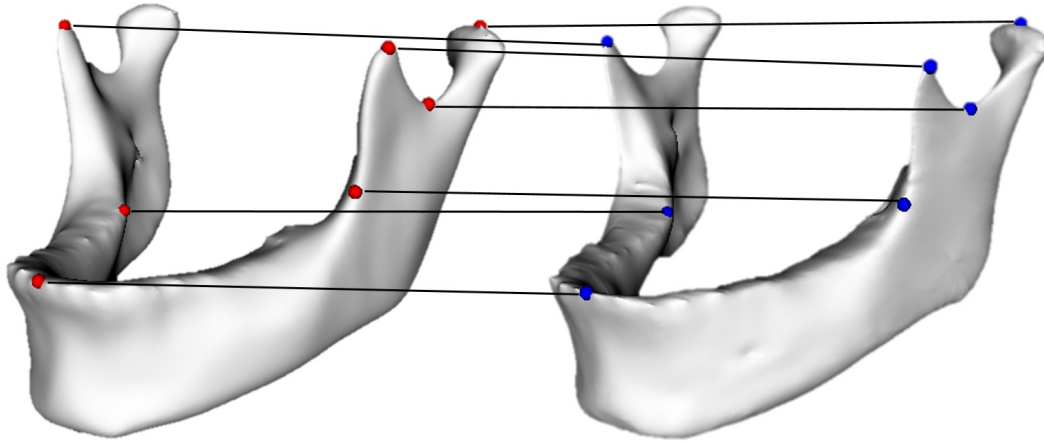


Figure 4.5: Illustration of matching point pairs
(Illustration: RL Gillingham)

(Heimann and Meinzer, 2009). This method assumes that the pose of the two shapes has not yet been accounted for and that every point on the reference shape corresponds to the closest point on the target shape. A transformation that reduces the root mean square (RMS) distance between the matched point pairs is implemented on the target shape. The sum of the squared distances between matched point pairs is used as the similarity metric. This process is repeated until the similarity metric shows a negligible change. This method is similar to the Procrustes analysis described earlier, except for the fact that the Procrustes analysis requires corresponding point sets as an input, whereas the ICP method treats this correspondence as a variable to be estimated. This method of correspondence should be limited to situations where a good size initialisation has already been achieved between the reference and target shapes. If the target and reference shapes differ considerably in size, then the ICP method will most likely draw incorrect correspondences (Heimann and Meinzer, 2009). It's for this reason that rigid-body transformations are best suited to applications where the same shape has been imaged by different modalities, and deformations to this shape are negligible. Seeing as for this study's application, correspondence is to be found amongst a dataset consisting of similar shapes, but not the same shape, a nonrigid transformation would be better suited to find this correspondence.

A general form of this nonrigid approach would be to find a global polynomial function that maps the reference shape to the target shape (Lavalley, 1996). This process of mapping is referred to as global polynomial interpolation. Such functions are known to not always produce suitable local deformations on anatomical structures (such as bones). Unpredictable behaviour can also result in the deformation finding process when the degree of the polynomial function is too high (Audette *et al.*, 2000). This can be mitigated some-

what by replacing the global polynomial function with a piecewise polynomial function. An example of such a piecewise polynomial function is a spline. Splines are known to show a very high degree of smoothness/continuity at the points (knots) where the piecewise polynomials connect (Judd and Judd, 1998). In interpolation/approximation applications, the use of splines are often preferred to global polynomial functions as the results yielded are similar, whilst the problem of instability is avoided. Subsol *et al.* (1998) and Fleute *et al.* (1999), who were amongst the first to use nonrigid deformation methods to find correspondence amongst the training shapes, both made use of spline approximation, specifically B-spline and Octree spline approximation respectively (Heimann and Meinzer, 2009).

Similar to the spline-based approaches, where complex deformations can be expressed through a combination of piecewise functions, Lüthi *et al.* (2017) describes a method where a deformation can be sampled from a Gaussian process as a linear combination of basis functions. A Gaussian process is a collection of random variables, any finite number of which have a joint Gaussian (normal) distribution (Wilson and Adams, 2013). There is no limit to the number of entries in this random collection of variables. As such, a Gaussian process can be generalised as a distribution over functions, rather than simply a finite amount of variables. In the case of finding correspondence between shapes, the functions are represented by the deformations that are added to the reference shape in order to match the target shape. A deformation sampled from a Gaussian process may be generalised as a mean deformation combined with a covariance function (Wilson and Adams 2013; Lüthi *et al.* 2017).

$$u(x) \sim GP(\mu(x), k(x, x')) \quad (4.6)$$

$k(x, x')$ represents a covariance/kernel function that determines the measure of similarity between two points. It is this kernel function that ultimately determines the smoothness of the deformations. With this method, smooth and predictable deformations are sampled and added to the reference shape, allowing it to deform in a manner that preserves its topology. Another recently devised registration technique that deforms the reference point set in a smooth manner that preserves its topology, is the Coherent point drift (CPD) algorithm developed by Myronenko and Song (2010). With this method, the reference point set is represented as Gaussian mixture model (GMM) centroids. These centroids are fitted to the target points by maximising the likelihood of correspondence using the Expectation maximum (EM) algorithm, initially described by Dempster *et al.* (1977).

For this step of the SSM construction, the Gaussian process morphable model (GPMM) registration technique described by Lüthi *et al.* (2017) was used. This was due to this method's ability to produce smooth deformations to the reference shape, allowing its topology to be preserved. An added benefit

of this method is its flexibility, where prior knowledge of the shape in question can be utilised to restrict the deformations under various conditions (Clogenson *et al.*, 2015). The open source software programs Statismo and Scalsimo easily allow for the implementation of this registration technique (Lüthi *et al.*, 2012). The rest of this section serves to summarise the use of this method in adding a deformation to the reference shape so that it matches the target shape.

This reference shape combined with a deformation sampled from the Gaussian process results in a new shape instance. This Gaussian process, by performing a Karhunen-Loève expansion, is represented parametrically as the summation of an infinite set of basis functions, as shown in Equation 4.7 (Lüthi *et al.*, 2017):

$$u(x) = \mu(x) + \sum_{i=1}^{\infty} b_i \sqrt{\lambda_i} \phi_i(x), b_i \in N(0, 1) \quad (4.7)$$

λ_i and ϕ_i represent eigenvalue/eigenfunction pairs that are calculated via Equation 4.8 and b_i is a constant that follows a normal distribution. (Rasmussen and Williams, 2006).

$$\lambda_i \phi_i(x') = \int k(x, x') \phi_i(x) d\rho(x) \quad (4.8)$$

Due to there being an infinite amount of basis functions that make up the Gaussian process, computing the integral in Equation 4.8 is infeasible unless a lower-rank approximation is obtained. This low-rank approximation is obtained by letting $d\rho(x) = p(x)dx$, where $p(x)$ is a probability density function (PDF). This leads to Equation 4.9, where x_l is sampled from $p(x)$.

$$\lambda_i \phi_i(x') = \int k(x, x') \phi_i(x) p(x) dx \sim \frac{1}{n} \sum_{l=1}^n k(x_l, x') \phi_i(x_l) \quad (4.9)$$

Substituting $(x_l)_{l=1 \rightarrow n}$ for x' in Equation 4.9 results in the eigenvalue problem defined by Equation 4.10.

$$K u_i = \lambda_i^{est} u_i \quad (4.10)$$

K represents a $n \times n$ covariance matrix of the sampled points, λ_i^{est} the i^{th} eigenvalue and u_i , the corresponding eigenvector. λ_i^{est} and u_i are calculated by performing SVD on the covariance matrix, where λ_i^{est} serves as an estimate for λ_i , whilst $\phi_i(x)$ is estimated via Equation 4.11:

$$\phi_i^{est}(x) = \frac{\sqrt{n}}{\lambda_i^{est}} k_X(x) u_i \quad (4.11)$$

Note that $k_X(x) = (k(x_1, x), \dots, (k(x_n), x))$. $\phi_i^{est}(x)$ serves as an estimation for the i^{th} eigenfunction of the Gaussian process and extends to all points within

the domain. This is contrary to u_i that extends only to the sampled points. If an infinite amount of points were sampled, u_i and λ_i^{est} would be equal to λ_i and $\phi_i(x)$ respectively. Therefore, the more points sampled from $p(x)$, the more accurately these quantities are estimated (Lüthi *et al.*, 2017). With λ_i^{est} and $\phi_i^{est}(x)$, Equation 4.7 is approximated by Equation 4.12:

$$u^{est}(x) = \mu(x) + \sum_{i=1}^n b_i \sqrt{\lambda_i^{est}} \phi_i^{est}(x), b_i \in N(0, 1) \quad (4.12)$$

With this low-rank approximation, a deformation is sampled from the Gaussian process and added to the reference shape. To find correspondence with a target shape, the reference shape must undergo a deformation until the deformed shape matches that of the target shape. This model fitting problem is shown by Equation 4.13 and is illustrated in Figure 4.6.

$$S_d = S_r + u^{est}(x), S_d \sim S_t \quad (4.13)$$

S_d represents the deformed reference shape (S_r) that matches the target shape (S_t). This model fitting problem may be solved by optimising the values of the weighting factors, $b_{i \rightarrow n}$ so as to minimise the error between the reference and target shapes, or by obtaining a posterior estimate, as described in Section 4.4. S_d serves as a representation of S_t that is in correspondence with S_r (Clogenson *et al.*, 2015).

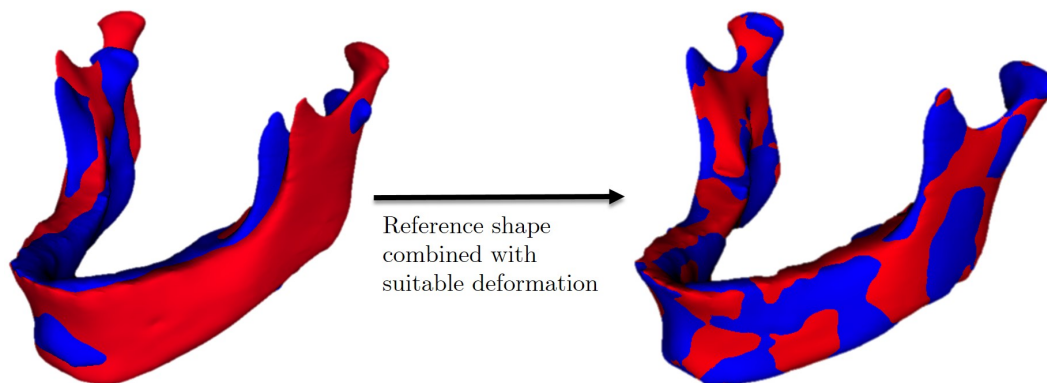


Figure 4.6: Deformation of reference shape (red) to match target shape (blue)
(Illustration: RL Gillingham)

4.3 Principal component analysis

Once all the instances within the dataset were aligned and superimposed, the variation at each of the points making up the general shape could be seen. This point distribution was then statistically analysed and represented as a mean shape combined with modes of variation. Figure 4.7 illustrates a typical

point distribution model of a dataset consisting of 17 aligned shape instances of the mandible's left side. Cootes and Taylor (1995) were amongst the first to statistically analyse the point distribution of a shape family and develop modes of variation from the training data. These modes were calculated using principal component analysis (PCA).

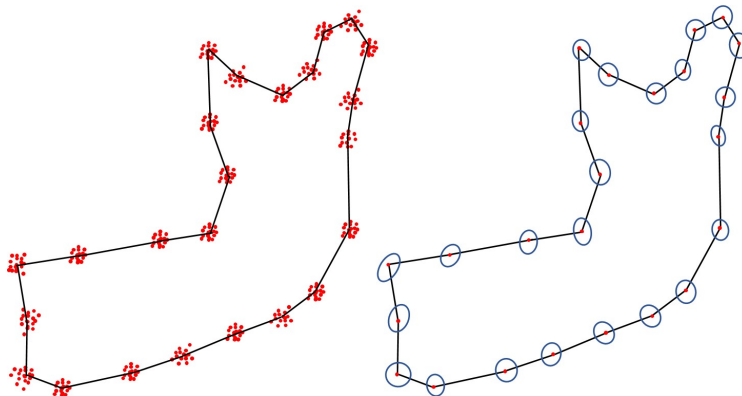


Figure 4.7: Example of a point distribution model
(Illustration: RL Gillingham)

The basis of a PCA-based SSM relies on the assumption that the total variation that exists amongst a shape family may be learned from example shapes (Lüthi *et al.*, 2017). PCA makes use of an orthogonal transformation in order to convert a set of possibly correlated variables into a set of linearly uncorrelated variables called principal components. These principal components, which are achieved by performing Singular-value decomposition (SVD) on the data's covariance matrix, are arranged in descending order of explained variance. Each of these principal components or modes of variation represent the "directions" in which the data (in our case shapes) changes. These directions are tough to visualise in applications where the dimension of the data is high. Figure 4.8 offers a more intuitive view of these principal components, where the dimensionality of the data points is only two. Therefore, in the case of shape modelling, any shape within the variation limits described by the training data can be realised by combining these components to the mean shape under various weightings.

This PCA-based model is generalised by Equation 4.14, where s , μ , b and ϕ represent a shape instance, the mean shape, a certain weighting and a principal component respectively. The rest of this section serves to detail the steps performed in order to obtain a PCA-based SSM in the form of Equation 4.14.

$$s = \mu + \sum_{i=1}^n b_i \phi_i \quad (4.14)$$

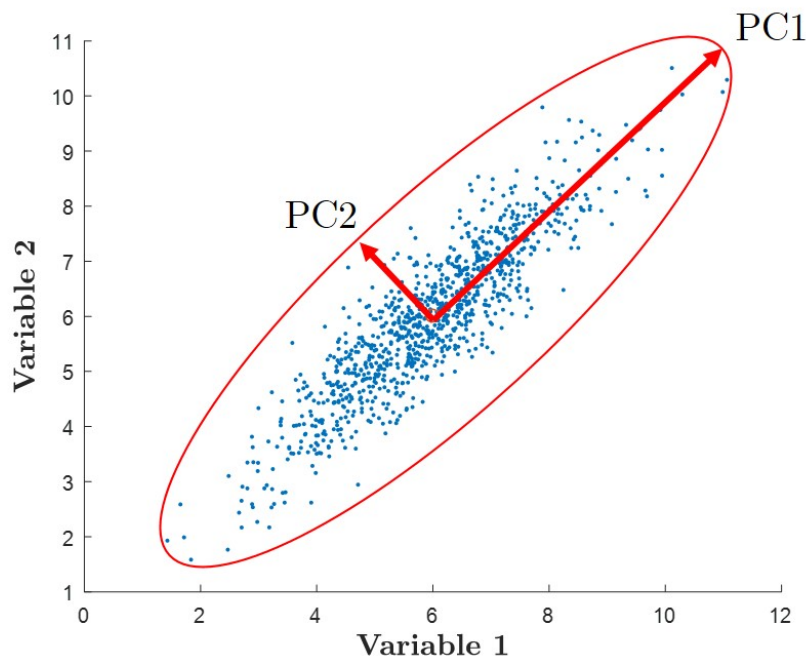


Figure 4.8: Basic example of PCA
(Illustration: RL Gillingham)

Each shape within the example data is represented as a vector $s_i \in \mathfrak{R}^{3n}$, where the x, y and z components of each point making up the shape, form the contents of the vector (Nair and Cavallaro, 2009):

$$s_i = (x_{1x}, x_{1y}, x_{1z}, \dots, x_{nx}, x_{ny}, x_{nz})^T \quad (4.15)$$

The general assumption that the shape variations can be modelled as a normal distribution is made, where μ and Σ represent the mean shape and covariance matrix of the data respectively (Lüthi *et al.*, 2017):

$$s \sim N(\mu, \Sigma) \quad (4.16)$$

The mean shape vector μ and covariance matrix Σ are calculated as follows (Shlens, 2014) :

$$\mu = \frac{1}{n} \sum_{i=1}^n s_i \quad (4.17)$$

$$\Sigma = \frac{1}{n-1} \sum_{i=1}^n (s_i - \mu)(s_i - \mu)^T \quad (4.18)$$

The resultant covariance matrix has dimensions of $n \times n$, with n being the number of entries in the original shape vector s_i . The element in the (i, j) position of the matrix is the covariance between the i^{th} and j^{th} elements of the shape vector s_i . This covariance is the measure of the linear relationship

between the two variables. For example, if the larger values of one variable correspond with the larger values of the other variable, and the same holds for the lesser values, then the covariance between the two variables is positive. If a relationship opposite to the one just mentioned occurs, then the covariance between the variables will be negative (Rasmussen and Williams, 2006).

An expansion of Equation (4.16) with vector and matrix representations of μ and Σ respectively is shown in Equation (4.19):

$$s \sim N \left(\underbrace{\begin{pmatrix} \mu_{x_{1x}} \\ \mu_{x_{1y}} \\ \mu_{x_{1z}} \\ \vdots \\ \mu_{x_{nx}} \\ \mu_{x_{ny}} \\ \mu_{x_{nz}} \end{pmatrix}}_{\mu}, \underbrace{\begin{pmatrix} \sum x_{1x}x_{1x} & \sum x_{1x}x_{1y} & \sum x_{1x}x_{1z} & \cdots & \sum x_{1x}x_{nz} \\ \sum x_{1y}x_{1x} & \sum x_{1y}x_{1y} & \sum x_{1y}x_{1z} & \cdots & \sum x_{1y}x_{nz} \\ \sum x_{1z}x_{1x} & \sum x_{1z}x_{1y} & \sum x_{1z}x_{1z} & \cdots & \sum x_{1z}x_{nz} \\ \vdots & \vdots & \vdots & \ddots & \vdots \\ \sum x_{nz}x_{1x} & \sum x_{nz}x_{1y} & \sum x_{nz}x_{1z} & \cdots & \sum x_{nz}x_{nz} \end{pmatrix}}_{\Sigma} \right) \quad (4.19)$$

The next step in producing the PCA based shape model is determining the principal modes of variation or "directions" in which the data changes with each other (Cootes *et al.*, 2000). This is accomplished by executing eigenvalue decomposition on the covariance matrix, as seen in Equation (4.20):

$$\Sigma = \begin{pmatrix} \vdots & \vdots & \vdots \\ \phi_1 & \cdots & \phi_n \\ \vdots & \vdots & \vdots \end{pmatrix} \begin{pmatrix} \lambda_1 & \cdots & 0 \\ \vdots & \ddots & \vdots \\ 0 & \cdots & \lambda_n \end{pmatrix} \begin{pmatrix} \vdots & \vdots & \vdots \\ \phi_1 & \cdots & \phi_n \\ \vdots & \vdots & \vdots \end{pmatrix}^T \quad (4.20)$$

ϕ_i and λ represent the principal modes/directions of variation (eigenvectors) and the variance (eigenvalues) that occurs at these modes respectively, centred at the mean of the data (Cootes *et al.*, 2000). The standard deviation (σ_i) of the data along the direction of the respective principal modes (ϕ_i) is calculated by taking the square root of the variance λ_i :

$$\sigma_i = \sqrt{\lambda_i} \quad (4.21)$$

According to the generalised normal distribution, $\sim 99.7\%$ of the data in line with any mode of variation can be realised within the confines of 3 standard deviations either side of the mean. As a result, PCA leads to a probabilistic model where any valid shape can be approximated by the linear combination of the modes to the data's mean shape (Heimann and Meinzer, 2009):

$$s = \mu + \sum_{i=1}^n b_i \sigma_i \phi_i \quad (4.22)$$

where b_i represents any value within the confines of $\{-3, 3\}$.

4.4 Shape estimation

Once the PCA shape model had been constructed, it could be used as a tool to estimate missing geometry of any shape within the shape family. This is accomplished by converting the prior model into what is known as a posterior shape model using partial input in the form of known point positions (Lüthi *et al.*, 2017). The new posterior model has the same characteristics as the prior shape model, $s_P \sim N(\mu_P, \Sigma_P)$, with the new mean (μ_P) serving as an estimate for the most likely geometry of the shape needing to be reconstructed based on the partial input received. The total variance in point positions observed in the covariance matrix (Σ_P) is also reduced as a result of having fixed point positions fed into the shape model. This posterior shape model is often referred to as a conditional shape model. The first part of producing a posterior model is identifying the known landmark positions on the shape to be reconstructed $L = \{L_1, \dots, L_n\}$ as well as the corresponding positions on the mean shape of the prior model $y = \{y_1, \dots, y_n\}$ (Lüthi *et al.*, 2017). From these positions, the discrepancies between the observed landmark positions and their corresponding positions on the prior model are calculated:

$$U = \begin{pmatrix} \Delta_1 \\ \vdots \\ \Delta_n \end{pmatrix} = \begin{pmatrix} L_1 - y_1 \\ \vdots \\ L_n - y_n \end{pmatrix} \quad (4.23)$$

The formulae for the new posterior model mean (μ_P) and covariance matrix (Σ_P) are as follows (Rasmussen and Williams, 2006):

$$\mu_p = \mu + \Sigma_{xy}^T \Sigma_{yy}^{-1} U \quad (4.24)$$

$$\Sigma_P = \Sigma - \Sigma_{xy}^T \Sigma_{yy}^{-1} \Sigma_{yx} \quad (4.25)$$

where Σ_{yy} represents the covariances between the observed landmark positions on the prior model and Σ_{yx} are the covariances between the observed and non-observed positions. Σ represents the prior model's covariance matrix. Figure 4.9 illustrates this model fitting process, with the original and posterior SSMs seen as point clouds. Figure 4.9a shows the identification of certain landmark positions on both the SSM mean (green) and target shape (blue). These observed landmarks serve as partial input to calculate the posterior SSM mean, shown in Figure 4.9b. Notice how the point cloud that represents the posterior SSM mean closely resembles that of the target shape. An even better fit is achieved if more landmarks corresponding on both the SSM and target shape are chosen.

The ICP method described earlier, is a useful technique to obtain this dense set of corresponding points. This method of correspondence should be limited to when a good size initialisation has already been achieved between

the reference and target shapes. It is therefore recommended to first obtain a posterior shape estimate of the target shape from sparse and manual landmark selection as partial input to the SSM.

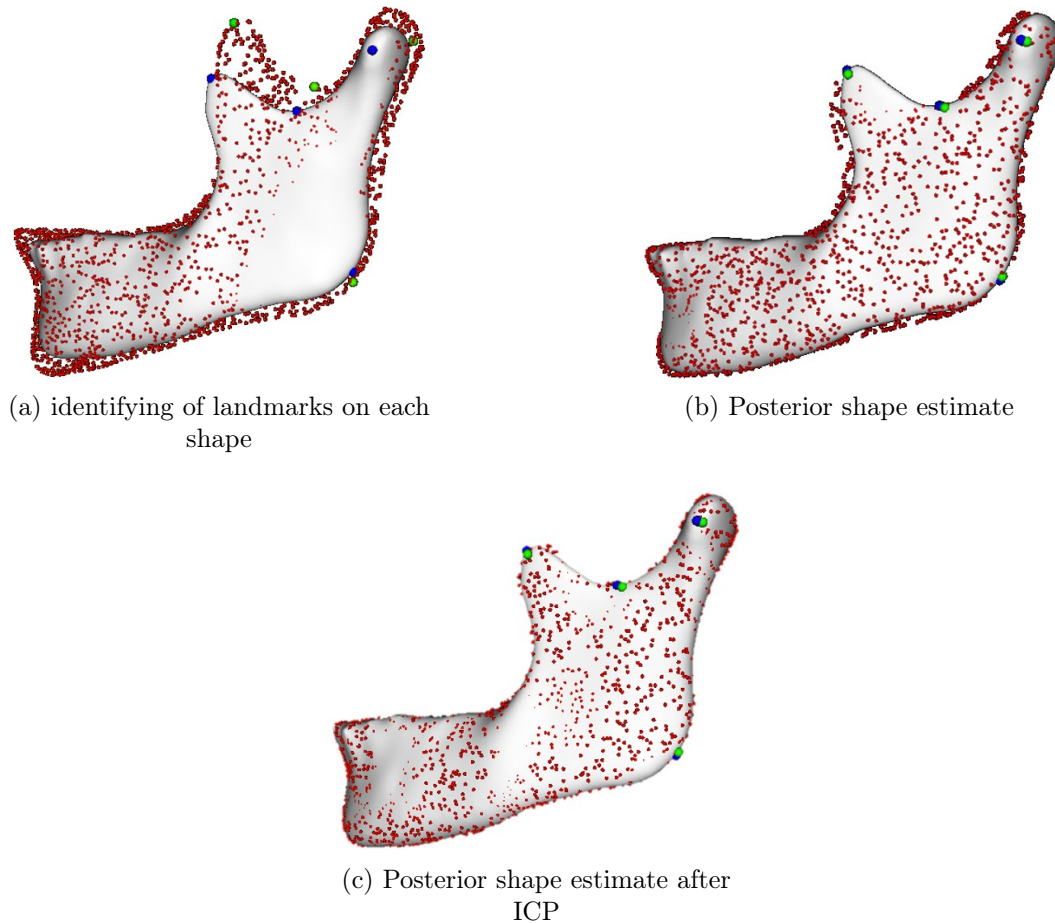


Figure 4.9: Model fitting procedure
(Illustration: RL Gillingham)

The posterior estimate then serves as the reference shape, on which a dense set of random points is generated and serve as pseudo-landmarks. The corresponding point on the target shape for each of the randomly generated points on the reference shape is assumed to be the point closest in distance. The distance discrepancies between these pseudo-landmarks and the corresponding closest points on the target shape serve as the new U , as seen in Equation 4.23. From here, a new posterior mean and covariance matrix is calculated using this dense set of distance discrepancies. This process is iterated a pre-determined amount of times or until negligible differences occur between estimates of consecutive iterations. An illustration of the new posterior estimate of the target shape may be seen in Figure 4.9c. Note how this estimate resembles the target

shape closer than the posterior estimate in 4.9b, when only a few landmarks were selected as partial input.

4.5 Model validation

Before using the SSM for reconstruction purposes, the quality of the SSM was evaluated. Davies (2002) and Styner *et al.* (2003) describe three objective evaluation measures, namely: the compactness, specificity and generality of the model. The model's performance in these measures was compared to other models in literature, where a decision was made on whether the current model's quality is of a suitable standard or not. These evaluation measures that were performed on the models are described below:

1. Compactness: A compact model is one where few parameters are needed to explain the variation limits that describe that model. The compactness of the SSM is calculated as the cumulative variance of the model as a function of the number of parameters, in this case, modes (Styner *et al.* 2003; Clogenson *et al.* 2015). In many cases, the amount of modes used in the specific model are reduced to a number that describes a suitable amount of the population's variance, usually 90 to 100% (Heimann and Meinzer, 2009). This is especially useful when a model is constructed from a large dataset, where reducing the dimensionality of the model could reduce noise and improve computational efficiency. This is shown by Equation 4.26, where $C(M)$, M and λ_i , represent the cumulative variance, number of modes and the i_{th} eigenvalue respectively.

$$C(M) = \sum_{i=1}^M \lambda_i \quad (4.26)$$

The fewer modes needed for the desired amount of variance to be explained, the more compact the model is.

2. Generality: The generalization ability of a model refers to the model's ability to represent unseen data of the same class that the model is made from. This is done by means of performing a leave-one-out experiment (Styner *et al.* 2003; Clogenson *et al.* 2015). This involves formulating the SSM with all but one of the mandibular surfaces from the training set and testing the SSM's ability to represent the left out surface. This test is repeated for all the surfaces that form part of the training set. The generalization ability is calculated as the root mean square error (RMSE) between the SSM estimation and the unseen surface as a function of the model's number of modes. This is shown by Equation 4.27, where $G(M)$, S_i , t_i and n_g represent the generalization ability of the model, the model's

estimate of the i_{th} unseen surface, the i_{th} unseen surface and the number of members in the training set respectively.

$$G(M) = \frac{1}{n_g} \sum_{i=1}^{n_g} RMSE(S_i(M), t_i) \quad (4.27)$$

The RMSE, which is a frequently used measure of the differences between predicted and observed values, is calculated via Equation 4.28

$$RMSE = \sqrt{\frac{1}{n} \sum_{i=1}^n (P_i - O_i)^2} \quad (4.28)$$

where P , O and n represent the predicted, observed and the number of points respectively (Hyndman and Koehler, 2006).

3. Specificity: Specificity measures the model's ability to generate instances that are similar to those of the training set. This is achieved by generating a random instance from the SSM and finding the member of the training set where the RMSE is the lowest between to two shapes. This process is repeated a predetermined amount of times, where the RMSE is recorded for each iteration. The specificity is defined as the average of the recorded RMSE's as a function of the model's modes. This can be seen in Equation 4.29, where $S(M)$, R_i , t_i and n_s represent the specificity, i_{th} random SSM instance, the member of the training set that resembles this instance the closest and the number of iterations respectively.

$$S(M) = \frac{1}{n_s} \sum_{i=1}^{n_s} RMSE(R_i(M), t_i) \quad (4.29)$$

4.6 SSM validation results

Two gender-specific SSMs were constructed, each made using 40 mandibular surfaces. As discussed in Section 4.5, the three objective measures of model quality: compactness, specificity and generality were performed on the models in order to decipher whether they are of a suitable standard or not. The rest of this section offers the results of the evaluation tests performed on the SSMs.

4.6.1 Compactness

As mentioned in Section 4.5, the fewer parameters needed to describe a model's variance, the more compact the model is. Figure 4.10 shows the compactness of the SSMs as a function of the number of modes used. 12 and 11 Modes were needed to capture 90% of the data's variance for the male and female SSMs

respectively. Abdolali *et al.* (2017) who constructed a gender-mixed SSM of the mandible from 84 subjects, reported approximately 90% of the cumulative variance of the dataset being explained by 15 modes. Tables 4.1 and 4.2 show the amount of variance captured by the first three modes as well as a visual implication of altering the shape parameters of these modes (between -3σ and $+3\sigma$) for the male and female SSMs respectively.

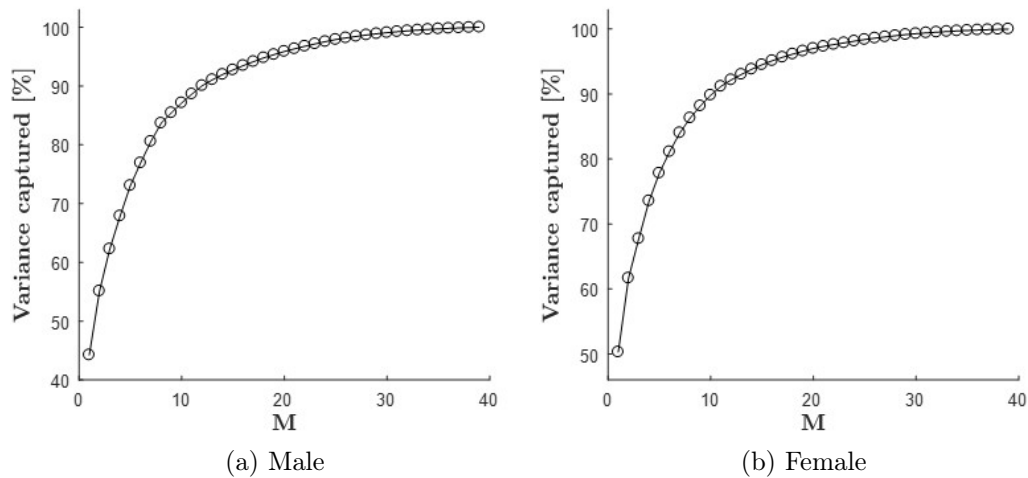











Figure 4.10: Compactness
(Illustration: RL Gillingham)

Table 4.1: Variance captured by first three modes for male SSM

M	-3σ	mean	$+3\sigma$	%
1				44
2				11
3				7

mean shape shown in white, altered shape shown in red

Table 4.2: Variance captured by first three modes for female SSM

M	-3σ	mean	$+3\sigma$	%
1				50
2				11
3				6

mean shape shown in white, altered shape shown in red

4.6.2 Specificity

A model should only generate shape instances that are similar to those shapes part of the training set. The lower the specificity values the better. The test for specificity was performed 100 times where the specificity score and standard error, as a function of the model's number of modes, are shown seen in Figure 4.11. The specificity ranged from 0.6 to 1.13 mm and 0.63 to 1.16 mm for the male and female models respectively.

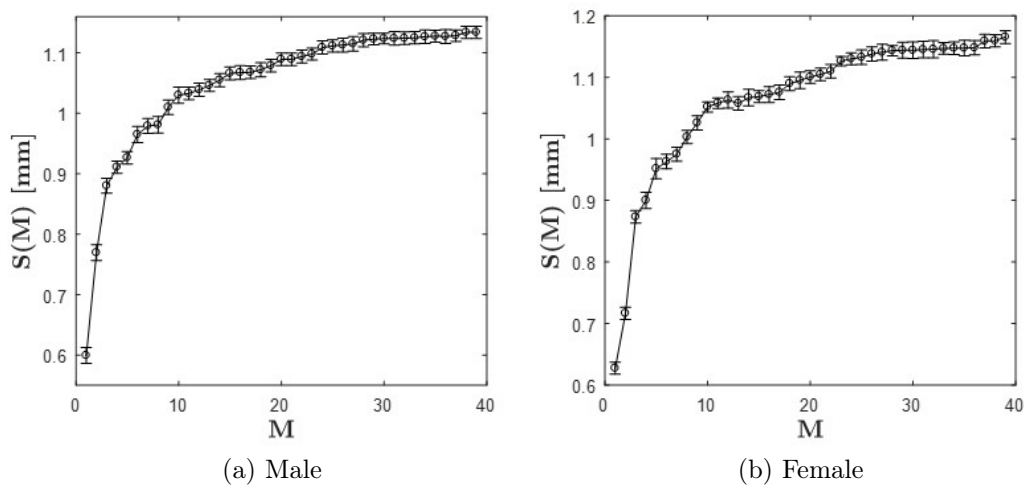


Figure 4.11: Specificity
(Illustration: RL Gillingham)

The previously mentioned gender mixed model developed by Abdolali *et al.* (2017) achieved a specificity ranging between 1.38 and 1.39 mm. Similar to the current study, Abdolali *et al.* (2017) made use of a nonrigid free-form deformation model to draw correspondence amongst the training shapes. The similarity measure between the reference and target shapes in that study was optimised using the gradient descent algorithm. Specificity performance results from other studies on SSMs of various anatomical structures are shown in Table 4.3.

Table 4.3: Specificity ranges of SSMs on various anatomical structures

Structure	Current study		Abdolali <i>et al.</i> (2017)	Van der Merwe (2018)		Clogenson <i>et al.</i> (2015)	Mayya <i>et al.</i> (2015)
	Mandible	Mandible	Mandible	Femur	Femur	Vertebra (C2)	Scapula
Gender	Male (n=40)	Female (n=40)	Neutral (n=84)	Male (n=32)	Female (n=32)	Neutral (n=92)	Neutral (n=85)
Specificity range (mm)	0.6 to 1.13	0.63 to 1.16	1.38 to 1.39	0.92 to 1.75	0.71 to 1.38	0.63 to 0.84	1.37 to 1.77

All of the studies shown in Table 4.3 made use of nonrigid registration methods in order to achieve correspondence amongst the training data.

4.6.3 Generality

A generality test was performed on the SSMs to assess their ability to represent unseen data. This was done by performing a leave-one-out experiment, as described in Section 4.5. As with specificity, the lower the generality values, the better. The generalization ability of the two models as a function of the number of modes used, is shown in Figure 4.12. The generalization ability ranged from 0.64 to 1.08 mm and 0.66 to 1.16 mm for the male and female models respectively. Abdolali *et al.* (2017)'s model of the mandible achieved similar generality values ranging between 0.6 and 1.3 mm. The generalization abilities of models produced by other studies are shown in Table 4.4.

Table 4.4: Generality ranges of SSMs on various anatomical structures

Structure	Current study		Abdolali <i>et al.</i> (2017)	Van der Merwe (2018)		Clogenson <i>et al.</i> (2015)	Mayya <i>et al.</i> (2015)
	Mandible	Mandible	Mandible	Femur	Femur	Vertebra (C2)	Scapula
Gender	Male (n=40)	Female (n=40)	Neutral (n=84)	Male (n=32)	Female (n=32)	Neutral (n=92)	Neutral (n=85)
Generality range (mm)	0.64 to 1.08	0.66 to 1.16	0.6 to 1.3	0.67 to 1.09	0.55 to 0.87	0.3 to 0.93	0.6 to 2.5

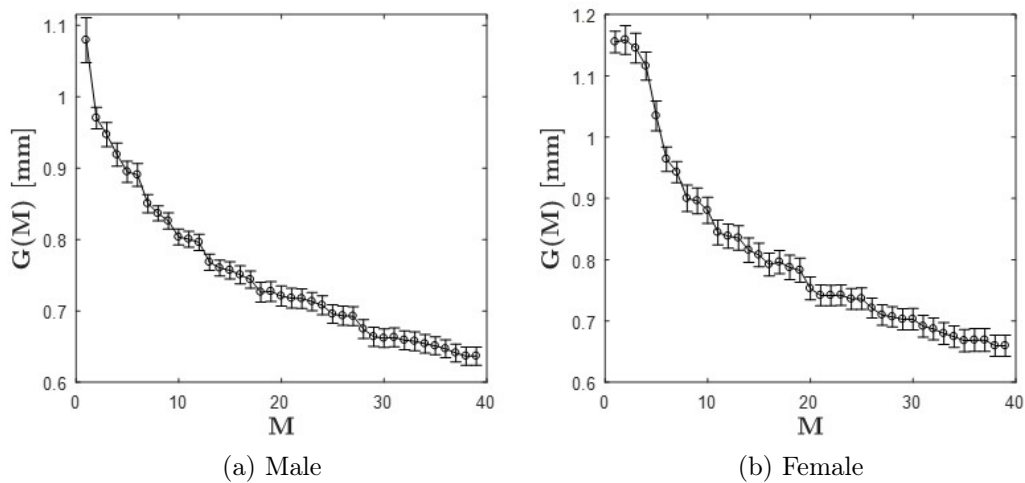


Figure 4.12: Generalization ability
(Illustration: RL Gillingham)

4.7 Discussion

The steps required to construct a SSM, as summarised in Figure 4.1, were carried out to create two gender-specific SSMs of the South African population. Each SSM was created from 40 mandibular surfaces. The quality of the resulting SSMs was tested using the evaluation measures described and carried out in Sections 4.5 and 4.6 respectively. The models performed well in all the of the evaluation measures.

4.7.1 Compactness

Both models proved to be compact, where relatively few modes were needed to capture the great majority of the population's variation (90%). In order to gain a visual image of shape variation, the shape parameters (b) of the models' modes were altered. A large amount of variation could be seen when altering the parameters of the first three modes (Tables 4.1 and 4.2). Despite the large amount of variation observed, the topology of the mandible remained intact, where only valid instances could be seen. For testing purposes, all 39 modes of the SSMs will be utilised, yet the amount of modes can be decreased without heavily affecting the amount of variation explained by the models. Due to the relatively few number of modes needed to capture the great majority of the dataset's variation, and the two models' good compactness comparative to a similar model in literature, we are satisfied that the models' are suitably compact.

4.7.2 Specificity

The current study's specificity range of 0.6 to 1.13 mm and 0.63 to 1.16 mm for the male and female models respectively, compare similarly to that of other models in literature (see Table 4.3). The comparatively satisfactory specificity ranges indicate that the models generate mandibular instances that are representative of the training data used to create the models.

4.7.3 Generality

Likewise with the specificity of the current study's models, the generalization ability compares similarly to other models on anatomical structures in literature (see Table 4.4). The study by Vanden Berghe *et al.* (2017) on using an SSM for the reconstruction of the acetabulum, reported a generality range of 0.7 to 2.75 mm. The model's subsequent ability to virtually reconstruct the acetabulum was tested. The results showed an improvement to other available reconstruction methods. The current study's SSMs have a generality range that compares favourably to this model. Seeing as that both SSMs have generalization abilities comparable to other successfully implemented SSMs in literature, we are satisfied with the models' ability to represent unseen mandibular shapes.

Chapter 5

Virtual Reconstruction

This chapter explores the use of the SPM and SSM devised during earlier chapters, for the virtual reconstruction of the mandible. This reconstruction was tested for two different scenarios, where each scenario consisted of two separate tests. The first test was the surface-to-surface error. For this test, the distance between the dense set of points that make up the estimated and ground truth shapes was calculated and reported as an RMSE. This test only applies to the SSM and mirroring techniques, as the SPM is limited to estimating measurements. The second test consisted of recording certain mandibular measurements on the estimated shapes that occur in the region of interest, and comparing these to the actual measurements taken on the ground truth shapes.

5.1 Testing procedure

The testing procedure was conducted for two different reconstruction scenarios. The first of these scenarios is for when the symmetrical plane is available and the second one for when this line of symmetry is not made available as the disruption on the mandible occurs on its front area. For both scenarios, ten healthy mandibular surfaces that were not part of the dataset used to create the SSM, each had a section removed. A reconstruction of the mandible took place using various methods. The methods' effectiveness were compared to each other using two evaluation techniques:

1. A surface-to-surface error calculated between the points of the estimated and actual surfaces at the reconstructed area. A two sample t-test was also conducted to calculate whether the differences in the various methods' accuracies were statistically significant.
2. Measurements based on landmarks occurring on the reconstructed area of the mandible were taken on the healthy and estimated mandibular

surfaces. A two sample t-test was also performed to calculate whether the difference between the ground truth and estimated measurements were statistically significant or not. Pearson's correlation coefficient was determined between the ground truth and estimated measurements for the different reconstruction techniques. This was to determine the extent of the mutual relationship that exists between the actual and estimated measurements.

5.1.1 First scenario

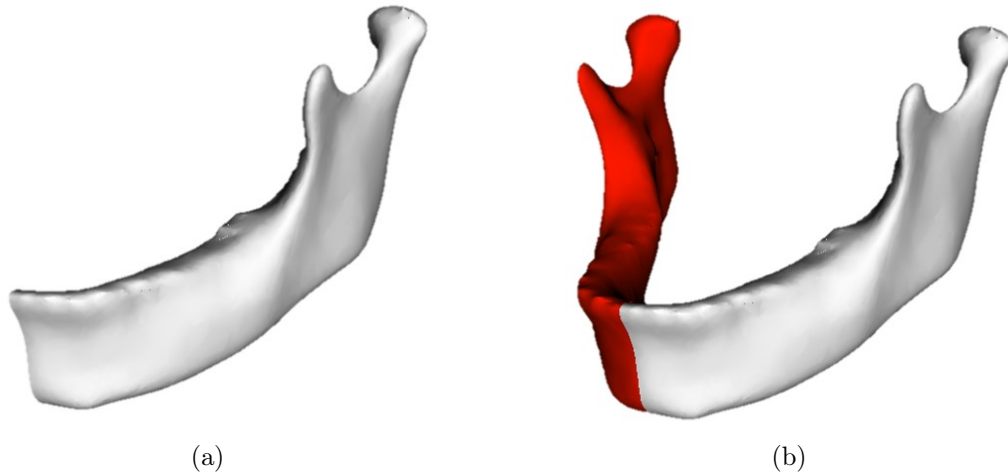


Figure 5.1: Reconstruction for first scenario
(Illustration: RL Gillingham)

For the first scenario of testing, the ground truth mandibular surfaces had half of their area removed (see Figure 5.1a). This was done by using the sagittal plane to divide each mandible into two halves and then removing either half in turn. This scenario served to replicate the situation where a patient's mandible is damaged on only one side, and a reconstruction can take place by mirroring the healthy portion of the mandible across the sagittal plane as an estimate for the damaged half. This mirroring method was compared to using an SSM or SPM to predict missing mandibular geometry when half the mandible is available as an input. The accuracy achieved by using the mirroring method served as the baseline accuracy for what is currently being achieved in practice. The location of the landmarks that were used as partial input for the SSM is shown in Figure C.1 (Appendix C).

5.1.2 Second scenario

For this scenario of testing, the front section of each mandibular surface was removed, as shown in Figure 5.2a. This was to mimic a reconstruction procedure in which the plane of symmetry is not available and the mirroring

method cannot be used. The devised geometry prediction techniques used the two flanges of the mandible as in input to estimate the geometry of the front section (Figure 5.2b). The location of the landmarks that were used as partial input for the SSM is shown in Figure C.2 (Appendix C).

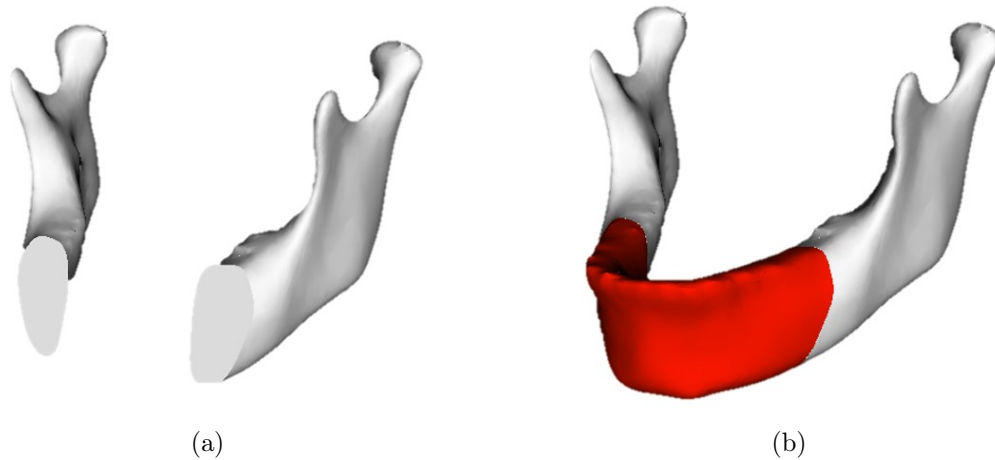


Figure 5.2: Reconstruction for first scenario
(Illustration: RL Gillingham)

5.2 Results

This section documents the summary of results obtained from the VSR tests. For a more detailed view on individual patient test results, see Appendix C.

5.2.1 First scenario

Table 5.1 displays the results of the surface-to-surface test done for the first scenario. The RMSE is reported as the mean (μ) and standard deviation (σ). This test was performed for the reconstruction of both the left and right halves of the mandible. The RMSE errors found using both methods were very similar, where no significant difference was found between the respective errors for both genders. Eight Measurements from the cephalometric analysis conducted in Chapter 3, that occur in the region of interest, were recorded using all three methods. A correlation coefficient (r) was calculated between the measurements obtained from the ground truth and estimated shapes, to show the extent of the linear relationship that exists between the actual and estimated measurements. Pearson's correlation was used for the data that followed a normal distribution, whilst Spearman's correlation was used otherwise. To test for this normality, a Lilliefors test was performed on each dataset. The two-sample t-test that was performed on the data, showed that no signifi-

cant difference was present between estimated and ground truth measurements when using any of the three techniques. The comparison between the three methods' effectiveness in predicting these measurements on the right half of the mandible is shown in Tables 5.2 and 5.3.

Table 5.1: First scenario: Surface-to-surface error

		Mirroring		SSM	
		Male	Female	Male	Female
		$\mu \pm \sigma$	$\mu \pm \sigma$	$\mu \pm \sigma$	$\mu \pm \sigma$
RMSE (right half)	[mm]	1.09±0.21	1.22±0.28	1.06±0.27	1.18±0.33
RMSE (left half)	[mm]	1.01±0.16	1.29±0.30	1.14±0.14	1.33±0.22

A r value of $r \geq 0.65$ will be considered to be a strong correlation, whilst anything else will be seen as poor. For the male population, estimated measurements occurring on the right half of the mandible using the mirroring method produced strong correlations in all of the measurements. The SSM and SPM estimations each showed strong correlations with the ground truth values in six of the eight measurements. In terms of the average error, the SSM and SPM, each outperformed the mirroring method in four of the eight measurements.

Table 5.2: First scenario: Male measurement estimation comparison for right half

Measurement		Mirroring		SSM		SPM	
		$\mu \pm \sigma$	r	$\mu \pm \sigma$	r	$\mu \pm \sigma$	r
Me angle	[°]	1.07±1.31	0.84 [†]	0.73±0.80	0.98	2.90±1.97	0.77
Me-Go-Co	[°]	1.84±2.26	0.79 [†]	2.32±2.68	0.66 [†]	2.43±2.04	0.72 [†]
Go-Sagittal	[mm]	1.96±2.28	0.79	1.52±1.67	0.79	1.48±0.98	0.88
Co-sagittal	[mm]	1.46±1.56	0.72 [†]	0.74±0.90	0.91 [†]	2.07±2.38	0.20 [†]
Co-Go	[mm]	1.50±1.62	0.79	1.95±2.29	0.37	1.54±1.18	0.26
Co-Sig	[mm]	0.97±1.06	0.96	1.56±1.94	0.62	0.66±0.56	0.98
Go-Me	[mm]	1.87±2.60	0.85	1.16±1.42	0.96	1.39±1.06	0.85 [†]
Co-in - Co-out	[mm]	1.14±1.22	0.66	1.30±1.23	0.77	0.73±0.73	0.72

[†] Spearman's correlation

As with the male subjects, the mirroring method's estimations showed strong correlations with the ground truth values in all of the measurements conducted on the right half of the female mandible. The SSM and SPM produced estimations that shared strong correlations with the ground truth values

in six and five of the eight measurements respectively. The average error in measurement prediction generated using the SSM and SPM methods outperformed the mirroring technique in four and one measurements respectively.

Table 5.3: First scenario: Female measurement estimation comparison for right half

Measurement		Mirroring		SSM		SPM	
		$\mu \pm \sigma$	r	$\mu \pm \sigma$	r	$\mu \pm \sigma$	r
Me angle	[°]	1.26±1.57	0.93	0.95±1.22	0.93	2.74±1.57	0.82
Me-Go-Co	[°]	2.06±2.25	0.87	2.18±3.19	0.62	2.75±2.16	0.42
Go-sagittal	[mm]	1.05±1.34	0.94	1.20±1.54	0.94	1.13±0.88	0.94
Co-sagittal	[mm]	0.95±1.43	0.85	0.70±1.20	0.87	1.40±1.53	0.46
Co-Go	[mm]	1.99±2.02	0.86	1.70±2.14	0.80	1.51±0.87	0.92
Co-Sig	[mm]	0.79±0.88	0.93	0.99±1.24	0.88	1.02±0.48	0.95
Go-Me	[mm]	1.12±1.14	0.97 [†]	0.90±1.06	0.98 [†]	1.59±0.90	0.91 [†]
Co-in - Co-out	[mm]	0.58±0.79	0.70	2.31±2.63	0.08	1.19±1.14	0.34

[†] Spearman's correlation

Tables 5.4 and 5.5 show the comparisons between the various methods' ability to predict measurements occurring on the left side of the mandible for the male and female populations respectively. For the male population, the mirroring method produced estimations that showed strong linear correlations with the ground truth values in all but one measurement (Co-sagittal).

Table 5.4: First scenario: Male measurement estimation comparison for left half

Measurement		Mirroring		SSM		SPM	
		$\mu \pm \sigma$	r	$\mu \pm \sigma$	r	$\mu \pm \sigma$	r
Me angle	[°]	1.21±1.37	0.90	0.78±1.02	0.96	3.37±2.28	0.75
Me-Go-Co	[°]	1.65±2.06	0.88	2.22±2.80	0.45	1.74±2.18	0.72
Go-Sagittal	[mm]	1.80±2.18	0.81	1.70±1.90	0.86	2.23±1.69	0.87
Co-sagittal	[mm]	1.17±1.40	0.54	0.66±1.29	0.83	2.43±1.98	0.20
Co-Go	[mm]	1.55±2.05	0.82	2.30±2.90	0.66	2.07±1.32	0.26
Co-Sig	[mm]	0.83±1.07	0.94	1.83±2.24	0.71	0.64±0.42	0.98
Go-Me	[mm]	1.45±2.30	0.90	1.63±1.86	0.93	1.94±0.91	0.68
Co-in - Co-out	[mm]	0.95±1.03	0.73	1.47±1.62	0.31	0.85±0.77	0.72

[†] Spearman's correlation

Both the SSM and SPM's estimations showed strong correlations with six of the eight measurements. When looking at the average error in measurement prediction, the SSM and SPM methods outperformed the mirroring method in three and two out of the eight measurements respectively. For the female population, the mirroring method's estimations correlated strongly with the ground truth values for every measurement, whilst the SSM and SPM methods produced estimations that showed strong correlations with the ground truth values in six and five out of the eight measurements respectively. The SSM and SPM's error in measurement estimation bettered that of the mirroring method in four and three measurements respectively.

Table 5.5: First scenario: Female measurement estimation comparison for left half

Measurement		Mirroring		SSM		SPM	
		$\mu \pm \sigma$	r	$\mu \pm \sigma$	r	$\mu \pm \sigma$	r
Me angle	[°]	1.96±2.05	0.85	0.89±1.13	0.96	2.93±2.06	0.82
Me-Go-Co	[°]	2.20±2.84	0.76	3.67±4.29	0.45	3.75±3.30	0.42
Go-sagittal	[mm]	1.04±1.25	0.96	0.70±0.92	0.97	1.56±0.78	0.95
Co-sagittal	[mm]	2.02±2.55	0.81	1.91±3.02	0.81	1.96±1.37	0.46
Co-Go	[mm]	1.67±2.08	0.85	2.54±2.94	0.61	1.99±1.24	0.92
Co-Sig	[mm]	0.92±1.20	0.91 [†]	1.61±2.24	0.70 [†]	0.86±0.48	0.95 [†]
Go-Me	[mm]	1.89±2.41	0.90	1.58±1.73	0.95	1.66±1.11	0.90
Co-in - Co-out	[mm]	0.66±0.80	0.74	1.73±1.27	0.67	1.54±1.20	0.34

[†] Spearman's correlation

5.2.2 Second scenario

Seeing as for the second scenario, the symmetrical plane is not made available, the mirroring method cannot be used. As a result, this section serves to report the geometry prediction effectiveness when using the SSM and SPM techniques. Table 5.6 displays the results of the surface-to-surface test done using the SSMs. The surface-to-surface error achieved using the male and female SSMs were similar. The error involved in predicting the front section of the mandible proved to be slightly higher than the values obtained in the first scenario, yet this difference was not significant.

Table 5.6: Second scenario: Surface to surface error

		Male	Female
		$\mu \pm \sigma$	$\mu \pm \sigma$
RMSE	[mm]	1.27±0.33	1.29±0.30

Seven measurements that occur in the region of interest were identified. The two methods' ability to predict these measurements for the male and female populations are shown in Tables 5.7 and 5.8 respectively. Similarly to the first scenario, no significant difference was found between the estimated and ground truth measurements for either technique. For the male population, the SSM's estimated measurements showed strong correlations in five of the seven measurements. The SPM produced measurements that showed strong correlations with the ground truth values in three measurements. With regards to the average error, the SSM outperformed the SPM in all but one measurement (Id-Me).

Table 5.7: Second scenario: Male measurement estimation comparison

Measurement		SSM		SPM	
		$\mu \pm \sigma$	r	$\mu \pm \sigma$	r
Me angle	[°]	0.45±0.58	0.99	2.56±1.54	0.66
Id-Me angle	[°]	2.12±3.03	0.62	5.01±4.85	0.38
Me-Go-Co (right)	[°]	1.13±1.30	0.94	3.35±2.15	0.28
Me-Go-Co (left)	[°]	0.84±1.06	0.84	2.88±1.97	0.13
Id-Me	[mm]	1.25±1.68	0.58	1.15±1.04	0.90
Me-Go (right)	[mm]	0.72±0.93	0.99	2.65±1.52	0.86
Me-Go (left)	[mm]	0.69±0.96	0.98	2.23±1.45	0.89 [†]

[†] Spearman's correlation

When testing on the female population, the SSM's estimated values showed strong correlations with the ground truth values in all of the measurements. The SPM produced estimations that showed strong correlations with the ground truth values in three measurements. The error in measurement estimation generated by the SSM bettered that of the SPM in every measurement.

Table 5.8: Second scenario: Female measurement estimation comparison

Measurement		SSM		SPM	
		$\mu \pm \sigma$	r	$\mu \pm \sigma$	r
Me angle	[°]	0.82±1.11	0.96	2.69±1.60	0.83
Id-Me angle	[°]	3.21±2.98	0.85 [†]	3.78±3.73	0.75 [†]
Me-Go-Co (right)	[°]	1.10±1.50	0.88	2.42±1.99	0.41
Me-Go-Co (left)	[°]	1.69±1.92	0.93	3.63±2.82	0.42
Id-Me	[mm]	1.16±1.20	0.96	1.68±1.48	0.90
Me-Go (right)	[mm]	1.46±1.88	0.94	2.89±2.67	0.50
Me-Go (left)	[mm]	1.27±1.69	0.96	2.83±1.99	0.62

[†] Spearman's correlation

5.3 Discussion

From the results, certain deductions could be made about the comparative effectiveness of the three investigated techniques. These deductions, as well as the implications of the results, are discussed in the following subsections.

5.3.1 First scenario

The first scenario of testing simulated situations where the symmetrical plane was available. The results of reconstruction using the mirroring method served as the baseline for the reconstruction accuracy that is currently being achieved. The effectiveness of the geometry prediction techniques devised during this study was then compared to this current golden standard. The estimations produced by the SSMs for both genders had a surface-to-surface error very similar to that of estimations produced using the mirroring method, where no significant differences were found between the two techniques' RMSE's. Mandibular measurements occurring in the region of interest were recorded using the three methods. These measurement estimations were then compared to the actual ground truth measurements. Generally speaking, the use of the SSMs and mirroring method, produced estimations that showed strong linear correlations with the ground truth measurements on a more consistent basis than when using the SPM, with the mirroring method being the most consistent of them all. The fact that these two methods also produce full representations of the mandible, whilst the SPM only offers a set of sparse measurement predictions, also adds to their favour. In terms of the accuracy in measurement prediction, the mirroring and SSM methods compared similarly. For the male and female testing, the SSMs produced better measurement estimations than the mirroring technique in seven and eight of the 16 (eight each on the left and right halves) measurements respectively. The SPM's estimated measurements achieved accuracies better than the mirroring method in six and four out of the 16 measurements for the male and female populations respectively. Seeing as the SPM produces measurement estimations that show inconsistent linear correlations with the ground truth values and weaker overall measurement estimation when compared to the mirroring method, we conclude that there is no clear benefit in using the SPM over the mirroring or SSM methods for shape estimation when the symmetrical plane is available. The use of an SSM however, shows comparatively similar reconstruction results to the method of mirroring, where no significant difference can be found between the effectiveness of both methods. The difference between these two methods lies in their restriction of use. The mirroring method can only be used in situations such as in the first scenario, whereas the SSM method extends to all reconstruction scenarios.

5.3.2 Second scenario

This scenario simulated a situation where a virtual reconstruction is required on the front section of the mandible and the symmetrical plane was unavailable. As a result, the mirroring method could not be used. The surface-to-surface error achieved by the SSM for both genders was very similar (see Table 5.6). The magnitude of these errors was slightly higher than the errors achieved using the mirroring method or SSMs in the first scenario, although these differences were not significant (i.e. $p > 0.05$). Although direct comparisons between the surface-to-surface errors obtained in the first and second scenarios are not recommended as different sections of the mandible are being reconstructed in each scenario, the fact that these errors are similar offers reasonable confidence that the reconstruction ability using the SSMs is similar regardless of the area in question. Mandibular measurements occurring in the reconstructed region were estimated using the prediction methods. These estimations (seven in total) were compared to the ground truth measurements. The SSMs produced estimations that showed strong linear correlations with the majority of the ground truth measurements. This was contrary to the SPM, whose estimations showed poor linear correlations with a large portion of the ground truth measurements (three of seven for male and four of seven for female). When looking at the accuracy in measurement prediction, the SSMs outperformed the SPMs in almost all the measurements (seven of eight for male and eight of eight for female). From these results, we conclude that an SSM is superior to that of the SPM technique in its geometry prediction ability.

5.3.3 Results summary

For both reconstruction scenarios, the use of an SSM performed better than the SPM. Not only does the SSM produce better estimations of mandibular measurements, but it also offers a full representation of the mandible. The SSMs reconstruction ability compared favourably to that of the mirroring technique, which serves as the golden standard in practice. This mirroring technique is limited, however, to situations where the symmetrical plane is available, whereas the SSM can be used for any reconstruction scenario.

Chapter 6

Conclusions

The aim set out at the commencement of this study was to formulate a pre-operative virtual mandibular reconstruction technique for the South African population, that accounts for the limitations present in current methods. It was proposed that such a technique could take the form of a prediction model based on statistical methods. This chapter offers conclusions on the extent to which the objectives have been fulfilled, recommendations on how to possibly improve the study and suggestions for future work.

6.1 Fulfilment of project objectives

Three objectives were formulated based on the study's aim. These objectives, as described in Chapter 1.3, were as follows:

1. Conduct a cephalometric analysis on the South African population. A SPM should be formulated using the correlations found between cephalometric measurements. This model must be able to predict unknown measurements from the input of other known measurements.
2. Construct a SSM of the mandible. This model must encapsulate the variation found in the population's mandibular structure. From partial input in the form of known mandibular coordinates, the SSM should offer a prediction for the most likely geometry of the missing region.
3. Evaluate the effectiveness of the developed models. A comparison should be made between these models and the mirroring technique. The mirroring technique serves as the baseline.

The extent to which these objectives were achieved is discussed in the following subsections.

6.1.1 Cephalometric analysis

The cephalometric analysis was performed on 40 male and female subjects. The sample size used for the study was calculated using parameters obtained from similar studies in literature. Once the results were finalised, this calculation was repeated using parameters obtained from the current study. The required sample size ended up being less than the amount used for the analysis, indicating that no further samples were required. The findings from the analysis compared similarly to that of other studies, where the male and female populations' skull structure was shown to be similar in shape, but not in size. The correlations existing between the cephalometric measurements were recorded and used to create regression functions that form the basis of the SPM. Strong linear relationships were shown to exist between bilateral measurements. These strong correlations combined with the fact that no significant difference was found between bilateral measurements, supports the intuitive observation of the mandible being symmetrical. High intra-rater reliability scores were reported, indicating that the study is very repeatable.

Due to the sufficient population size, similar findings to other studies in literature as well as the high reliability of the analysis, it was deemed that this objective was satisfied.

6.1.2 Statistical shape model

Using the same data analysed for the cephalometric analysis, two gender-specific SSMs were constructed. The GPA and GPMM methods were used in order to align and register the mandibular surfaces respectively. Modes of variation (directions in which the shapes change) were found by performing PCA on the point distributions. Objective evaluation measures that determine compactness, specificity and generality were performed on the SSMs. Both models performed well in all the evaluation measures, where comparisons were made with models found in literature. These models are able to produce estimates of the most likely geometry of missing regions by being fed known mandibular coordinates.

The objective of constructing a SSM was adjudged to have been satisfied. This was due to the satisfactory validation scores as well as the ability of these models to offer estimates of missing geometries from partial input.

6.1.3 Evaluation of techniques

A VSR testing procedure was set up to evaluate the effectiveness of the devised prediction models as well as to form a baseline for the accuracy that is currently being achieved in practice. Testing involved reconstructing missing

areas of mandibles not part of the dataset used to create the models. The mirroring method was used to establish a baseline reconstruction accuracy. The effectiveness of the mirroring method and SSM were very similar, where both methods comfortably outperformed the SPM. A scenario of testing also took place where the mirroring method couldn't be used, as the plane of symmetry was made unavailable. The SSM was still able to produce similar reconstruction accuracies during this scenario. This suggests that the SSM produces consistent reconstruction accuracies regardless of the region in question.

Both prediction models' effectiveness was compared to the VSR method that is used in practice. Results from testing suggest that a SSM accounts for limitations present in current methods. As a result, this objective was satisfied.

6.2 Recommendations

Despite the promising results shown by the SSMs during the virtual reconstruction scenarios, the following recommendations are put forward to possibly further improve their quality.

1. **Increase sample size:** Despite the popularity of PCA-based SSMs, the issue of data size sufficiency is not normally considered. As such, there is little literature on this issue (Mei *et al.*, 2008). Despite this, it is desired to increase the sample size used for both the cephalometric analysis and SSM construction to observe if the performance of these models improves.
2. **Correspondence improvement:** During the registration process, a reference shape must be chosen. This reference shape is then deformed to match the rest of the shapes in the training set in order to develop correspondence amongst the data. It has been documented that the representations of the training set after the registration process, show induced bias towards the chosen reference (Heimann and Meinzer, 2009). This was also noticed in the current study, where certain subtle characteristics found on the reference shape were present in many of the training set representations after the correspondence finding process. It is therefore recommended to use a more representative shape as the reference in order to reduce this biasing to one particular shape (Mutsvangwa *et al.*, 2015). Vos *et al.* (2004) and Clogenson *et al.* (2015) offer a method to reduce this biasing to the reference shape. This method involves calculating the mean shape of the training set once correspondence has been found amongst the data. This mean shape is then to be used as the reference shape and the correspondence finding process is repeated. This

is repeated until the calculated mean shape shows a negligible difference to the mean shape calculated in the previous iteration.

3. **Compare different correspondence techniques:** Although the method of using the GPMM technique to draw correspondence performed adequately, a more comprehensive evaluation of different correspondence finding techniques would be recommended. This can be done by performing the same evaluation measures done in Chapter 5 on each model using a different registration technique. By doing this, a conclusion can be made on whether a different registration method yields better correspondence results.
4. **Interobserver Repeatability:** The successful implementation of the predictive modelling techniques relies on the accurate identification of landmark positions. Section 3.5.4 showed that the intra-observer repeatability of the study is very high. The intra-observer error measures the repeatability in recording data by the same observer. Although satisfactory for a pilot study, it would be recommended to also perform an interobserver agreement test, in order to gather how reproducible results are if performed by different observers.

6.3 Future work

This study investigated the use of an SSM for virtual reconstruction purposes. This involves the model fitting scenario of matching the SSM surface to the surface of the target shape. This SSM can be adapted for the scenario of model fitting the surface of the SSM to an image. This adapted SSM is referred to as an active shape model (ASM) and was initially introduced by Cootes and Taylor (1995). One of the most popular uses of fitting a shape model to an image is for the segmentation process of anatomical structures, as seen in Figure 6.1 (Heimann and Meinzer 2009; Lüthi *et al.* 2017). Manual segmentation is extremely time-consuming. Clogenson *et al.* (2015) reported that manual segmentation of the C2 vertebra took, on average, one hour. A similar amount of time was spent when segmenting each mandibular surface in the current study. The active shape model search algorithm is an iterative approach, and proceeds as follows (Cootes *et al.*, 2000):

1. Examine the region of the image around each point on the ASM and find the best matching point on the image.
2. Estimate a transformation to be applied to the ASM in order to match these corresponding points.
3. Transform the reference points on the ASM using this transformation.
4. Iterate until convergence.

Where an SSM is made up of training data consisting of point coordinates making up the shape's surface, an ASM's training data consists of the same point coordinates as well as the image intensity profile that is experienced at each of these points. Each of these intensity profiles consists of information on the image intensity of the specified and neighboring points. Medical images are generally represented as grayscale images, as seen in Figure 6.2 . These images are therefore composed exclusively of shades of grey, varying from black at the weakest intensity to white at the strongest (Johnson, 2006). Therefore, when looking back at step 1 of the ASM search algorithm, the point on the image that best matches the point on the ASM is the point on the image whose image intensities surrounding that point best matches the ASM's point that has a similar intensity profile. The performing of an ASM search, as described by Cootes *et al.* (2000), is illustrated in Figure 6.2.

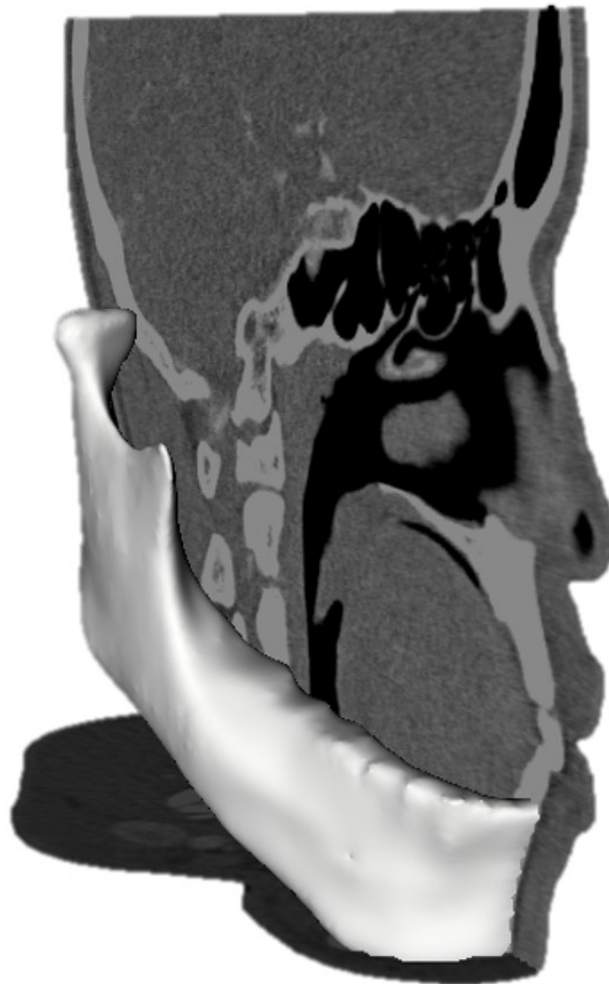


Figure 6.1: Automated segmentation
(Illustration: RL Gillingham)

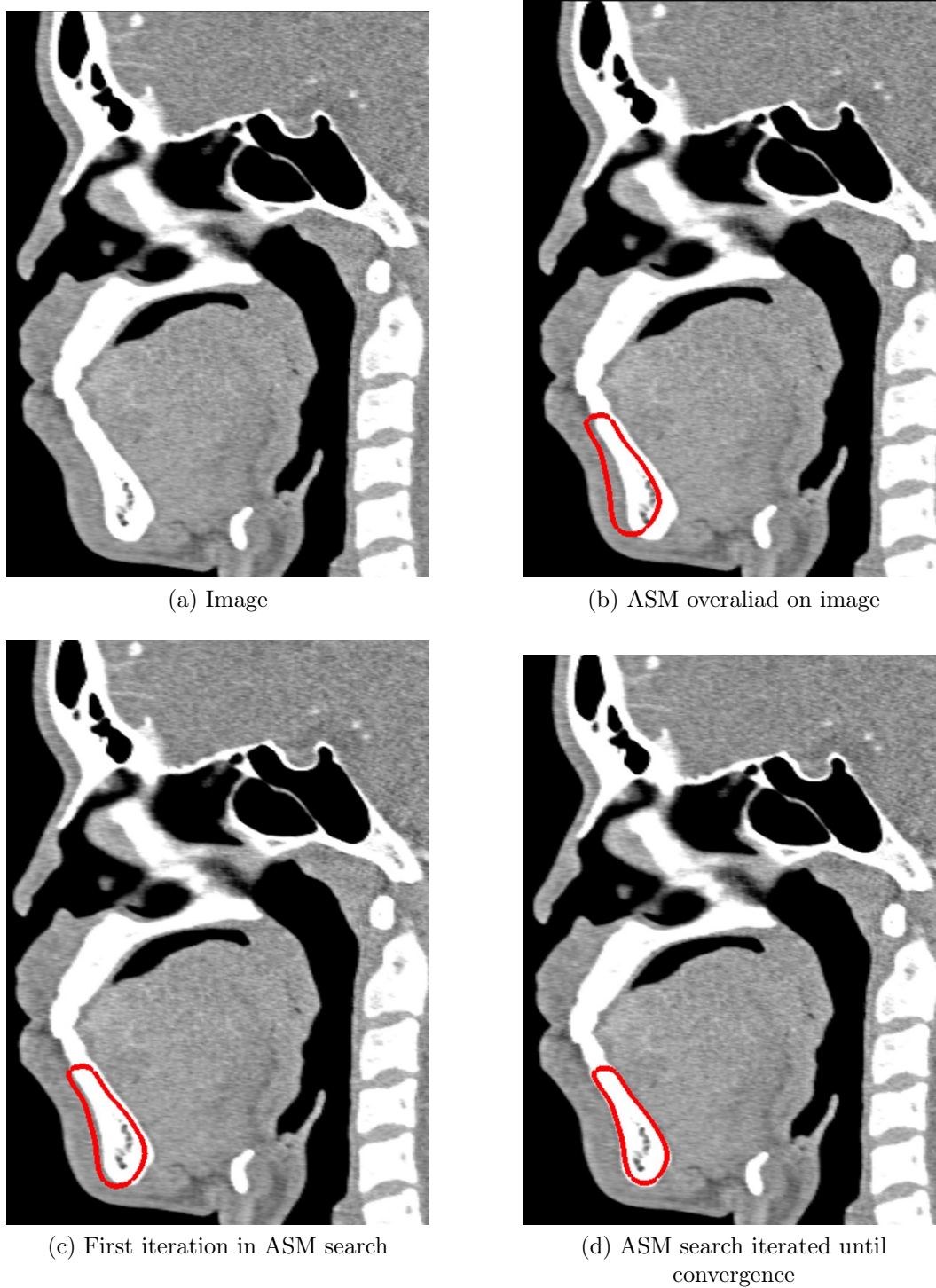


Figure 6.2: Active shape model search procedure
(Illustration: RL Gillingham)

6.4 Conclusion

The project objectives set out at the commencement of the study were fulfilled. Two prediction models (SPM and SSM) were formed that offer an estimation of missing mandibular geometry from partial input. The SSM produced reconstruction accuracies similar to that of the mirroring method. This mirroring technique is limited, however, to situations where the symmetrical plane is available, whereas the SSM was shown to produce estimations with similar accuracies regardless of the region being reconstructed. It is therefore concluded that a SSM presents itself as a modular VSR technique that successfully accounts for limitations existing in current methods.

List of References

- AAOMS (2015). *Corrective jaw surgery*. American Association of Oral and Maxillo-facial Surgeons.
- Abdolali, F., Zoroofi, R.A., Abdolali, M., Yokota, F., Otake, Y. and Sato, Y. (2017). Automatic segmentation of mandibular canal in cone beam ct images using conditional statistical shape model and fast marching. *International journal of computer assisted radiology and surgery*, vol. 12, no. 4, pp. 581–593.
- Abraham, D. (2014 December). Cephalometric analysis.
Available at: <http://https://cephx.com/Cephalometric-Analysis/>
- Ahlqvist, J., Eliasson, S. and Welander, U. (1983). The cephalographic projection. *Dentomaxillofacial Radiology*, vol. 12, no. 2, pp. 101–108.
- Al-Ahmari, A., Nasr, E.A., Moiduddin, K., Anwar, S., Kindi, M.A. and Kamrani, A. (2015). A comparative study on the customized design of mandibular reconstruction plates using finite element method. *Advances in Mechanical Engineering*, vol. 7, no. 7, p. 1687814015593890.
- Albrecht, T. (2011). *3D statistical shape models of human bones: their construction using a finite element registration algorithm, formulation on Hilbert spaces, and application to medical image analysis*. Ph.D. thesis, University_of_Basel.
- Altman, D.G. (1990). *Practical statistics for medical research*. CRC press.
- Asi, S.M., Ismail, N.H., Ahmad, R., Ramlan, E.I. and Rahman, Z.A.A. (2014). Automatic craniofacial anthropometry landmarks detection and measurements for the orbital region. *Procedia Computer Science*, vol. 42, pp. 372 – 377. ISSN 1877-0509. Medical and Rehabilitation Robotics and Instrumentation (MRRI2013).
Available at: <http://www.sciencedirect.com/science/article/pii/S1877050914015142>
- Audette, M.A., Ferrie, F.P. and Peters, T.M. (2000). An algorithmic overview of surface registration techniques for medical imaging. *Medical Image Analysis*, vol. 4, no. 3, pp. 201 – 217. ISSN 1361-8415.
Available at: <http://www.sciencedirect.com/science/article/pii/S1361841500000141>

- Baruah, N., Bora, M. *et al.* (2009). Cephalometric evaluation based on steiner analysis on young adults of assam. *J Indian Orthodontic Society*, vol. 43, no. 1, pp. 17–22.
- Baumrind, S., Carlson, S., Beers, A., Curry, S., Norris, K. and Boyd, R. (2003). Using three-dimensional imaging to assess treatment outcomes in orthodontics: a progress report from the university of the pacific. *Orthodontics & craniofacial research*, vol. 6, pp. 132–142.
- Bayome, M., Park, J.H. and Kook, Y.-A. (2013). New three-dimensional cephalometric analyses among adults with a skeletal class i pattern and normal occlusion. *The Korean Journal of Orthodontics*, vol. 43, no. 2, pp. 62–73.
- Besl, P.J. and McKay, N.D. (1992). Method for registration of 3-d shapes. In: *Sensor Fusion IV: Control Paradigms and Data Structures*, vol. 1611, pp. 586–607. International Society for Optics and Photonics.
- Cevidanes, L.H., L Tanya, J.B., Tucker, S.F., Styner, M.A., Mol, A., Phillips, C.L., Proffit, W.R. and Turvey, T. (2007). Three-dimensional cone-beam computed tomography for assessment of mandibular changes after orthognathic surgery. *American journal of orthodontics and dentofacial orthopedics*, vol. 131, no. 1, pp. 44–50.
- Cheung, L.K., Chan, Y.M., Jayaratne, Y.S. and Lo, J. (2011). Three-dimensional cephalometric norms of chinese adults in hong kong with balanced facial profile. *Oral Surgery, Oral Medicine, Oral Pathology, Oral Radiology, and Endodontology*, vol. 112, no. 2, pp. e56–e73.
- Chow, S.-C., Shao, J., Wang, H. and Lokhnygina, Y. (2017). *Sample size calculations in clinical research*. Chapman and Hall/CRC.
- Cicchetti, D.V. (1994). Guidelines, criteria, and rules of thumb for evaluating normed and standardized assessment instruments in psychology. *Psychological assessment*, vol. 6, no. 4, p. 284.
- Clogenson, M., Duff, J.M., Luethi, M., Levivier, M., Meuli, R., Baur, C. and Henein, S. (2015). A statistical shape model of the human second cervical vertebra. *International journal of computer assisted radiology and surgery*, vol. 10, no. 7, pp. 1097–1107.
- Cohen, M.I. (1965). Mandibular prognathism. *American Journal of Orthodontics and Dentofacial Orthopedics*, vol. 51, no. 5, pp. 368–379.
- Cootes, T., Baldock, E. and Graham, J. (2000). An introduction to active shape models. *Image processing and analysis*, pp. 223–248.
- Cootes, T.F. and Taylor, C.J. (1995). Combining point distribution models with shape models based on finite element analysis. *Image and Vision Computing*, vol. 13, no. 5, pp. 403–409.
- Daly, L. and Bourke, G.J. (2008). *Interpretation and uses of medical statistics*. John Wiley & Sons.

- Davies, R.H. (2002). *Learning shape: optimal models for analysing natural variability*. University of Manchester Manchester.
- Dempster, A.P., Laird, N.M. and Rubin, D.B. (1977). Maximum likelihood from incomplete data via the em algorithm. *Journal of the royal statistical society. Series B (methodological)*, pp. 1–38.
- Downs, W.B. (1948). Variations in facial relationships: their significance in treatment and prognosis. *American journal of orthodontics*, vol. 34, no. 10, pp. 812–840.
- Eraly, K., Debeer, P., Gelaude, F., Clijmans, T., Jonkers, I. and Vander Sloten, J. (2011). Ct-based virtual shape reconstruction for severe glenoid bone defects.
- Fehrenbach, M.J. and Herring, S.W. (2015). *Illustrated Anatomy of the Head and Neck-E-Book*. Elsevier Health Sciences.
- Fleute, M., Lavallée, S. and Julliard, R. (1999). Incorporating a statistically based shape model into a system for computer-assisted anterior cruciate ligament surgery. *Medical Image Analysis*, vol. 3, no. 3, pp. 209–222.
- Flynn, T.R., Ambrogio, R.I. and Zeichner, S.J. (1989). Cephalometric norms for orthognathic surgery in black american adults. *Journal of Oral and Maxillofacial Surgery*, vol. 47, no. 1, pp. 30–38.
- Friede, H., Kahnberg, K.-E., Adell, R. and Ridell, A. (1987). Accuracy of cephalometric prediction in orthognathic surgery. *Journal of Oral and Maxillofacial Surgery*, vol. 45, no. 9, pp. 754–760.
- Ganapathi, A., McCarron, J.A., Chen, X. and Iannotti, J.P. (2011). Predicting normal glenoid version from the pathologic scapula: a comparison of 4 methods in 2-and 3-dimensional models. *Journal of shoulder and elbow surgery*, vol. 20, no. 2, pp. 234–244.
- Goldberg, B.B., Isard, H.I., Gershon-Cohen, J. and Ostrum, B.J. (1966). Ultrasonic fetal cephalometry. *Radiology*, vol. 87, no. 2, pp. 328–332.
- Han, H.H., Kim, H.Y. and Lee, J.Y. (2017). The pros and cons of computer-aided surgery for segmental mandibular reconstruction after oncological surgery. *Archives of craniofacial surgery*, vol. 18, no. 3, pp. 149–154.
- Harnsberger, H.R., Osborn, A.G., Ross, J. and Macdonald, A. (2006). *Diagnostic and surgical imaging anatomy: brain, head & neck, spine*. Amirsys Salt Lake City.
- Heimann, T. and Meinzer, H.-P. (2009). Statistical shape models for 3d medical image segmentation: A review. *Medical Image Analysis*, vol. 13, no. 4, pp. 543 – 563. ISSN 1361-8415.
Available at: <http://www.sciencedirect.com/science/article/pii/S1361841509000425>

- Henderson, D. (1974). The assessment and management of bony deformities of the middle and lower face. *Journal of Plastic, Reconstructive & Aesthetic Surgery*, vol. 27, no. 3, pp. 287–296.
- Huang, W.-J., Taylor, R.W. and Dasanayake, A.P. (1998). Determining cephalometric norms for caucasians and african americans in birmingham. *The angle orthodontist*, vol. 68, no. 6, pp. 503–512.
- Hyndman, R.J. and Koehler, A.B. (2006). Another look at measures of forecast accuracy. *International Journal of Forecasting*, vol. 22, no. 4, pp. 679 – 688. ISSN 0169-2070.
Available at: <http://www.sciencedirect.com/science/article/pii/S0169207006000239>
- Jacks, S.C., Zuniga, J.R., Turvey, T.A. and Schalit, C. (1998). A retrospective analysis of lingual nerve sensory changes after mandibular bilateral sagittal split osteotomy. *Journal of oral and maxillofacial surgery*, vol. 56, no. 6, pp. 700–704.
- Johnson, S. (2006). *Stephen Johnson on digital photography*. O'Reilly Media, Inc.
- Judd, K.L. and Judd, K.L. (1998). *Numerical methods in economics*. MIT press.
- Jurda, M., Urbanovı, P. and Krılık, M. (2015). The post-mortem pressure distortion of human crania uncovered in an early medieval pohansko (czech republic) graveyard. *International Journal of Osteoarchaeology*, vol. 25, no. 4, pp. 539–549. ISSN 1099-1212.
Available at: <http://dx.doi.org/10.1002/oa.2321>
- Kadam, P. and Bhalerao, S. (2010). Sample size calculation. *International journal of Ayurveda research*, vol. 1, no. 1, p. 55.
- Kallenberger, L. and Pilbrow, V. (2012). Using cranium to test the population affinity of known crania. *Journal of anatomy*, vol. 221, no. 5, pp. 459–464.
- Kim, S.-G. and Park, S.-S. (2007). Incidence of complications and problems related to orthognathic surgery. *Journal of Oral and Maxillofacial Surgery*, vol. 65, no. 12, pp. 2438–2444.
- Kirke, D.N., Owen, R.P., Carrao, V., Miles, B.A. and Kass, J.I. (2016). Using 3d computer planning for complex reconstruction of mandibular defects. *Cancers of the Head & Neck*, vol. 1, no. 1, p. 17.
- Kolokitha, O.-E. and Topouzelis, N. (2011). Cephalometric methods of prediction in orthognathic surgery. *Journal of maxillofacial and oral surgery*, vol. 10, no. 3, p. 236.
- Kondo, S., Katsuta, H., Akizuki, A., Kurihara, Y., Kamatani, T., Yaso, A., Nagasaki, M., Shimane, T. and Shirota, T. (2015). Computer-assisted surgery for mandibular reconstruction using a patient-specific titanium mesh tray and particulate cancellous bone and marrow. *Case Reports in Clinical Medicine*, vol. 4, no. 03, p. 85.

- Koo, T.K. and Li, M.Y. (2016). A guideline of selecting and reporting intraclass correlation coefficients for reliability research. *Journal of chiropractic medicine*, vol. 15, no. 2, pp. 155–163.
- Lanigan, D.T. and West, R.A. (1990). Aseptic necrosis of the mandible: report of two cases. *Journal of Oral and Maxillofacial Surgery*, vol. 48, no. 3, pp. 296–300.
- Lavallee, S. (1996). Registration for computer-integrated surgery: methodology. *Computer-Integrated Surgery: Technology and Clinical Applications*, p. 77.
- Lee Rodgers, J. and Nicewander, W.A. (1988). Thirteen ways to look at the correlation coefficient. *The American Statistician*, vol. 42, no. 1, pp. 59–66.
- Lorusso, A., Eggert, D.W. and Fisher, R.B. (1995). *A comparison of four algorithms for estimating 3-D rigid transformations*. University of Edinburgh, Department of Artificial Intelligence.
- Ludlow, J.B., Gubler, M., Cevidanes, L. and Mol, A. (2009). Precision of cephalometric landmark identification: cone-beam computed tomography vs conventional cephalometric views. *American Journal of Orthodontics and Dentofacial Orthopedics*, vol. 136, no. 3, pp. 312–e1.
- Lüthi, M., Blanc, R., Albrecht, T., Gass, T., Goksel, O., Büchler, P., Kistler, M., Bousleiman, H., Reyes, M., Cattin, P. *et al.* (2012). Statismo—a framework for pca based statistical models. *The Insight Journal*, vol. 2012, pp. 1–18.
- Lüthi, M., Forster, A., Gerig, T. and Vetter, T. (2017). Shape modeling using gaussian process morphable models. *Statistical Shape and Deformation Analysis: Methods, Implementation and Applications*, p. 165.
- Manmadhachary, A., Malyala, S.K., Kumar, R., Alwala, A. *et al.* (2017). Design & manufacturing of implant for reconstructive surgery: A case study. *KnE Engineering*, vol. 2, no. 2, pp. 143–149.
- Martis, C. and Karabouta, I. (1984). Infection after orthognathic surgery, with and without preventive antibiotics. *International journal of oral surgery*, vol. 13, no. 6, pp. 490–494.
- Mayya, M., Poltaretskyi, S., Hamitouche, C. and Chaoui, J. (2015). Mesh correspondence improvement using regional affine registration: Application to statistical shape model of the scapula. *Irbm*, vol. 36, no. 4, pp. 220–232.
- McNeill, R.W., Proffit, W.R. and White, R.P. (1972). Cephalometric prediction for orthodontic surgery. *The Angle orthodontist*, vol. 42, no. 2, pp. 154–164.
- Mehra, P., Cottrell, D.A., Caiazzo, A. and Lincoln, R. (1999). Life-threatening, delayed epistaxis after surgically assisted rapid palatal expansion: a case report. *Journal of oral and maxillofacial surgery*, vol. 57, no. 2, pp. 201–204.

- Mei, L., Figl, M., Darzi, A., Rueckert, D. and Edwards, P. (2008). Sample sufficiency and pca dimension for statistical shape models. In: *European Conference on Computer Vision*, pp. 492–503. Springer.
- Miura, F., Inoue, N. and Suzuki, K. (1965). Cephalometric standards for japanese according to the steiner analysis. *American journal of orthodontics*, vol. 51, no. 4, pp. 288–295.
- Mohammed, M., Fitzpatrick, A., Malyala, S. and Gibson, I. (2016). Customised design and development of patient specific 3d printed whole mandible implant. In: *Proceedings of the 27th Annual International Solid Freeform Fabrication Symposium*, pp. 1708–1717.
- Mutsvangwa, T., Burdin, V., Schwartz, C. and Roux, C. (2015). An automated statistical shape model developmental pipeline: application to the human scapula and humerus. *IEEE Transactions on Biomedical Engineering*, vol. 62, no. 4, pp. 1098–1107.
- Myronenko, A. and Song, X. (2010). Point set registration: Coherent point drift. *IEEE transactions on pattern analysis and machine intelligence*, vol. 32, no. 12, pp. 2262–2275.
- Nair, P. and Cavallaro, A. (2009 June). 3-d face detection, landmark localization, and registration using a point distribution model. *IEEE Transactions on Multimedia*, vol. 11, no. 4, pp. 611–623. ISSN 1520-9210.
- Pandis, N., Polychronopoulou, A. and Eliades, T. (2011). Sample size estimation: an overview with applications to orthodontic clinical trial designs. *American journal of orthodontics and dentofacial orthopedics*, vol. 140, no. 4, pp. e141–e146.
- Parthasarathy, J., Starly, B. and Raman, S. (2009). Computer aided biomodeling and analysis of patient specific porous titanium mandibular implants. *Journal of Medical Devices*, vol. 3, no. 3, p. 031007.
- Plessers, K., Berghe, P.V., Van Dijck, C., Wirix-Speetjens, R., Debeer, P., Jonkers, I. and Vander Sloten, J. (2018). Virtual reconstruction of glenoid bone defects using a statistical shape model. *Journal of shoulder and elbow surgery*, vol. 27, no. 1, pp. 160–166.
- Proffit, W.R., Fields Jr, H.W. and Sarver, D.M. (2006). *Contemporary orthodontics*. Elsevier Health Sciences.
- Qaisi, M., Kolodney, H., Swedenburg, G., Chandran, R. and Caloss, R. (2016). Fibula jaw in a day: state of the art in maxillofacial reconstruction. *Journal of Oral and Maxillofacial Surgery*, vol. 74, no. 6, pp. 1284–e1.
- Rao, S.B., Singaraju, G.s., Mandava, P. and Ganugapanta, V.R. (2015). Cephalometric analysis for orthognathic surgery. *Annals and Essences of Dentistry*, vol. 7, no. 3, pp. 1c–10c.

- Rasmussen, C.E. and Williams, C.K. (2006). *Gaussian processes for machine learning*, vol. 1. MIT press Cambridge.
- Ricketts, R.M. (1961). Cephalometric analysis and synthesis. *The Angle Orthodontist*, vol. 31, no. 3, pp. 141–156.
- Scala, A., Auconi, P., Scazzocchio, M., Caldarelli, G., McNamara, J.A. and Franchi, L. (2012). Using networks to understand medical data: the case of class iii malocclusions. *PloS one*, vol. 7, no. 9, p. e44521.
- Scalise, J.J., Codi, M.J., Bryan, J. and Iannotti, J.P. (2008). The three-dimensional glenoid vault model can estimate normal glenoid version in osteoarthritis. *Journal of shoulder and elbow surgery*, vol. 17, no. 3, pp. 487–491.
- Schultes, G., Gaggl, A. and Kärcher, H. (1998). Periodontal disease associated with interdental osteotomies after orthognathic surgery. *Journal of oral and maxillofacial surgery*, vol. 56, no. 4, pp. 414–417.
- Shlens, J. (2014). A tutorial on principal component analysis. *arXiv preprint arXiv:1404.1100*.
- Singare, S., Shenggui, C. and Sheng, L. (2017). The use of 3 d printing technology in human defect reconstruction-a review of cases study.
- Snedecor, G.W. and Cochran, W.G. (1989). *Statistical methods*, 8thedn. Ames: Iowa State Univ. Press Iowa.
- Standring, S. (2015). *Gray's anatomy e-book: the anatomical basis of clinical practice*. Elsevier Health Sciences.
- Steiner, C.C. (1953). Cephalometrics for you and me. *American Journal of Orthodontics*, vol. 39, no. 10, pp. 729–755.
- Styner, M.A., Rajamani, K.T., Nolte, L.-P., Zsemlye, G., Székely, G., Taylor, C.J. and Davies, R.H. (2003). Evaluation of 3d correspondence methods for model building. In: *Biennial International Conference on Information Processing in Medical Imaging*, pp. 63–75. Springer.
- Subsol, G., Thirion, J.-P. and Ayache, N. (1998). A scheme for automatically building three-dimensional morphometric anatomical atlases: application to a skull atlas. *Medical image analysis*, vol. 2, no. 1, pp. 37–60.
- Synthes (2012). *MatrixMandible Performed Reconstruction Plates. Preshaped to mandibular anatomy*.
- Tenti, F.V. (1981). Cephalometric analysis as a tool for treatment planning and evaluation. *European Journal of Orthodontics*, vol. 3, no. 4, p. 241. [/oup/backfile/contentpublic/journal/ejo/3/4/10.1093/ejo3.4.241/3/3-4-241.pdf](#). Available at: [+http://dx.doi.org/10.1093/ejo/3.4.241](http://dx.doi.org/10.1093/ejo/3.4.241)

- Thilander, B., Persson, M. and Adolfsson, U. (2005). Roentgen–cephalometric standards for a swedish population. a longitudinal study between the ages of 5 and 31 years. *The European Journal of Orthodontics*, vol. 27, no. 4, pp. 370–389.
- Tortora, G.J. and Derrickson, B.H. (2008). *Principles of anatomy and physiology*. John Wiley & Sons.
- Vahdettin, L., Aksoy, S., ÖZ, U. and Orhan, K. (2016). Three-dimensional cephalometric norms of turkish cypriots using cbctimages reconstructed from a volumetric rendering program in vivo. *Turkish journal of medical sciences*, vol. 46, no. 3, pp. 848–861.
- Van der Merwe, J. (2018). *Development of a patient-specific unicompartmental knee replacement*. Ph.D. thesis, Stellenbosch: Stellenbosch University.
- Vanden Berghe, P., Demol, J., Gelaude, F. and Vander Sloten, J. (2017). Virtual anatomical reconstruction of large acetabular bone defects using a statistical shape model. *Computer methods in biomechanics and biomedical engineering*, vol. 20, no. 6, pp. 577–586.
- Vos, F., de Bruin, P.W., Aubel, J., Streekstra, G.J., Maas, M., van Vliet, L.J. and Vossepoel, A.M. (2004). A statistical shape model without using landmarks. In: *Pattern Recognition, 2004. ICPR 2004. Proceedings of the 17th International Conference on*, vol. 3, pp. 714–717. IEEE.
- Wical, K.E. and Swoope, C.C. (1974). Studies of residual ridge resorption. part i. use of panoramic radiographs for evaluation and classification of mandibular resorption. *The Journal of Prosthetic Dentistry*, vol. 32, no. 1, pp. 7 – 12. ISSN 0022-3913.
Available at: <http://www.sciencedirect.com/science/article/pii/S0022391374900936>
- Wilson, A. and Adams, R. (2013). Gaussian process kernels for pattern discovery and extrapolation. In: *International Conference on Machine Learning*, pp. 1067–1075.
- Zachow, S., Lamecker, H., Elsholtz, B. and Stiller, M. (2005). Reconstruction of mandibular dysplasia using a statistical 3d shape model. *International Congress Series*, vol. 1281, pp. 1238 – 1243. ISSN 0531-5131. CARS 2005: Computer Assisted Radiology and Surgery.
Available at: <http://www.sciencedirect.com/science/article/pii/S053151310500600X>
- Zhang, J. and Besier, T.F. (2017). Accuracy of femur reconstruction from sparse geometric data using a statistical shape model. *Computer methods in biomechanics and biomedical engineering*, vol. 20, no. 5, pp. 566–576.
- Zielinski, E., Jacobs, R.J., Barker, E., Rodby, K. and Antony, A.K. (2015). Virtual surgical planning in craniomaxillofacial reconstruction. In: *A Textbook of Advanced Oral and Maxillofacial Surgery Volume 2*. InTech.

Appendices

Appendix A

Sample Size Calculation

The software program, Matlab, has a built-in library function to calculate the required sample size. This function takes in the effect size, shared standard deviation (σ), power ($1-\beta$) and the ratio between the two populations as an input, whilst assuming the type 1 error (α) to be 0.05.

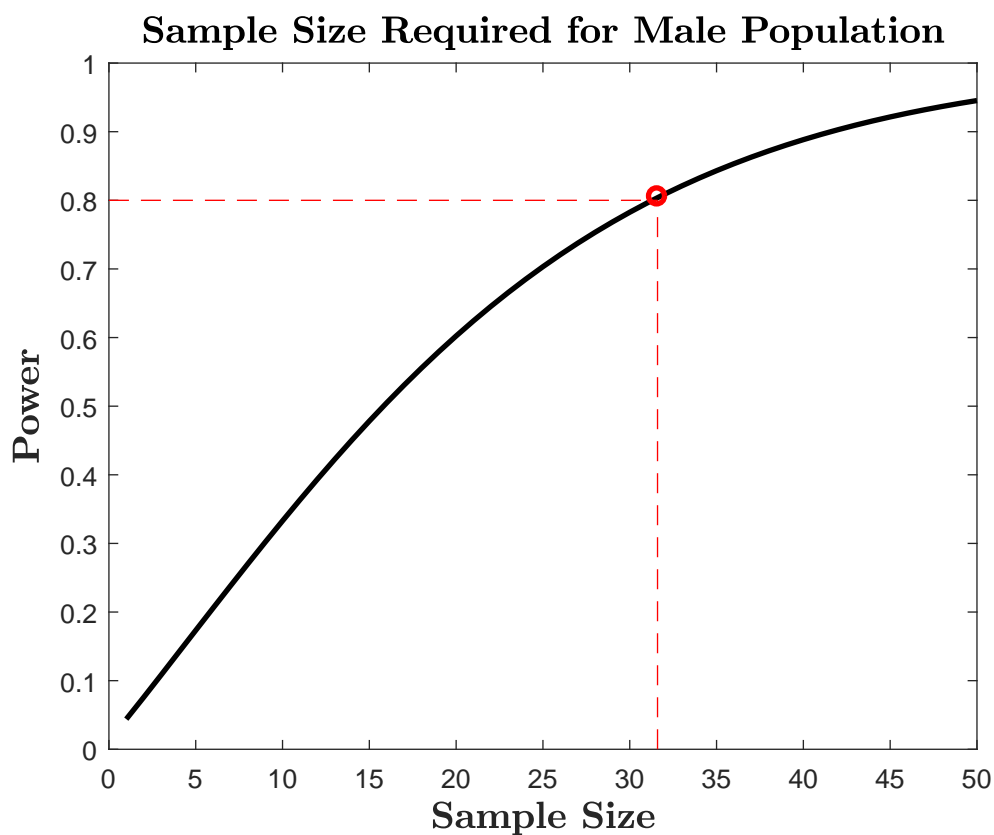


Figure A.1: Required sample size for male population

Figures A.1 and A.1 illustrate the initial sample size required for a desired power for the male and female populations respectively. For a power score of 0.8, 32 male and 36 female subjects were needed. This compares favourably to the sample sizes calculated using Equation 3.1. For conservativeness, it was decided that 40 scans for each gender would be collected.

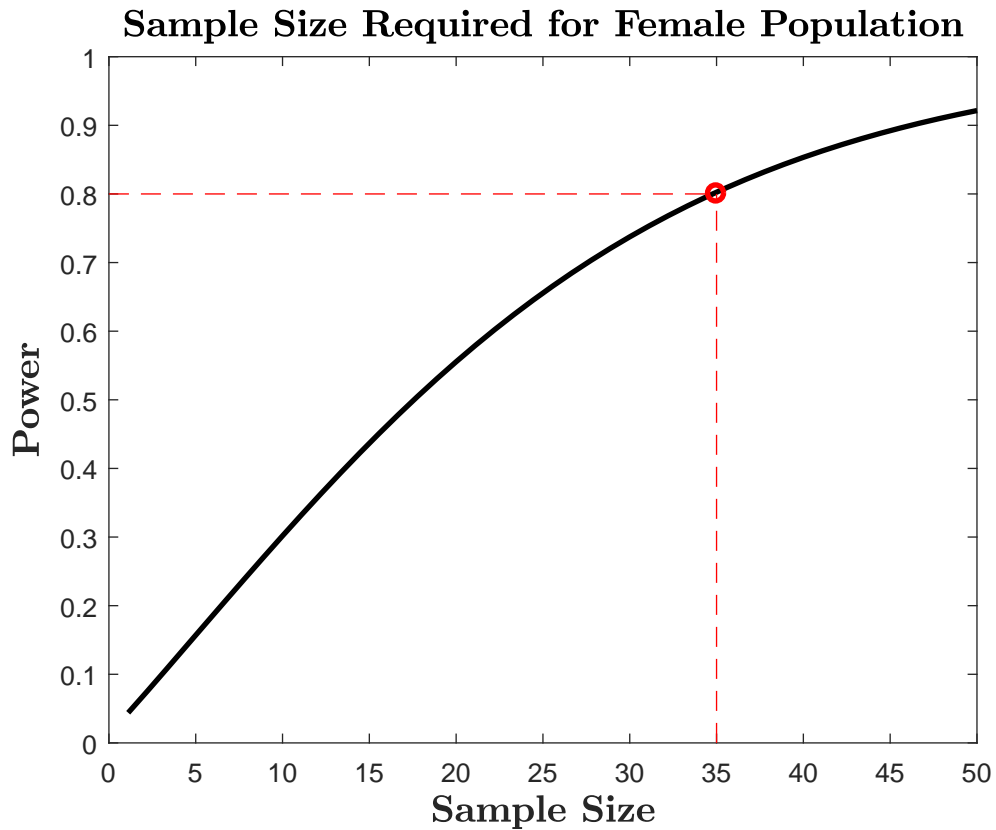


Figure A.2: Required sample size for female population

This calculation was repeated at the end of the study. The updated parameters fed into Equation 3.1 were obtained from the results of the current study. The revised sample size required equated to 35 subjects for both the male and female populations. Figure A.3 displays this result.

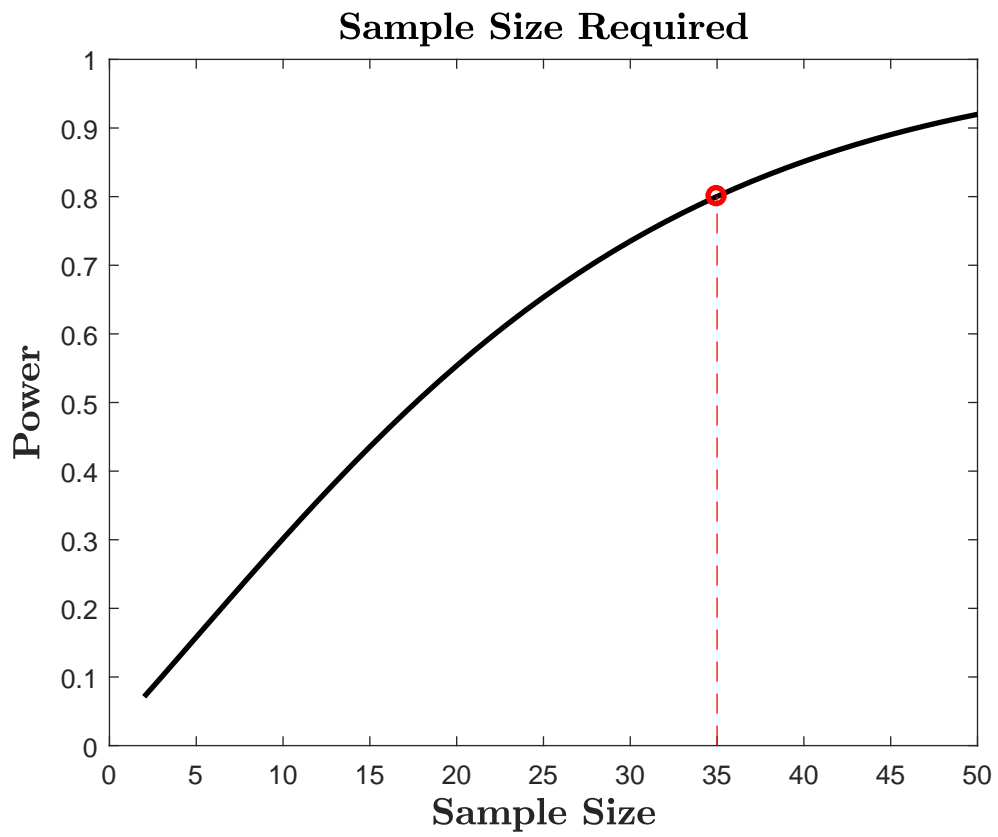


Figure A.3: Updated sample size requirement

Appendix B

SPM Algorithms

This chapter offers the regression algorithms that form part of the Sparse Prediction Model (SPM). This model serves to offer an estimate of unknown measurements by taking the value of known, available measurements as an input. Only those known measurements that share a strong correlation with the unknown measurement are used as an input. The algorithms are based on the regression formula represented by Equation B.1. P , μ_P , Σ_{PO} , Σ_{OO} and U represents the measurement to be predicted, the mean value of this measurement, the covariances between the predicted and observed values, the covariances between the observed values and the difference between the observed measurements and the mean value of the observed measurements respectively.

$$P = \mu_P + \Sigma_{PO}^T \Sigma_{OO}^{-1} U \quad (\text{B.1})$$

B.1 Male Algorithms

B.1.1 First scenario

Estimated	Symbol	Available	Symbol
Me angle	P	Go-Sagittal (right)	O

$$P = 62.30 + [13.53] \cdot [11.11]^{-1} \cdot [O - 46.99] \quad (\text{B.2})$$

Estimated	Symbol	Available	Symbol
Me-Go-Co (right)	P1	Me-Go-Co (left)	O1
Me-Go-Co (left)	P2	Me-Go-Co (right)	O2

$$\begin{aligned}
P1 &= 115.34 + [10.96] \cdot [17.74]^{-1} \cdot [O1 - 115.93] \\
P2 &= 115.93 + [10.96] \cdot [14.27]^{-1} \cdot [O2 - 115.34]
\end{aligned}
\tag{B.3}$$

Estimated	Symbol	Available	Symbol
Go-Sagittal (right)	P1	Go-Sagittal (left)	O1
Go-Sagittal (left)	P2	Go-Sagittal (right)	O2

$$\begin{aligned}
P1 &= 46.99 + [8.09] \cdot [9.65]^{-1} \cdot [O1 - 44.93] \\
P2 &= 44.93 + [8.09] \cdot [11.11]^{-1} \cdot [O2 - 46.99]
\end{aligned}
\tag{B.4}$$

Estimated	Symbol	Available	Symbol
Co-Sagittal (right)	P1	Co-Sagittal(left)	O1
Co-Sagittal (left)	P2	Co-Sagittal (right)	O2

$$\begin{aligned}
P1 &= 50.72 + [4.64] \cdot [7.56]^{-1} \cdot [O1 - 50.04] \\
P2 &= 50.04 + [4.64] \cdot [8.03]^{-1} \cdot [O2 - 50.72]
\end{aligned}
\tag{B.5}$$

Estimated	Symbol	Available	Symbol
Co-Go (right)	P1	Co-Go (left)	O1
Co-Go (left)	P2	Co-Go (right)	O2

$$\begin{aligned}
P1 &= 58.52 + [10.17] \cdot [15.29]^{-1} \cdot [O1 - 57.69] \\
P2 &= 57.69 + [10.17] \cdot [12.14]^{-1} \cdot [O2 - 58.52]
\end{aligned}
\tag{B.6}$$

Estimated	Symbol	Available	Symbol
Co-Sig (right)	P1	Co-Sig (left)	O1
Co-Sig (left)	P2	Co-Sig (right)	O2

$$\begin{aligned} P1 &= 18.61 + [7.52] \cdot [9.32]^{-1} \cdot [O1 - 18.21] \\ P2 &= 18.21 + [7.52] \cdot [7.77]^{-1} \cdot [O2 - 18.61] \end{aligned} \quad (\text{B.7})$$

Estimated	Symbol	Available	Symbol
Go-Me (right)	P1	Facial angle	O1
		Go-Me (left)	O2
Go-Me (left)	P2	Facial angle	O3
		Go-Me (right)	O4

$$\begin{aligned} P1 &= 89.40 + [8.07 \quad 24.13] \cdot \begin{bmatrix} 5.61 & 9.49 \\ 9.49 & 31.18 \end{bmatrix}^{-1} \cdot \begin{bmatrix} O1 - 87.24 \\ O2 - 89.06 \end{bmatrix} \\ P2 &= 89.06 + [9.49 \quad 24.13] \cdot \begin{bmatrix} 5.61 & 8.07 \\ 8.07 & 22.84 \end{bmatrix}^{-1} \cdot \begin{bmatrix} O3 - 87.24 \\ O4 - 89.40 \end{bmatrix} \end{aligned} \quad (\text{B.8})$$

Estimated	Symbol	Available	Symbol
Co-in - Co-out (right)	P1	Co-in - Co-out (left)	O1
Co-in - Co-out (left)	P2	Co-in - Co-out (right)	O2

$$\begin{aligned} P1 &= 19.47 + [3.14] \cdot [3.79]^{-1} \cdot [O1 - 19.09] \\ P2 &= 19.09 + [3.14] \cdot [3.56]^{-1} \cdot [O2 - 19.47] \end{aligned} \quad (\text{B.9})$$

B.1.2 Second scenario

Estimated	Symbol	Available	Symbol
Me angle	P	Go-Sagittal (right)	O1
		Go-Sagittal (left)	O2

$$P = 62.30 + [13.53 \quad 9.05] \cdot \begin{bmatrix} 11.11 & 8.09 \\ 8.09 & 9.65 \end{bmatrix}^{-1} \cdot \begin{bmatrix} O1 - 46.99 \\ O2 - 44.93 \end{bmatrix} \quad (\text{B.10})$$

Estimated	Symbol	Available	Symbol
Id-Me angle	P	Convexity angle	O

$$P = 69.04 + [-21.24] \cdot [23.91]^{-1} \cdot [O - 8.19] \quad (\text{B.11})$$

Estimated	Symbol	Available	Symbol
Me-Go-Co (right)	P	Sn-GoGn (right)	O1
		Sn-GoGn (left)	O2

$$P = 115.34 + [11.15 \quad 10.26] \cdot \begin{bmatrix} 24.38 & 21.99 \\ 21.99 & 22.52 \end{bmatrix}^{-1} \cdot \begin{bmatrix} O1 - 32.21 \\ O2 - 31.12 \end{bmatrix} \quad (\text{B.12})$$

Estimated	Symbol	Available	Symbol
Me-Go-Co (left)	P	Sn-GoGn (right)	O1
		Sn-GoGn (left)	O2

$$P = 115.93 + [7.18 \quad 8.24] \cdot \begin{bmatrix} 24.38 & 21.99 \\ 21.99 & 22.52 \end{bmatrix}^{-1} \cdot \begin{bmatrix} O1 - 32.21 \\ O2 - 31.12 \end{bmatrix} \quad (\text{B.13})$$

Estimated	Symbol	Available	Symbol
Id-Me	P	Sn-GoGn (right)	O1
		Sn-GoGn (left)	O2

$$P = 34.07 + [7.67 \quad 7.99] \cdot \begin{bmatrix} 24.38 & 21.99 \\ 21.99 & 22.52 \end{bmatrix}^{-1} \cdot \begin{bmatrix} O1 - 32.21 \\ O2 - 31.12 \end{bmatrix} \quad (\text{B.14})$$

Estimated	Symbol	Available	Symbol
Me-Go (right)	P	FO-FO ZA-ZA	O1 O2

$$P = 89.40 + [6.40 \quad 6.11] \cdot \begin{bmatrix} 13.49 & 9.83 \\ 9.83 & 16.07 \end{bmatrix}^{-1} \cdot \begin{bmatrix} O1 - 101.59 \\ O2 - 95.24 \end{bmatrix} \quad (\text{B.15})$$

Estimated	Symbol	Available	Symbol
Me-Go (left)	P	Sn-GoGn (right) Sn-GoGn (left)	O1 O2

$$P = 88.84 + [6.06 \quad 5.76] \cdot \begin{bmatrix} 24.38 & 21.99 \\ 21.99 & 22.52 \end{bmatrix}^{-1} \cdot \begin{bmatrix} O1 - 32.21 \\ O2 - 31.12 \end{bmatrix} \quad (\text{B.16})$$

B.2 Female Algorithms

B.2.1 First scenario

Estimated	Symbol	Available	Symbol
Me angle	P1	Go-Sagittal (right)	O1
Me angle	P2	Go-Sagittal (left)	O2

$$\begin{aligned} P1 &= 62.44 + [12.28] \cdot [11.92]^{-1} \cdot [O - 44.62] \\ P2 &= 62.44 + [7.62] \cdot [12.34]^{-1} \cdot [O - 43.22] \end{aligned} \quad (\text{B.17})$$

Estimated	Symbol	Available	Symbol
Me-Go-Co (right)	P1	Me-Go-Co (left)	O1
Me-Go-Co (left)	P2	Me-Go-Co (right)	O2

$$\begin{aligned}
P1 &= 115.45 + [19.84] \cdot [27.20]^{-1} \cdot [O1 - 115.40] \\
P2 &= 115.40 + [19.84] \cdot [21.17]^{-1} \cdot [O2 - 115.45]
\end{aligned}
\tag{B.18}$$

Estimated	Symbol	Available	Symbol
Go-Sagittal (right)	P1	Go-Sagittal (left)	O1
Go-Sagittal (left)	P2	Go-Sagittal (right)	O2

$$\begin{aligned}
P1 &= 44.62 + [7.12] \cdot [9.48]^{-1} \cdot [O1 - 43.22] \\
P2 &= 43.22 + [7.12] \cdot [7.26]^{-1} \cdot [O2 - 44.62]
\end{aligned}
\tag{B.19}$$

Estimated	Symbol	Available	Symbol
Co-Sagittal (right)	P1	Co-Sagittal (left)	O1
Co-Sagittal (left)	P2	Co-Sagittal (right)	O2

$$\begin{aligned}
P1 &= 47.11 + [7.11] \cdot [8.94]^{-1} \cdot [O1 - 47.20] \\
P2 &= 47.20 + [7.11] \cdot [9.78]^{-1} \cdot [O2 - 47.11]
\end{aligned}
\tag{B.20}$$

Estimated	Symbol	Available	Symbol
Co-Go (right)	P1	Co-Go(left)	O1
Co-Go (left)	P2	Co-Go(right)	O2

$$\begin{aligned}
P1 &= 54.09 + [18.30] \cdot [19.82]^{-1} \cdot [O1 - 53.01] \\
P2 &= 53.01 + [18.30] \cdot [22.94]^{-1} \cdot [O2 - 54.09]
\end{aligned}
\tag{B.21}$$

Estimated	Symbol	Available	Symbol
Co-Sig (right)	P1	Co-Sig (left)	O1
Co-Sig (left)	P2	Co-Sig (right)	O2

$$\begin{aligned} P1 &= 18.06 + [8.62] \cdot [9.28]^{-1} \cdot [O1 - 17.72] \\ P2 &= 17.72 + [8.62] \cdot [9.23]^{-1} \cdot [O2 - 18.06] \end{aligned} \quad (\text{B.22})$$

Estimated	Symbol	Available	Symbol
Go-Me (right)	P1	Facial angle	O1
		Go-Me (left)	O2
Go-Me (left)	P2	Facial angle	O3
		Go-Me (right)	O4

$$\begin{aligned} P1 &= 84.97 + [5.06 \quad 19.69] \cdot \begin{bmatrix} 4.38 & 4.08 \\ 4.08 & 20.89 \end{bmatrix}^{-1} \cdot \begin{bmatrix} O1 - 86.99 \\ O2 - 85.13 \end{bmatrix} \\ P2 &= 89.06 + [19.69 \quad 4.08] \cdot \begin{bmatrix} 4.38 & 5.06 \\ 5.06 & 21.15 \end{bmatrix}^{-1} \cdot \begin{bmatrix} O3 - 86.99 \\ O4 - 84.97 \end{bmatrix} \end{aligned} \quad (\text{B.23})$$

Estimated	Symbol	Available	Symbol
Co-in - Co-out (right)	P1	Co-in - Co-out (left)	O1
Co-in - Co-out (left)	P2	Co-in - Co-out (right)	O2

$$\begin{aligned} P1 &= 17.78 + [3.47] \cdot [4.63]^{-1} \cdot [O1 - 17.82] \\ P2 &= 17.82 + [3.47] \cdot [4.28]^{-1} \cdot [O2 - 17.78] \end{aligned} \quad (\text{B.24})$$

B.2.2 Second scenario

Estimated	Symbol	Available	Symbol
Me angle	P	Go-Sagittal (right)	O1
		Go-Sagittal (left)	O2

$$P = 62.44 + [10.08 \quad 11.03] \cdot \begin{bmatrix} 7.26 & 7.12 \\ 7.12 & 9.48 \end{bmatrix}^{-1} \cdot \begin{bmatrix} O1 - 44.62 \\ O2 - 43.22 \end{bmatrix} \quad (\text{B.25})$$

Estimated	Symbol	Available	Symbol
Id-Me angle	P	Convexity angle	O

$$P = 69.35 + [-29.42] \cdot [31.67]^{-1} \cdot [O - 8.49] \quad (\text{B.26})$$

Estimated	Symbol	Available	Symbol
Me-Go-Co (right)	P	Sn-GoGn (right)	O1

$$P = 115.45 + [11.15] \cdot [35.99]^{-1} \cdot [O1 - 34.52] \quad (\text{B.27})$$

Estimated	Symbol	Available	Symbol
Me-Go-Co (left)	P	Sn-GoGn (right)	O1
		Sn-GoGn (left)	O2

$$P = 115.40 + [20.01 \quad 19.54] \cdot \begin{bmatrix} 35.99 & 34.28 \\ 34.28 & 35.00 \end{bmatrix}^{-1} \cdot \begin{bmatrix} O1 - 34.52 \\ O2 - 33.41 \end{bmatrix} \quad (\text{B.28})$$

Estimated	Symbol	Available	Symbol
Id-Me	P	Sn-GoGn (right)	O1
		Sn-GoGn (left)	O2

$$P = 31.78 + [9.96 \quad 10.16] \cdot \begin{bmatrix} 35.99 & 34.28 \\ 34.28 & 35.00 \end{bmatrix}^{-1} \cdot \begin{bmatrix} O1 - 34.52 \\ O2 - 33.41 \end{bmatrix} \quad (\text{B.29})$$

Estimated	Symbol	Available	Symbol
Me-Go (right)	P	FO-FO	O1
		ZA-ZA	O2

$$P = 84.97 + [8.01 \quad 8.77] \cdot \begin{bmatrix} 12.91 & 9.14 \\ 9.14 & 20.00 \end{bmatrix}^{-1} \cdot \begin{bmatrix} O1 - 97.14 \\ O2 - 90.24 \end{bmatrix} \quad (\text{B.30})$$

Estimated	Symbol	Available	Symbol
Me-Go (left)	P	FO-FO	O1
		ZA-ZA	O2

$$P = 85.13 + [9.20 \quad 9.39] \cdot \begin{bmatrix} 12.91 & 9.14 \\ 9.14 & 20.00 \end{bmatrix}^{-1} \cdot \begin{bmatrix} O1 - 97.14 \\ O2 - 90.24 \end{bmatrix} \quad (\text{B.31})$$

Appendix C

Individual Subject Results

The reconstruction of 10 mandibular instances was tested using a SPM and SSM. These mandibles were separate to the dataset used for the creation of the models.

C.1 First scenario

Figure C.1 displays the landmarks that are manually located and fed into the SSM as partial input.

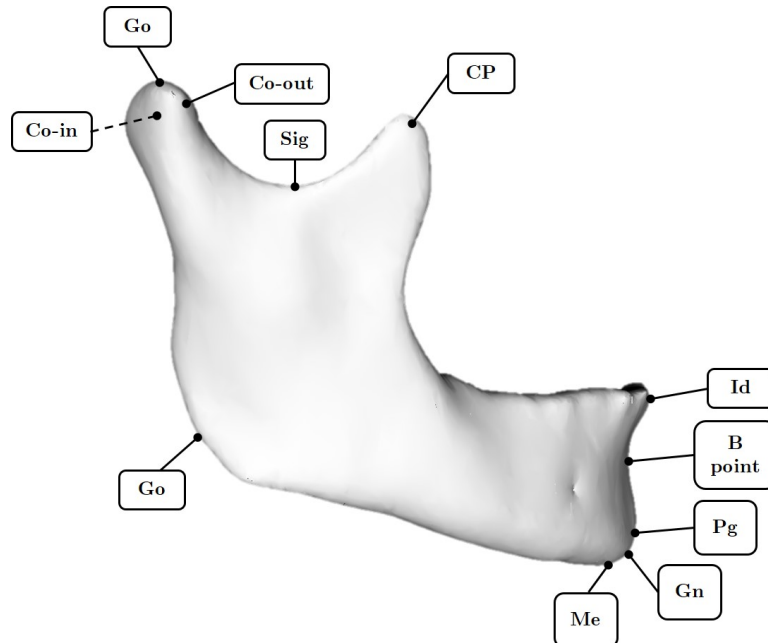


Figure C.1: Manual landmark selection for first scenario
(Illustration: RL Gillingham)

C.1.1 Male subjects

Anonymized code: 2BDE2F29		Mirroring		SSM		SPM		
Age (years) 26		Right	Left	Right	Left	Right	Left	
Measurements	Surface-to-surface	[mm]	0.97	0.96	1.04	1.29	-	-
	Me angle	[°]	1.44	1.17	0.51	0.04	4.95	2.86
	Me-Go-Co	[°]	1.18	0.93	1.10	2.14	3.01	4.72
	Go-Sagittal	[mm]	1.37	1.84	1.44	0.51	2.43	1.47
	Co-Sagittal	[mm]	1.75	1.69	0.72	1.84	1.58	2.41
	Co-Go	[mm]	1.78	2.22	2.45	0.07	3.71	3.95
	Co-Sig	[mm]	1.14	0.62	2.41	2.97	0.45	0.81
	Go-Me	[mm]	0.26	1.42	1.29	1.32	2.22	0.61
	Co-in - Co-out	[mm]	1.49	1.42	0.52	1.11	0.05	0.10

Anonymized code: 2CE7D393		Mirroring		SSM		SPM		
Age (years) 25		Right	Left	Right	Left	Right	Left	
Measurements	Surface-to-surface	[mm]	1.11	1.14	1.28	1.10	-	-
	Me angle	[°]	0.39	1.46	1.07	1.64	1.08	3.71
	Me-Go-Co	[°]	1.145	2.71	4.29	1.28	2.60	0.70
	Go-Sagittal	[mm]	2.13	2.15	2.10	1.84	0.97	0.80
	Co-Sagittal	[mm]	1.03	0.15	0.17	0.64	0.23	1.25
	Co-Go	[mm]	2.27	3.46	1.78	0.51	0.70	1.40
	Co-Sig	[mm]	0.41	0.69	0.29	1.17	1.92	1.69
	Go-Me	[mm]	2.25	0.72	1.57	0.63	1.75	2.43
	Co-in - Co-out	[mm]	0.26	0.76	0.50	1.82	0.04	0.53

Anonymized code: 5DA79D3A		Mirroring		SSM		SPM		
Age (years) 38		Right	Left	Right	Left	Right	Left	
Measurements	Surface-to-surface	[mm]	1.08	1.33	1.01	1.13	-	-
	Me angle	[°]	1.35	0.58	0.69	0.57	4.18	3.34
	Me-Go-Co	[°]	0.20	0.33	1.22	3.78	1.45	0.14
	Go-Sagittal	[mm]	0.55	0.12	1.73	2.12	1.66	0.20
	Co-Sagittal	[mm]	2.20	2.66	0.16	0.03	0.60	0.25
	Co-Go	[mm]	1.80	0.19	0.94	0.55	1.21	0.08
	Co-Sig	[mm]	1.05	0.76	2.07	0.32	0.56	0.62
	Go-Me	[mm]	3.20	1.16	1.41	1.97	2.89	2.73
	Co-in - Co-out	[mm]	0.76	0.29	1.28	0.45	2.36	2.37

Anonymized code: 08C9110C		Mirroring		SSM		SPM		
Age (years) 25		Right	Left	Right	Left	Right	Left	
Measurements	Surface-to-surface	[mm]	1.22	1.07	0.80	0.91	-	-
	Me angle	[°]	2.33	1.99	0.03	0.91	1.91	3.08
	Me-Go-Co	[°]	1.48	1.17	1.48	1.34	2.43	2.34
	Go-Sagittal	[mm]	1.81	2.45	0.76	0.73	3.07	2.71
	Co-Sagittal	[mm]	1.71	0.89	1.10	0.28	4.96	4.08
	Co-Go	[mm]	1.54	0.78	0.06	2.16	1.67	3.60
	Co-Sig	[mm]	1.62	2.00	1.79	3.63	0.82	0.44
	Go-Me	[mm]	1.16	0.90	0.27	0.56	0.40	3.03
	Co-in - Co-out	[mm]	2.00	1.97	1.30	2.24	0.59	0.64

Anonymized code: 0FC7C8CB		Mirroring		SSM		SPM		
Age (years) 27		Right	Left	Right	Left	Right	Left	
Measurements	Surface-to-surface	[mm]	0.9	0.84	1.22	1.20	-	-
	Me angle	[°]	1.47	2.17	1.40	1.38	0.78	1.52
	Me-Go-Co	[°]	0.13	1.33	2.24	3.06	0.90	0.16
	Go-Sagittal	[mm]	1.41	2.07	2.28	3.57	1.51	4.65
	Co-Sagittal	[mm]	1.64	0.66	1.31	0.47	1.14	1.58
	Co-Go	[mm]	0.98	0.78	1.63	3.76	3.41	2.71
	Co-Sig	[mm]	0.71	0.08	0.76	1.93	0.25	0.63
	Go-Me	[mm]	0.27	0.28	0.46	2.38	1.80	1.44
	Co-in - Co-out	[mm]	1.13	1.00	1.97	1.24	0.47	0.44

Anonymized code:		9DF59D9C	Mirroring		SSM		SPM	
Age (years)		19	Right	Left	Right	Left	Right	Left
Measurements	Surface-to-surface	[mm]	1.46	0.9	0.83	1.31	-	-
	Me angle	[°]	0.18	0.57	0.86	0.49	0.45	0.57
	Me-Go-Co	[°]	3.13	3.01	0.93	0.64	3.91	2.23
	Go-Sagittal	[mm]	3.22	2.42	0.08	2.27	0.02	2.52
	Co-Sagittal	[mm]	1.88	0.78	0.30	0.61	0.03	0.01
	Co-Go	[mm]	0.97	2.71	1.08	3.44	1.87	1.21
	Co-Sig	[mm]	1.60	1.64	0.30	2.06	0.16	0.71
	Go-Me	[mm]	5.60	6.25	0.94	3.45	1.06	1.96
	Co-in - Co-out	[mm]	1.83	1.65	1.74	1.43	0.40	0.63

Anonymized code:		9FA1979F	Mirroring		SSM		SPM	
Age (years)		23	Right	Left	Right	Left	Right	Left
Measurements	Surface-to-surface	[mm]	1.02	0.87	1.18	1.17	-	-
	Me angle	[°]	0.74	0.52	0.27	0.23	3.23	3.08
	Me-Go-Co	[°]	4.04	4.13	2.68	1.75	7.31	6.29
	Go-Sagittal	[mm]	0.72	0.64	1.89	1.31	1.04	0.16
	Co-Sagittal	[mm]	1.04	0.90	0.38	1.36	7.40	6.27
	Co-Go	[mm]	2.56	3.23	1.11	4.59	0.90	3.16
	Co-Sig	[mm]	1.16	1.16	0.70	2.06	0.13	0.43
	Go-Me	[mm]	0.65	0.42	3.19	1.15	0.17	2.47
	Co-in - Co-out	[mm]	1.96	1.16	2.42	2.38	1.00	0.64

Anonymized code:		0731DF30	Mirroring		SSM		SPM	
Age (years)		24	Right	Left	Right	Left	Right	Left
Measurements	Surface-to-surface	[mm]	0.7	0.84	0.78	0.95	-	-
	Me angle	[°]	0.67	1.84	0.01	0.86	2.10	1.73
	Me-Go-Co	[°]	3.05	1.14	0.42	1.61	0.66	0.23
	Go-Sagittal	[mm]	3.33	3.85	1.70	2.06	2.65	4.96
	Co-Sagittal	[mm]	2.53	2.22	1.40	0.15	2.21	3.24
	Co-Go	[mm]	1.34	1.05	0.98	3.00	0.36	0.37
	Co-Sig	[mm]	0.97	1.06	1.96	3.17	1.20	0.31
	Go-Me	[mm]	2.60	0.80	1.12	1.37	0.14	0.26
	Co-in - Co-out	[mm]	0.49	0.16	0.67	0.43	1.27	2.13

Anonymized code: EB74FEB9		Mirroring		SSM		SPM		
Age (years)		Right	Left	Right	Left	Right	Left	
Measurements	Surface-to-surface	[mm]	1.18	0.96	0.84	1.14	-	-
	Me angle	[°]	0.26	0.20	1.91	0.09	3.88	4.96
	Me-Go-Co	[°]	2.41	0.30	5.58	1.96	1.49	0.56
	Go-Sagittal	[mm]	1.46	0.66	1.65	0.75	0.58	1.72
	Co-Sagittal	[mm]	0.67	0.70	0.14	0.70	0.28	1.15
	Co-Go	[mm]	0.90	0.93	4.87	1.90	1.36	2.32
	Co-Sig	[mm]	0.45	0.27	1.81	0.64	0.80	0.17
	Go-Me	[mm]	2.35	1.80	1.27	1.72	2.83	2.54
	Co-in - Co-out	[mm]	0.90	0.70	0.88	2.00	1.15	0.79

Anonymized code: 9A956112		Mirroring		SSM		SPM		
Age (years)		Right	Left	Right	Left	Right	Left	
Measurements	Surface-to-surface	[mm]	1.55	1.16	1.64	1.33	-	-
	Me angle	[°]	1.86	1.56	0.57	1.61	6.44	8.83
	Me-Go-Co	[°]	1.31	1.46	3.24	1.32	0.52	0.06
	Go-Sagittal	[mm]	3.57	1.77	1.56	1.30	0.90	3.05
	Co-Sagittal	[mm]	0.16	1.03	1.68	0.55	2.27	4.11
	Co-Go	[mm]	0.88	0.18	4.57	2.32	0.27	1.91
	Co-Sig	[mm]	0.60	0.01	3.54	0.38	0.26	0.55
	Go-Me	[mm]	0.40	0.74	0.06	0.75	0.63	1.96
	Co-in - Co-out	[mm]	0.55	0.42	1.75	1.57	0.01	0.19

C.1.2 Female subjects

Anonymized code:		4B4EC893	Mirroring		SSM		SPM	
Age (years)		30	Right	Left	Right	Left	Right	Left
Measurements	Surface-to-surface	[mm]	1.36	1.65	1.10	1.64	-	-
	Me angle	[°]	0.08	2.09	0.65	1.05	1.09	1.64
	Me-Go-Co	[°]	2.37	0.13	1.49	5.55	0.42	1.76
	Go-Sagittal	[mm]	1.63	1.06	1.12	0.54	1.30	0.80
	Co-Sagittal	[mm]	1.06	2.10	0.90	1.52	0.07	0.55
	Co-Go	[mm]	0.71	1.86	0.81	3.51	1.86	2.53
	Co-Sig	[mm]	0.15	0.37	0.10	0.46	0.34	0.05
	Go-Me	[mm]	0.45	2.34	0.98	3.00	1.32	0.43
	Co-in - Co-out	[mm]	0.57	0.93	1.97	3.15	1.24	1.75

Anonymized code:		6C9FACE3	Mirroring		SSM		SPM	
Age (years)		24	Right	Left	Right	Left	Right	Left
Measurements	Surface-to-surface	[mm]	0.94	0.90	1.12	1.36	-	-
	Me angle	[°]	1.24	0.31	0.42	0.31	1.48	2.27
	Me-Go-Co	[°]	0.21	0.28	0.23	3.81	1.41	2.02
	Go-Sagittal	[mm]	0.01	1.66	0.20	1.77	1.87	1.26
	Co-Sagittal	[mm]	0.24	4.92	0.52	5.34	0.42	1.14
	Co-Go	[mm]	0.37	0.26	0.37	3.41	2.15	1.71
	Co-Sig	[mm]	1.00	0.93	0.81	0.22	0.76	0.82
	Go-Me	[mm]	0.90	0.40	0.57	2.66	2.76	0.66
	Co-in - Co-out	[mm]	1.58	1.28	4.23	1.16	0.77	3.99

Anonymized code:		365B85A0	Mirroring		SSM		SPM	
Age (years)		34	Right	Left	Right	Left	Right	Left
Measurements	Surface-to-surface	[mm]	1.32	1.43	1.26	1.42	-	-
	Me angle	[°]	1.96	1.99	2.96	1.14	4.91	2.13
	Me-Go-Co	[°]	4.52	5.11	5.60	3.84	1.41	1.78
	Go-Sagittal	[mm]	0.93	0.65	3.27	0.35	1.87	2.27
	Co-Sagittal	[mm]	0.11	1.03	0.26	1.67	0.42	1.32
	Co-Go	[mm]	1.50	0.12	2.54	1.00	2.15	2.00
	Co-Sig	[mm]	1.08	1.36	0.56	0.41	0.76	0.40
	Go-Me	[mm]	0.01	1.30	1.53	1.98	2.76	2.99
	Co-in - Co-out	[mm]	0.24	0.53	0.47	1.53	0.77	1.22

Anonymized code:		A42038AA	Mirroring		SSM		SPM	
Age (years)		43	Right	Left	Right	Left	Right	Left
Measurements	Surface-to-surface	[mm]	0.79	0.85	0.85	1.03	-	-
	Me angle	[°]	2.01	0.33	0.75	0.04	1.58	0.80
	Me-Go-Co	[°]	1.75	0.89	0.17	5.78	1.86	3.06
	Go-Sagittal	[mm]	0.88	1.17	0.88	0.42	1.22	2.45
	Co-Sagittal	[mm]	0.59	1.23	0.32	0.11	4.24	4.10
	Co-Go	[mm]	0.21	0.03	1.00	1.28	1.20	0.12
	Co-Sig	[mm]	0.46	0.25	1.08	0.52	1.71	1.93
	Go-Me	[mm]	0.01	1.19	0.48	1.84	1.13	0.56
	Co-in - Co-out	[mm]	0.46	0.18	2.32	0.69	2.15	2.42

Anonymized code:		B91AE436	Mirroring		SSM		SPM	
Age (years)		30	Right	Left	Right	Left	Right	Left
Measurements	Surface-to-surface	[mm]	0.96	1.05	1.36	1.51	-	-
	Me angle	[°]	1.78	1.55	0.36	1.30	3.83	5.28
	Me-Go-Co	[°]	0.16	0.66	3.16	4.00	4.66	5.84
	Go-Sagittal	[mm]	0.80	0.07	0.05	1.11	1.37	0.66
	Co-Sagittal	[mm]	0.11	1.33	0.20	2.14	0.18	1.37
	Co-Go	[mm]	2.45	2.52	2.25	3.59	1.93	0.92
	Co-Sig	[mm]	0.97	0.89	0.88	2.37	1.49	0.94
	Go-Me	[mm]	2.47	4.09	1.36	1.07	2.81	2.00
	Co-in - Co-out	[mm]	0.24	0.62	2.15	0.28	1.33	0.42

Anonymized code:		EBD9926E	Mirroring		SSM		SPM	
Age (years)		25	Right	Left	Right	Left	Right	Left
Measurements	Surface-to-surface	[mm]	1.54	1.54	1.68	1.36	-	-
	Me angle	[°]	1.89	4.73	2.71	2.12	0.80	1.93
	Me-Go-Co	[°]	3.02	5.67	6.69	4.23	7.55	10.5
	Go-Sagittal	[mm]	0.47	0.22	3.45	0.69	0.55	1.21
	Co-Sagittal	[mm]	2.03	2.56	0.23	2.99	3.60	3.56
	Co-Go	[mm]	6.63	1.48	3.62	5.53	1.45	2.64
	Co-Sig	[mm]	2.04	2.80	0.44	0.40	0.74	0.98
	Go-Me	[mm]	1.49	3.41	1.47	1.52	0.25	0.36
	Co-in - Co-out	[mm]	0.14	0.21	1.63	0.42	0.04	0.55

Anonymized code:		C472A912	Mirroring		SSM		SPM	
Age (years)		21	Right	Left	Right	Left	Right	Left
Measurements	Surface-to-surface	[mm]	1.59	1.50	1.68	1.36	-	-
	Me angle	[°]	0.18	0.27	2.71	1.42	3.15	4.21
	Me-Go-Co	[°]	2.72	0.16	6.69	4.91	1.86	0.58
	Go-Sagittal	[mm]	1.04	0.98	3.45	1.14	0.76	0.80
	Co-Sagittal	[mm]	1.06	0.08	0.23	0.71	0.91	1.01
	Co-Go	[mm]	3.41	0.89	3.62	0.70	0.19	0.68
	Co-Sig	[mm]	0.48	2.09	0.44	2.25	0.95	1.94
	Go-Me	[mm]	2.21	0.91	1.47	1.57	1.43	1.51
	Co-in - Co-out	[mm]	0.77	4.32	1.63	3.38	0.09	0.77

Anonymized code:		5C425429	Mirroring		SSM		SPM	
Age (years)		23	Right	Left	Right	Left	Right	Left
Measurements	Surface-to-surface	[mm]	1.37	1.6	0.87	0.92	-	-
	Me angle	[°]	1.90	2.98	0.35	0.27	5.60	3.90
	Me-Go-Co	[°]	2.98	3.15	1.62	3.17	1.65	1.76
	Go-Sagittal	[mm]	3.67	3.45	0.06	0.04	1.08	1.47
	Co-Sagittal	[mm]	3.14	3.23	3.22	0.37	1.62	2.79
	Co-Go	[mm]	1.02	1.69	3.20	2.38	2.13	2.42
	Co-Sig	[mm]	0.22	0.30	2.12	3.59	0.71	1.24
	Go-Me	[mm]	2.36	0.04	0.24	0.37	2.17	2.80
	Co-in - Co-out	[mm]	1.20	1.22	2.65	2.52	0.50	0.55

Anonymized code:		B5B13B80	Mirroring		SSM		SPM	
Age (years)		22	Right	Left	Right	Left	Right	Left
Measurements	Surface-to-surface	[mm]	1.13	1.10	1.54	1.26	-	-
	Me angle	[°]	0.28	1.29	0.06	0.33	1.72	3.39
	Me-Go-Co	[°]	0.78	0.67	0.48	1.64	2.18	2.39
	Go-Sagittal	[mm]	0.02	0.57	0.80	0.20	0.98	1.55
	Co-Sagittal	[mm]	0.24	0.05	0.58	0.33	1.36	1.11
	Co-Go	[mm]	1.65	4.42	0.66	1.64	2.58	3.72
	Co-Sig	[mm]	0.72	0.22	0.82	2.25	1.68	2.15
	Go-Me	[mm]	0.23	2.82	0.60	0.20	1.86	1.44
	Co-in - Co-out	[mm]	0.01	0.03	1.04	2.43	0.91	1.69

C.2 Second scenario

Figure C.2 displays the landmarks that are manually located and fed into the SSM as partial input.

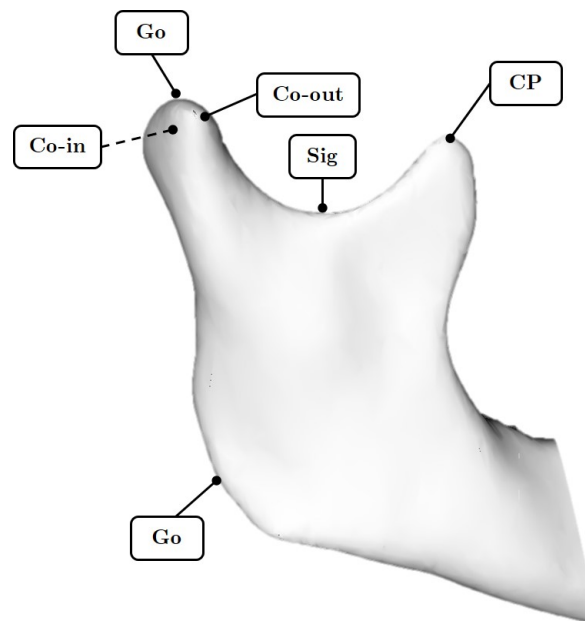


Figure C.2: Manual landmark selection for first scenario
(Illustration: RL Gillingham)

C.2.1 Male subjects

Anonymized code:		2BDE2F29	
Age (years)		26	SSM SPM
Surface-to-surface		[mm]	1.20 -
Measurements	Me angle	[°]	0.18 4.95
	Id-Me angle	[°]	1.63 2.80
	Me-Go-Co (right)	[°]	0.34 1.04
	Me-Go-Co (left)	[°]	0.19 4.80
	Id-Me	[mm]	1.20 1.98
	Go-Me (right)	[mm]	0.34 5.69
	Go-Me (left)	[mm]	0.41 4.83

Anonymized code:		2CE7D393	
Age (years)		25	SSM SPM
Surface-to-surface		[mm]	1.21 -
Measurements	Me angle	[°]	0.04 1.08
	Id-Me angle	[°]	6.70 12.7
	Me-Go-Co (right)	[°]	1.47 1.57
	Me-Go-Co (left)	[°]	0.99 1.98
	Id-Me	[mm]	3.92 1.94
	Go-Me (right)	[mm]	0.55 1.78
	Go-Me (left)	[mm]	0.24 0.63

Anonymized code:		5DA79D3A	
Age (years)		38	SSM SPM
Surface-to-surface		[mm]	1.34 -
Measurements	Me angle	[°]	0.97 4.18
	Id-Me angle	[°]	4.57 0.55
	Me-Go-Co (right)	[°]	1.10 1.94
	Me-Go-Co (left)	[°]	0.62 1.14
	Id-Me	[mm]	0.74 0.31
	Go-Me (right)	[mm]	0.43 2.95
	Go-Me (left)	[mm]	1.67 0.01

Anonymized code:		08C9110C	
Age (years)		25	SSM SPM
Surface-to-surface		[mm]	0.73 -
Measurements	Me angle	[°]	0.39 1.91
	Id-Me angle	[°]	1.30 2.59
	Me-Go-Co (right)	[°]	0.87 0.31
	Me-Go-Co (left)	[°]	1.83 1.04
	Id-Me	[mm]	0.59 2.45
	Go-Me (right)	[mm]	1.44 1.02
	Go-Me (left)	[mm]	1.32 3.66
	Anonymized code:		0FC7C8CB
Age (years)		27	SSM SPM
Surface-to-surface		[mm]	1.35 -
Measurements	Me angle	[°]	0.32 0.78
	Id-Me angle	[°]	2.31 1.65
	Me-Go-Co (right)	[°]	2.59 4.65
	Me-Go-Co (left)	[°]	1.42 3.15
	Id-Me	[mm]	2.45 0.05
	Go-Me (right)	[mm]	0.17 4.01
	Go-Me (left)	[mm]	0.31 2.50
	Anonymized code:		9Df59D9C
Age (years)		19	SSM SPM
Surface-to-surface		[mm]	1.79 -
Measurements	Me angle	[°]	1.03 0.45
	Id-Me angle	[°]	0.78 6.71
	Me-Go-Co (right)	[°]	1.27 3.21
	Me-Go-Co (left)	[°]	1.68 0.58
	Id-Me	[mm]	0.47 1.51
	Go-Me (right)	[mm]	0.72 2.02
	Go-Me (left)	[mm]	1.05 4.05

		Anonymized code: 9FA1979F			
		Age (years)	23	SSM	SPM
		Surface-to-surface	[mm]	1.58	-
Measurements	Me angle	[°]	0.60	3.23	
	Id-Me angle	[°]	0.53	2.71	
	Me-Go-Co (right)	[°]	1.77	6.17	
	Me-Go-Co (left)	[°]	0.33	2.16	
	Id-Me	[mm]	1.24	0.44	
	Go-Me (right)	[mm]	1.49	2.31	
	Go-Me (left)	[mm]	0.31	4.50	
			Anonymized code: 0731DF30		
		Age (years)	24	SSM	SPM
		Surface-to-surface	[mm]	0.80	-
Measurements	Me angle	[°]	0.21	2.10	
	Id-Me angle	[°]	0.46	0.86	
	Me-Go-Co (right)	[°]	0.15	3.59	
	Me-Go-Co (left)	[°]	0.48	3.08	
	Id-Me	[mm]	0.75	0.22	
	Go-Me (right)	[mm]	0.58	1.00	
	Go-Me (left)	[mm]	0.03	0.87	
			Anonymized code: EB74FEB9		
		Age (years)	19	SSM	SPM
		Surface-to-surface	[mm]	1.14	-
Measurements	Me angle	[°]	0.16	3.88	
	Id-Me angle	[°]	2.64	8.56	
	Me-Go-Co (right)	[°]	0.98	6.62	
	Me-Go-Co (left)	[°]	0.37	6.09	
	Id-Me	[mm]	0.23	0.92	
	Go-Me (right)	[mm]	0.10	3.24	
	Go-Me (left)	[mm]	0.05	0.48	

Anonymized code:		9A956112	
Age (years)		25	SSM SPM
Surface-to-surface		[mm]	1.30 -
Measurements	Me angle	[°]	0.56 6.44
	Id-Me angle	[°]	0.30 0.70
	Me-Go-Co (right)	[°]	0.73 0.74
	Me-Go-Co (left)	[°]	0.54 1.23
	Id-Me	[mm]	0.93 0.74
	Go-Me (right)	[mm]	1.39 6.97
	Go-Me (left)	[mm]	1.52 8.74

C.2.2 Female subjects

Anonymized code:		4B4EC893	
Age (years)		30	SSM SPM
Surface-to-surface		[mm]	1.15 -
Measurements	Me angle	[°]	0.76 2.10
	Id-Me angle	[°]	2.74 4.51
	Me-Go-Co (right)	[°]	0.62 0.04
	Me-Go-Co (left)	[°]	1.50 2.30
	Id-Me	[mm]	1.97 0.92
	Go-Me (right)	[mm]	0.34 6.27
	Go-Me (left)	[mm]	0.23 5.76

Anonymized code:		6C9FACE3	
Age (years)		24	SSM SPM
Surface-to-surface		[mm]	1.43 -
Measurements	Me angle	[°]	0.87 1.53
	Id-Me angle	[°]	2.37 0.68
	Me-Go-Co (right)	[°]	1.65 3.75
	Me-Go-Co (left)	[°]	0.74 7.47
	Id-Me	[mm]	0.36 2.04
	Go-Me (right)	[mm]	3.95 0.03
	Go-Me (left)	[mm]	2.00 0.69

Anonymized code:		365B85A0	
Age (years)		34	SSM SPM
Measurements	Surface-to-surface	[mm]	1.39 -
	Me angle	[°]	1.49 3.45
	Id-Me angle	[°]	2.91 9.20
	Me-Go-Co (right)	[°]	3.14 2.29
	Me-Go-Co (left)	[°]	2.45 1.38
	Id-Me	[mm]	0.31 0.92
	Go-Me (right)	[mm]	0.96 1.23
	Go-Me (left)	[mm]	1.30 1.78

Anonymized code:		A42038AA	
Age (years)		43	SSM SPM
Measurements	Surface-to-surface	[mm]	0.95 -
	Me angle	[°]	0.22 0.63
	Id-Me angle	[°]	2.99 1.91
	Me-Go-Co (right)	[°]	0.12 5.61
	Me-Go-Co (left)	[°]	0.55 1.57
	Id-Me	[mm]	0.52 0.81
	Go-Me (right)	[mm]	0.46 4.33
	Go-Me (left)	[mm]	0.70 3.71

Anonymized code:		B91AE436	
Age (years)		30	SSM SPM
Measurements	Surface-to-surface	[mm]	0.84 -
	Me angle	[°]	0.17 4.90
	Id-Me angle	[°]	3.80 8.63
	Me-Go-Co (right)	[°]	0.05 4.04
	Me-Go-Co (left)	[°]	0.77 6.93
	Id-Me	[mm]	0.22 5.12
	Go-Me (right)	[mm]	0.73 7.24
	Go-Me (left)	[mm]	0.48 5.15

Anonymized code:		EBD9926E		
Age (years)	25	SSM	SPM	
Surface-to-surface	[mm]	1.31	-	
Measurements	Me angle	[°]	0.13	1.23
	Id-Me angle	[°]	2.43	0.57
	Me-Go-Co (right)	[°]	0.84	3.73
	Me-Go-Co (left)	[°]	3.03	7.68
	Id-Me	[mm]	0.67	2.50
	Go-Me (right)	[mm]	1.90	0.39
	Go-Me (left)	[mm]	0.13	0.74

Anonymized code:		C472A912		
Age (years)	21	SSM	SPM	
Surface-to-surface	[mm]	1.79	-	
Measurements	Me angle	[°]	0.19	3.74
	Id-Me angle	[°]	7.26	3.95
	Me-Go-Co (right)	[°]	1.15	0.04
	Me-Go-Co (left)	[°]	1.97	1.43
	Id-Me	[mm]	1.84	0.86
	Go-Me (right)	[mm]	0.70	0.87
	Go-Me (left)	[mm]	0.80	0.65

Anonymized code:		5C425429		
Age (years)	23	SSM	SPM	
Surface-to-surface	[mm]	1.56	-	
Measurements	Me angle	[°]	1.92	4.75
	Id-Me angle	[°]	3.41	2.41
	Me-Go-Co (right)	[°]	1.52	0.55
	Me-Go-Co (left)	[°]	3.43	1.74
	Id-Me	[mm]	2.09	1.75
	Go-Me (right)	[mm]	2.24	1.55
	Go-Me (left)	[mm]	2.37	4.33

Anonymized code:		B513B80	
Age (years)		22	SSM SPM
Surface-to-surface		[mm]	1.21 -
Measurements	Me angle	[°]	1.68 2.49
	Id-Me angle	[°]	0.95 5.91
	Me-Go-Co (right)	[°]	0.78 1.77
	Me-Go-Co (left)	[°]	0.81 2.19
	Id-Me	[mm]	2.50 0.17
	Go-Me (right)	[mm]	1.84 4.12
	Go-Me (left)	[mm]	3.45 2.63